UNIVERSIDADE ESTADUAL PAULISTA
"JÚLIO DE MESQUITA FILHO"
Campus de Ilha Solteira

Breno Ebinuma Takiuti

A STUDY INTO WAVE SCATTERING FROM DISCONTINUITIES IN ONE-DIMENSIONAL WAVEGUIDES USING FINITE ELEMENT ANALYSIS

Ilha Solteira
2018

UNIVERSIDADE ESTADUAL PAULISTA
"JÚLIO DE MESQUITA FILHO"
Campus de Ilha Solteira

Breno Ebinuma Takiuti

A STUDY INTO WAVE SCATTERING FROM DISCONTINUITIES IN ONE-DIMENSIONAL WAVEGUIDES USING FINITE ELEMENT ANALYSIS

Dissertação apresentada à Faculdade de Engenharia - UNESP – Campus de Ilha Solteira, para obtenção do título de Doutor em Engenharia Mecânica.
Área de Conhecimento: Mecânica dos Sólidos

Prof. Dr. Vicente Lopes Júnior
Orientador
Profª. Drª. Elisabetta Manconi
Co-Orientador

Ilha Solteira
2018

FICHA CATALOGRÁFICA
Desenvolvido pelo Serviço Técnico de Biblioteca e Documentação

Takiuti, Breno Ebinuma.
T136a A Study into wave scattering from discontinuities in one-dimensional waveguides using finite element analysis / Breno Ebinuma Takiuti. -- Ilha Solteira: [s.n.], 2018
155 f. : il.

Tese (doutorado) - Universidade Estadual Paulista. Faculdade de Engenharia. Área de conhecimento: Mecânica dos Sólidos, 2018

Orientador: Vicente Lopes Júnior
Co-orientador: Elisabetta Manconi
Inclui bibliografia

1. Ondas guiadas. 2. Reflexão de ondas. 3. Elementos finitos. 4. Detecção de danos.

Sandra Maria Clemente de Souza
DSTBD/STRAUD
Supervisão de Seção
CRB 8-4740

unesp

UNIVERSIDADE ESTADUAL PAULISTA

Câmpus de Ilha Solteira

CERTIFICADO DE APROVAÇÃO

TÍTULO DA TESE: A study into wave scattering from discontinuities in one-dimensional waveguides using finite element analysis

AUTOR: BRENO EBINUMA TAKIUTI
ORIENTADOR: VICENTE LOPES JUNIOR

Aprovado como parte das exigências para obtenção do Título de Doutor em ENGENHARIA MECÂNICA, área: Mecanica dos Sólidos pela Comissão Examinadora:

Prof. Dr. VICENTE LOPES JUNIOR
Departamento de Engenharia Mecânica / Faculdade de Engenharia de Ilha Solteira

Prof. Dr. MICHAEL JOHN BRENNAN
Departamento de Engenharia Mecânica / Faculdade de Engenharia de Ilha Solteira

Prof. Dr. DOUGLAS DOMINGUES BUENO
Departamento de Matemática / Faculdade de Engenharia de Ilha Solteira - UNESP

PROFESSOR TITULAR PAULO SÉRGIO VAROTO
Departamento de Engenharia Mecânica / ESCOLA DE ENGENHARIA DE SÃO CARLOS-USP

Prof. Dr. MARCOS SILVEIRA
Departamento de Engenharia Mecânica / Faculdade de Engenharia de Bauru

Ilha Solteira, 04 de dezembro de 2018

ACKNOWLEDGEMENTS

I would like to express my thanks to my committee chair and advisor, Professor Vicente Lopes Júnior, to whom I have been working under since my undergraduate dissertation. He encouraged me to face the world, go to international conferences and study abroad.

I would like to express my deepest gratitude toward Professor Elisabetta Manconi, who advised me in the time I spent in Italy, and throughout the entire PhD studies. Even not knowing me, and even with my lack of preparation in the area of wave propagation and simulation, she accepted me as a student, helped me in the time spent in Italy and guided me step by step in our research. She is a brilliant researcher and her love for new discoveries captivated me and always gave me strength even in the darkest moments.

I would like to thank Professor Michael John Brennan, for his support during the time I was still struggling with initial concepts, and during the final periods, by giving insights to the results and discussions. His experience, knowledge and patience are endless and helped me a lot through all the periods of research.

I would like to thank my fiancé Patricia Hashimoto, for her support during all these years of academic research, and for her patience during the time I spent abroad. She is the reason for all the effort I make and will make in my entire life.

I would like to thank my parents Célia Takiuti and Robert Takiuti, for all the support given until now. I hope that one day I can repay all the love and patience they have given me.

Special thanks to Dario Mangoni, Iryna Yasinskaya and the guys from “Gruppo pranzo”, for their support during the initial period in Italy and for the companionship during the time in the University of Parma.

Special thanks to the colleagues in my office and the GMSINT group, for all these years of companionship, and to Professor Antonio Eduardo Turra, for his friendship and wise advice.

The author gratefully acknowledge the financial support provided by the Coordenação de Aperfeiçoamento de Pessoal de Nível Superior – Brasil (CAPES) – Finance Code 001.

Part of the work was carried out while the author held a fellowship at University of Parma, Italy, funded by the Ministero degli Affari Esteri Italiano – Italy. The author gratefully acknowledge the financial support provided.

RESUMO

Prever a dispersão das ondas incidentes em uma seção danificada de uma estrutura é importante para o monitoramento da saúde estrutural e técnicas de testes não destrutivas a fim de se detectar danos. Nesses casos, ondas de alta frequência são geralmente envolvidas e modelos simples, que não conseguem capturar o comportamento dinâmico das guias de onda, podem resultar em falha experimental ou má interpretação dos resultados. Além disso, os danos geralmente não são simétricos em relação ao eixo neutro da estrutura, resultando na conversão do modo de onda e diferentes ondas refletidas e transmitidas se propagando com diferentes velocidades. O objetivo deste trabalho é investigar a reflexão e transmissão de ondas em uma guia de onda unidimensional devido a descontinuidades assimétricas. Estes podem ser tubos contendo fluido, placas, vigas ou estruturas em geral os quais estejam sujeitas a propagação de ondas em uma única direção, com mudanças na área da seção transversal, que podem ser interpretadas como danos estruturais. Essas podem ser alterações de área de seção transversal pontuais ou de tamanho finito e também podem ser simétricas ou assimétricas com relação à linha neutra da guia de onda. Múltiplos tipos de modos de ondas são considerados e conversão de onda devido às interações com descontinuidades são investigadas para altas frequências (frequências a cima da frequência de corte do segundo modo de Lamb simétrico, S2). Neste trabalho, a análise de propagação de onda em guias de ondas danificadas é realizada usando o método de Elementos Finitos de Onda (do inglês *Wave Finite Element method*). Neste método, um pequeno segmento do guia de ondas é modelado usando um dado número de elementos finitos sólidos ou planos, discretizado ao longo da seção transversal, e que descreve tanto um rico comportamento de onda como os fenômenos de conversão de modos de onda em altas frequências. Condições de continuidade e equilíbrio de forças são impostas nas interfaces da descontinuidade, usando a metodologia baseada na matriz de onda, e a matriz de reflexão é obtida junto com as razões de potência de reflexão e transmissão. Estes valores fornecem informações valiosas sobre o efeito de danos na reflexão e transmissão de ondas. Esta metodologia é validada através da comparação com resultados analíticos para casos mais simples. Os resultados são apresentados através dos coeficientes de reflexão e transmissão, coeficientes de potência, energia cinética e velocidade da energia. Exemplos numéricos são estudados de modo a simular diversas condições de danos.

Palavras-chave: Ondas guiadas. Reflexão de ondas. Elementos finitos. Detecção de danos.

ABSTRACT

Predicting the scattering from waves that are incident on a damaged section of a structure is of importance in structural health monitoring and non-destructive testing techniques to detect damage. High-frequency waves are generally involved, and simple models, which cannot capture the dynamic behaviour of the waveguides at high frequency, can result in experimental failure and misinterpretation of the results. Moreover, the damage can be non-symmetrical with respect to the neutral axis of the structure, resulting in wavemode conversion and different reflected and transmitted waves propagating with different velocities. The aim of this work is to investigate wave reflection and transmission due to symmetric and non-symmetric discontinuities in one-dimensional waveguides. These can be fluid-filled pipes, plates, beams, or more generally structures involving wave propagation in one direction, with a change of cross-section, which can be seen as a structural damage. In particular, wave scattering from changes of cross-sectional area in a beam/plate are numerically studied. These can be point or finite length changes of area and they can be symmetric or non-symmetric with respect to the axis of the waveguide. Multiple wave modes are considered and conversion due to interaction with the discontinuity are investigated up to high frequency (above the cut-off of the second symmetric Lamb wave mode, S_2).The Wave Finite Element method is applied to the structure for studying the wave propagation in the damaged waveguides. Using this technique, a small segment of the waveguide is modelled by a number of solid or plane finite elements, meshed through the cross-section, which can describe both rich wave behaviour and wavemode conversion up to high frequency. Continuity and equilibrium conditions are then imposed at the interfaces of the discontinuity using a wave-matrix based approach, and the scattering matrix is obtained together with the power reflection and transmission ratios. These provide valuable information about the effect of damage on the reflected and transmitted propagating waves. The approach is validated through comparison with analytical results for simple cases. Results are presented in terms of reflection and transmission displacement and power coefficients, kinetic energy, and energy velocity. Numerical examples are studied to show different damage conditions and results are discussed

Keywords: Guided waves. Wave scattering. Finite elements. Damage detection.

LIST OF FIGURES

LIST OF TABLES

LIST OF SYMBOLS

Symbol	Name	Units
b	Width of a beam or bar	[mm]
E	Young's modulus	[N/m^2]
f	Force	[N]
F_s	Spring Force	[N]
h	Height of a beam or bar	[mm]
I	Second moment of area	[m^4]
k	Wave number	[m^{-1}]
L	Length of the waveguide or element	[m]
M	Bending moment	[N.m]
M_s	Spring Bending moment	[N.m]
P	Energy flow	[W]
q	External loading	[N]
R	Reflection Coefficient	[-]
S	Cross-sectional area	[m^2]
s_1	Spring stiffness	[N/m]
T	Transmission Coefficient	[-]
u	Longitudinal displacement	[m]
U	Longitudinal Amplitude	[m]
V	Shear force	[N]
w	Bending displacement	[m]
W	Bending Amplitude	[m]
Z	Characteristic Impedance	[kg/s]
α	Dimensionless stiffness ratio	[-]
β	Dimensionless area ratio	[-]
Γ	Kinetic energy	[J]
Δ	Potential energy	[J]
ρ	Density	[kg/m3]
ϕ	Phase	[deg]
θ	Angular displacement	[rad]
λ	Eigenvalues	

σ	Correction factor	[-]
υ	Poisson's ratio	[-]
ω	Angular frequency	[rad/s]
Π	Time-averaged energy flow	[W]

C	Damping matrix
D	Dynamic stiffness matrix
f	Vector containing the forces
I	Identity matrix
K	Stiffness matrix
M	Mass matrix
q	Vector containing the displacements or amplitudes
S	Scattering matrix
T	Spatial transformation matrix
Φ	Matrix of wave modes
Ψ	Matrix of the left eigenvalues

Subscripts and superscripts

H	Hermitian operator
P	Propagating mode
N	Nearfield mode
L	Left
R	Right

CONTENTS

1 INTRODUCTION

1.1 SCOPE OF THE THESIS

The aim of this work is to contribute to the numerical modelling of wave scattering in one-dimensional waveguides for Structural Health Monitoring (SHM) applications involving high-frequency wave propagation. Damage detection is one of the primary goals in SHM. However, at high frequency, standard methods can fail in describing the rich and complex wave behaviour, resulting in poor efficiency of the diagnostic set-up or misinterpretation of the experimental results. This work deals with the application of a Wave Finite Element (WFE) method to predict the wave scattering behaviour of damaged waveguides. These can be beam or plate with symmetric or asymmetric variations of the cross-sectional area (notch), which can be representative of open cracks, or damage due to corrosion in one-dimensional waveguides.

Structural Health Monitoring techniques have been extensively developed in the last decade to check the structural integrity of engineering structures and consequently maintain their functionality safely and without presenting severe risks of failures. When dealing with the maintenance of mechanical systems and structures, three approaches can be typically taken: 1) the corrective maintenance, where the system/structure must fail before getting repaired (or replaced); 2) preventive maintenance, where the critical parts are replaced periodically; 3) predictive, where sensors are used to provide real-time measurements of the condition of the system/structure. SHM can be viewed as an improvement of the third case. The primary goal of the SHM is, in fact, to detect damage in order to avoid catastrophic failures (unexpected breakage of a system) using sensor networks, which provide information that is then post-processed to predict the remaining useful life of the system or part (damage prognosis). Thanks to this information, the engineer will be able to take the necessary actions reducing greatly the costs for repairs and replacements, but also drastically reducing the risk of catastrophic failures. One of the field in which, for obvious reasons, this method is most widely applied, is the aerospace industry (BOLLER; STASZEWSKI, 2004). However, several other fields can be benefited from its use such as for example, inspection of the structural integrity of pipeline systems.

In pipelines for oil, gas, and water distribution, the economic and environmental risks of leakages or failures are of primary importance. Concerning the civil water distribution pipeline system, for example, most of the pipes are old with a high presence of leakages, which implies water loss and loss of water pressure, higher energy consumption and sometimes

erosion of the surrounding soil. According to SNIS[1] (*Sistema Nacional de Informações sobre Saneamento* – in English, National Information System about Sanitation - Brazil), the rate of water losses in the Brazilian water distribution system varies from 32%, in the central-western region, to 49% in the northern region, which represents 32% and 51% respectively in monetary losses. São Paulo, which is the most populous state, registered 34% of water loss, and 30% of monetary loss. In a country with an increasing number of cities with water shortage, summed with the increase in the energy consumption generated by the leakages, the development of pipe defect detection and location is a crucial topic. Also, leakages in oil and gas pipes can cause irreparable damage to the environment, and therefore they must be avoided as much as possible. Because of this, researchers are focusing on new methods for monitoring the structural integrity of pipes.

As described by Alleyne, Lowe and Cawley (1998), typically damage in a pipe appears on the outer surface of the pipe, due to corrosion or scratches. These kinds of discontinuity can be seen as a non-symmetric cross-sectional area change, which is difficult to model analytically because of the mode conversion resultant from the non-symmetry. In a similar way as in Demma *et al.* (2004), this work proposes a study of a WFE method for modelling symmetric and non-symmetric discontinuities (damage) in terms of a change of the cross-sectional area, which can be used to predict the wave scattering from damage. The study deals with the application of a WFE method to predict the behaviour of damaged waveguides in order to develop a model, which can be later used for SHM techniques based on Lamb waves in pipes and tubes modelled as one dimensional waveguides. Using this approach, a small segment of a one-dimensional waveguide is discretized using standard Finite Element (FE) analysis. The FE mass and stiffness matrices are then post-processed using the theory of wave propagation in periodic structures to get dispersion curves and wavemodes. These are used to formulate the scattering wave problem and obtain information on the reflection and transmission of the waves. The numerical approach is validated by comparison of the results with those obtained from analytical models for axial and flexural wave propagation, viz. rod and Euler-Bernoulli beam. This is then applied to more complex cases, such as a thick beam with a notch, which better emulate a real damaged waveguide due to corrosion. Results are given up to high frequency, where the analytical models are expected to fail.

[1] **Planilha AE2012: resumo por abrangência**, 2014

1.2 LITERATURE REVIEW

1.2.1 Damage detection techniques

Some widely used damage detection methods are the electromechanical impedance method and the Lamb wave method. In both cases, piezoelectric sensors and actuators are used. In short, the electromechanical impedance method consists on using PZT patches to excite the structure with some kind of signal (usually some frequency sweep as for example, the CHIRP function) and the same PZTs are used as a sensor to measure the impedance of the combination of structure and sensor. The obtained measurements are compared with the measurements of the healthy structure (baseline) and a damage index is calculated to identify the presence of damage. This method is based on the fact that the stiffness and the mass of the structure are changed with the appearance of a damage, causing a change in the impedance, e.g. Lopes *et al.* (2000).

Most of the SHM techniques deal with the study of wave scattering and wave propagation in the damaged structure. Studies on wave propagation date back in ancient time, and a lot of important works and studies has been written. The first studies related to waves was perhaps performed by Pythagoras in the 6th century BC, (GRAFF, 1975). Following him, several great names contributed directly or indirectly to the wave formulation, such as Galileo Galilei, Robert Hooke, Isaac Newton, Brook Taylor, Leonard Euler and many others. Regarding wave propagation in elastic solids, one of the most important names is Lord Rayleigh, with his work “On Waves Propagated along the Plane Surface of an Elastic Solid”, where he first described the behaviour of a wave propagating in the free surface of an infinite homogeneous isotropic elastic solid. Then came the researches by Horace Lamb where he first described the behaviour of a wave propagating in plates, originating the term “guided waves”. A few decades later, the theory developed by them and refined by several others, motivated the appearance of damage detection techniques based on wave propagation and more recently the numeric modelling methods began to rise (GRAFF, 1975).

One simple example of damage detection using waves is proposed by Tua, Quek and Wang (2005), in which the Time of Flight (TOF) is used as a parameter to find out the location of the damage. The TOF is the time taken for the wave to travel through the mean, reflect at some kind of discontinuity and get back to the excitation location. Gao *et al.* (2004) performed initial studies about using the noise measurements originated from the water transport system in plastic pipes. Using the cross-correlation between two signals measured at different positions, they were able to find a delay between them, which could be used to calculate the position of the damage. Following this work, Almeida *et al.* (2014) performed a comparative

study using three different types of sensors (accelerometer, hydrophone and geophone) simultaneously, in order to determine the advantages and disadvantages of each case. Satyarnarayan *et al.* (2008) evaluated the possibility to use guided waves emitted in the circumferential direction of the tube, aiming to detect defects at both inner and outer side of the pipe. Köppe, Bartholmai and Prager (2012) proposed to develop a guided wave emission device using a set of piezoelectric actuators distributed around the pipe. Ying *et al.* (2013) studied three different pattern recognition techniques (adaptive boosting, modified adaptive boosting and support vector machines) to recognize damage patterns in measured signals.

1.2.2 Modelling of wave propagation using numerical methods

The wave propagation analysis can be performed by using analytical and numerical methods. The wave behaviour is typically described in terms of the propagation (dispersion curves and wavemodes), attenuation, damping, reflection and transmission of waves. In simple cases, such as rods, thin beams and thin plates, analytical solutions can be found (GRAFF, 1975). However, for more complicated structures and at high frequency, when the wavelength become comparable with the cross-sectional dimensions, the 3D theory of elasticity must be applied and the analytical formulation become more and more complicated, involving systems of differential equations which are difficult or impossible to solve.

Perhaps, the most common and widely used numerical method to accomplish structural problems posed over complicated geometric and material domain is the Finite Element Method (FEM). In the FEM a structure is discretized into small pieces, called elements, characterized by the behaviour of discrete points called nodes. By using these, the behaviour of each element is represented by simple functions, typically polynomial, called shape functions, making possible to find the static or dynamic solutions of structures posed over complicated domains. FE analysis has been also applied to evaluate the wave behaviour. One example of the conventional FEM applied to damage modelling in pipes is the works by Zheng *et al.* (2011), where a 3D FE model of a circular cylindrical structure was used to study the propagation of ultrasonic guided wave modes and their interaction with defects.

The problem with using FEM to model the dynamics at high frequency is that FE errors become significant if the size of the elements, used to discretize the structure, is too large to represent the higher vibrational modes. Considering waves instead of vibrational modes, the same consideration holds. As a rule-of-thumb, there should be at least 6 or more elements to represent the shortest wavelength. In most cases, this can lead to FE models which are impractically large. On the other hand, if the elements are too small round-off errors can occur

in the evaluation of the dynamic stiffness matrix when $\omega^2|\mathbf{M}| \ll |\mathbf{K}|$, e.g. Waki, Mace and Brennan (2009b). Moreover, higher frequency dynamics, which involves nondestructive testing and also noise transmission, shock response, etc. typically require wave modelling while standard FE approaches are not suited for wave analysis. Therefore, different approaches must be used.

It should be noted that the terms low, mid or high related to the frequency are relative to the size of the waveguide with respect to the shortest wavelength that can propagate in the structure. In particular, when the thickness of the structure becomes comparable to the wavelength, pure axial, torsional and flexural modes start changing behaviour due to the through-thickness displacements under the passage of the waves and higher order wavemodes, with more complicated behaviour, start propagating. As an example, considering the typical dispersion curves for a thin plate, frequencies well below the first cut-off frequency can be considered "low" while frequencies above the third or fourth cut-off frequencies can be considered "high". More details about cut-off frequencies and dispersion curves can be found in Chapter 5. Some methods propose to overcome these issues exploiting FE discretization in the normal direction to the waveguide direction and imposing harmonic displacement in the space domain in the propagation direction, such as the Spectral Finite Elements Method (SFEM). According to Lee (2009), SFEM can be defined as the combinations of the spatial discretization and assembly by FEM, wave mode superposition via Fast Fourier Transform (FFT) from the Spectral Analysis Method (SAM) and exactness and reduced number of Degrees-of-Freedom (DOF) from the Dynamic Stiffness Method (DSM). In this method, a single waveguide with no discontinuities (no change of properties) can be modelled by using a single FE element, from which the dynamic stiffness is calculated and the eigensolutions or the frequency response solutions can be obtained for the whole waveguide (LEE, 2009). This method differs from the FE method as it does not require finer discretization for higher frequencies, only requiring to add a new element when the properties of the waveguide change. Some examples of works involving the use of the SFEM are: Mahapatra and Gopalakrishnan (2003) where the SFEM was applied to uniform composite tubes; Sreekanth Kumar, Roy Mahapatra and Gopalakrishnan (2004) where SFEM was used to diagnose transverse cracks in beams by dividing the structure into 6 parts and the crack was simulated by a transverse gap between two elements; Żak and Krawczuk (2010), which compared several formulation for the rod spectral element and proposed a high-order multi-mode theory, and was shown to give better results for calculating the dispersion curves; later a work by the same authors (ŻAK;

KRAWCZUK, 2011) investigated the numerical problems related to node distribution in the elements in modelling wave propagation in a rod. According to this, the Lobatto and Chebyshev node distributions are recommended instead of linear node distribution. These distributions are used to reduce or eliminate the Runge phenomenon, which causes the element shape functions to exhibit undesired oscillations near the element ends. Roughly these distributions can be described as having fewer points in the middle of the element and progressively more points close to the element's end. Brigham *et al.* (2011) studied the application of SFEM in soft solids (such as organic tissues for medical applications), where the low stiffness combined with high-frequency harmonic loads gives rise to numerical errors called "pollution" and proposed the use of higher-order spectral elements to minimize pollution errors. Another example can be found in Nanda, Kapuria and Gopalakrishnan (2014) where the authors proposed a formulation of spectral element using the zigzag theory for wave propagation in composites and sandwich structures and compared the results of dispersion, free vibration and wave propagation with the results obtained using the First-order Shear Deformation Theory (FSDT) and Classical Lamination Theory (CLT). In a more recent work, Murthy, Renji and Gopalakrishnan (2015) also studied the spectral element formulation for sandwich composite waveguides, but in this case, the Extended Higher order Sandwich Panel Theory (EHSaPT) using numerical Laplace transforms was used to formulate the spectral elements. Works by Mitra and Gopalakrishnan (2006) and later by Samaratunga, Jha and Gopalakrishnan (2014) proposed the use of the Wavelet Spectral Finite Element Method (WSFEM), which uses the Daubechies formulation for the wavelet transform to reduce the Partial Differential Equations (PDEs) into Ordinary Differential Equations (ODEs) without the "wrap around" problems encountered when using the Fast Fourier Transform (FFT) based spectral elements methods. Comparison with the conventional SFEM was performed for rods, beams and in waveguides with a transverse crack. In all cases, it was shown that the results with WSFEM are better for short finite waveguides in short time windows.

The drawback of the SFEM is that each structure or waveguide requires an *ad hoc* element formulation, which can be difficult to be realized for some kinds of structure. On the other hand, conventional FEM formulation always uses the same elements, resulting in a reduced complexity for the formulation of the elements, for example exploiting the well-developed element libraries of FE elements in commercial software.

Another option for numerical simulation of wave propagation is the Boundary Elements Method (BEM). According to Cho and Rose (1996), BEM is "more mathematically sophisticated and easier to work numerically than FEM", since only the boundary is discretized

while FEM requires both the domain and the boundary to be discretized. As an example, in the works by Cho and Rose, a hybrid BEM formulation is proposed where the elastodynamic boundary integral equation is linked with the normal mode expansion of the Lamb waves. The same method was successfully applied in Cho, Hongerholt and Rose (1997) for crack evaluation using Lamb waves, and the results were compared with experimental data. Using the same hybrid BEM technique, Zhao and Rose (2003) studied the accuracy in the detection of different configurations of damage using different wave modes. It was found that the ideal frequency range is below the first cut-off frequency, to avoid false positives (damage being detected when there is none) and that in this frequency range it is possible to evaluate the size of the damage using the reflected waves amplitude. Another hybrid BEM technique is proposed by Galán and Abascal (2004), where the waveguide was discretized with BE in the vicinity of the damage while the rest of the waveguide was modelled using FEM. Here a mode conversion factor was used to evaluate the depth of the damage.

One difficulty when using wave propagation for damage detection lies in the fact that the structures are often coated in order to avoid corrosion of the external surfaces. These insulating coatings are usually made of materials with high damping coefficients, which cause the waves to attenuate rapidly resulting in a shorter range of monitoring. From a numerical point of view, the solution of the dispersion relation for coated waveguides is also difficult, since the roots are complex (KIRBY; ZLATEV; MUDGE, 2012). To solve this, Kirby proposed the use of a hybrid Semi-Analytic Finite Element (SAFE) method, which solves the dispersion relation without root searching. In this work, the FEM was used only at the region of the damage, with full discretization, and the rest of the waveguide was modelled by modal expansions; the two solutions were then connected by mode matching. Following this paper, the same method was applied in uncoated pipes, Duan and Kirby (2015), and coated pipes Duan, Kirby and Mudge (2016). Another work, by Barshinger and Rose (2004) proposed to use the global matrix method to study coated pipes, where the waveguide was divided into layers and each layer was studied locally using wave matrix formulation. These matrices were joined in a single global matrix using boundary conditions at the interfaces of the layers. In this case, a theoretical method was shown to be effective in modelling the wave propagation in multi-layered waveguides and the results were validated using experimental data. This paper also indicated that lower frequency modes are more suitable for damage monitoring, see also the work by Zhao and Rose (2003). Works by Hayashi, Song and Rose (2003) and Hayashi, Tamayama and Murase (2006) showed the applicability of the SAFE method in obtaining the dispersion relation in waveguides with an arbitrary cross-section.

1.2.3 Wave Finite Element method (WFE)

WFE method is a relatively new method (ABDEL-RAHMAN, 1979), which was more recently developed for wave characterization in 1D waveguides by Mace *et al.* (2005) and later in 2D waveguides by Mace and Manconi (2008) and Manconi and Mace (2009). The method combines standard FE formulation and the theory of wave propagation in periodic structures (BRILLOUIN, 1953). In short, the mass and stiffness matrices, typically obtained using commercial FE packages, are post-processed using the periodicity conditions in order to obtain an eigenvalue problem whose solutions provide the frequency evolution of the wavenumber (dispersion curves) and the wavemodes. In the paper by Mace *et al.* (2005), the method was presented for 1D waveguides and applied to beams and simply supported plates in order to compare results with analytical solutions, and to more complicated structures as viscoelastic laminated plates. The method was applied to a segment of a tyre, in order to evaluate the free and forced vibrations of this structure (WAKI; MACE; BRENNAN, 2009a). Mace and Manconi (2008) extended the WFE method to 2D structures. In this work shell and solid elements were used to characterize wave propagation waveguides which confines wave propagation in a plane. Later in Manconi and Mace (2009), the same procedure was applied to isotropic, orthotropic and laminated sandwich cylinders and curved panels. In Waki, Mace and Brennan (2009b) the numerical issues associated to the application of the WFE, such as poor conditioning problems, discretization errors caused by the periodicity condition imposed, and truncation errors when using elements which are too small, were investigated. Numerical issues were also investigated by Søe-Knudsen and Sorokin (2011) where the accuracy of the WFE predictions of wavenumbers and power flow was discussed. In particular, a formula using the length of the element and the shortest wavelength was proposed to determine a window in which the WFE wavenumbers are accurate. Manconi and Mace (2010) presented a method for estimating the global loss factor of viscoelastic laminated panels; here a formulation for evaluating the average loss factor in the general case of an anisotropic component was proposed and numerical examples were presented. Later in Manconi, Mace and Garziera (2013) the method was extended to include pre-stress effects, and this method was applied to laminated curves panels and cylinders. More recent work include Zhou *et al.* (2015), which proposed the use of a combination of the Component Mode Synthesis (CMS) with the WFE method in order to further reduce computational costs, and Mencik and Duhamel (2016), which proposed the use of the WFE to model periodic structures with local perturbations of the material and geometric characteristics.

The WFE model can be used to simulate wave scattering using a wave matrix approach: the undamaged sections of the waveguide are modelled using WFE to obtain dispersion relation and wavemodes, the nodal forces and nodal displacement are described using these wavemodes, and equilibrium and force balance is imposed in order to get the scattering matrix. This information can then be used as an indication of damage and later used as a benchmark for detecting damage in real-world applications.

Wave matrix approach for scattering problems was introduced by Mace (1984) who investigated reflection and transmission coefficients in a beam with elastic discontinuities. In his paper, it was observed that even when a nearfield wave is used as the incident wave, it results in a propagating, nearfield reflected and transmitted waves. Later, using this wave matrix formulation, Mace studied the power flow at discontinuities (MACE, 1992a; MACE, 1992b). In Harland, Mace and Jones (2001) wave reflection and transmission in a tunable fluid filled beam were studied in order to use the tunable properties of magneto-rheological or electro-rheological fluids for vibration control. Lee, Mace and Brennan (2007) later studied the reflection and transmission of waves in a non-uniform one-dimensional waveguide. From a damage detection analysis perspective, Ichchou, Mencik and Zhou (2009) presented a study of coupled structures with damage using WFEM to model the undamaged sections and a Diffusion Matrix Model (DMM) to model the damaged coupling section. Results from WFE were compared with those obtained using the SAFE and DMM and they were validated with experimental data. Zhou, Ichchou and Mencik (2009) proposed also the use of the WFE technique to model cylindrical pipes with local inhomogeneity. In this work wave modes and scattered fields were compared with published experimental results. Later, Zhou and Ichchou (2010) studied wave propagation in curved pipes using the WFE, but in this case, the study was focused on characterizing the influence of the curve and the damage on the scattering field in order to establish an ideal incident wave for damage monitoring. It was found that careful preliminary modelling must be performed before applying the experimental monitoring of the structure in order to determine the ideal frequency range for the incident wave that would be less affected by the curvature while maintaining enough sensitivity to the damage.

More recent works by Renno and Mace (2013) and Mitrou, Ferguson and Renno (2017) proposed the study of the reflection and transmission coefficients of joints using a hybrid WFE/FE method. In these works, the joint section was modelled using FE and the rest of the waveguides were modelled using WFE. These sections were joined following the compatibility of the DOFs at the interfaces and equilibrium of internal forces. The results obtained agreed

with experimental results and full FE results. The WFE method was also applied in Masri, Ferguson and Waters (2017) for detecting rebar damage in reinforced beams.

1.2.4 Experimental works on damage detection using wave propagation

Perhaps one of the earlier works on the use of the wave analysis for damage in pipes is the work by Alleyne and Cawley (1996), where the use of the circumferential Lamb wave is proposed. Lamb waves can travel longer distances compared to bulk waves, since the guided waves travel "guided" in the tube's axial direction constituting basically a one-dimensional propagation, as opposed to the bulk waves that travel in all three directions. Later, Alleyne, Lowe and Cawley (1998) studied the damage detection in pipes using guided waves by using analytical, FEM and experimental approaches and introduced some discussions on the range of applicability of this monitoring technique, effect of the dispersion, mode selection, experimental procedures, sensor positioning. Comparison of the analytical, FEM and experimental results for the scattering coefficients were also shown in this work. In Demma *et al.* (2004) the authors proposed a methodology for interpreting guided wave scattering in a pipe with a notch (damage). Muggleton *et al.* (2007) proposed the use of an averaging method to estimate the power reflection and transmission coefficients for discontinuities using measured data only, testing cases with one or more types of waves and different types of waveguides, and using as few measurements as possible. Ihn and Chang (2008) investigated the use of a pitch-catch damage detection method using Lamb waves in aircraft structures, where the healthy structure was excited using Lamb waves and the measured time domain data was compared with the data obtained in an unknown health state. Differences in these measurements are used to evaluate the presence of the damage. More recent works by Kai *et al.* (2009) and Atashipour *et al.* (2013) presented results and studies for thick beams. The difficulty when dealing with thick beams (small length-to-thickness ratio) is that the distance between the upper and lower surfaces of the beams are relatively farther than in thin beams. This makes it difficult to properly excite the structure with a guided wave such as the Lamb wave. Both works presented a detailed experimental procedure and comparison of the experimental results with the FEM model.

1.3 AIMS OF THE THESIS

The aims of the thesis are summarized as follow:

- study a numerical model using the WFE method to investigate wave scattering in one-dimensional waveguides;

- determine wave scattering in simple beam-type waveguides. This first step is fundamental for validating the WFE numerical model by comparison of the result with those obtained from analytical solutions, for understanding issues related to the application of the method and adjust the numerical algorithm, and for developing the numerical procedure for the application of the method to the more complicated cases and when multiple wavemodes are involved;
- determine and understand the types of waves propagating in the structure and their characteristics up to high frequency using the WFE;
- evaluate the wave scattering in one-dimensional waveguides with symmetric and non-symmetric change of area in terms of scattering coefficients and power coefficients;
- evaluate the wave scattering in terms of main displacement characteristics of the reflected and transmitted wave field using the direction component of the scattered kinetic energy;
- investigate the effect of the type of the incident wave and the effects of an increase in the dimensions of the change of area in the waveguide.

1.4 THESIS OUTLINE

The thesis is organised as follows. Chapter 2 deals with an introduction of the WFE method. The equations of motion for several cases are described using the dynamic matrices obtained by standard FE models, the periodicity conditions are applied, and the WFE eigenproblem, whose solutions give the dispersion curves and wave modes, is discussed. Formulation of this eigenvalue problem is shown and a wave matrix approach is introduced to obtain the reflection and transmission (scattering) coefficients. Energy-related quantities are also studied.

In Chapter 3, examples concerning scattering of pure axial and pure flexural waves propagating in a waveguide with point discontinuities are studied using an analytical method. Simple discontinuities are introduced, such as spring type discontinuities and change of cross-sectional area. Several cases are discussed and results are investigated considering also the limiting cases (free, fixed or simply supported cases) and literature results.

In Chapter 4, the same examples studied in Chapter 3 are studied using WFE approach. The results obtained using the WFE approach are validated by comparing the results at low frequency with those obtained by the analytical solutions as in Chapter 3.

In Chapter 5, a one-dimensional waveguide is modelled using more complex FE model. In particular, a stack of plane element meshed through the cross-section was used for predicting the wave propagation up to high frequency. The case of symmetric and non-symmetric changes in cross-sectional areas are introduced and investigated. Scattering coefficients, power coefficients and time-averaged kinetic energies are evaluated. These results are discussed to investigate the changes in the wave behaviour caused by a damage.

2 WAVE PROPAGATION AND SCATTERING USING A WAVE FINITE ELEMENT METHOD

2.1 INTRODUCTION

In this chapter, the procedure to model a waveguide with a discontinuity using the WFE method is studied. The method describes how to obtain the wave scattering due to the discontinuity using wavemodes.

High frequency dynamics are often modelled in terms of waves. In particular, Structural Health Monitoring (SHM) techniques can benefit from the prediction of the wave characteristics and wave reflection and transmission behaviour due to damage. Typically a model for the prediction of the wave propagation characteristics is required in order to understand the structure behaviour under the passage of the waves and therefore to choose an appropriate monitoring method and a damage prognosis system (INMAN *et al.*, 2005). For simple cases an analytical model is sufficient to describe the behaviour of the structure, however, this type of model is typically valid for a limited range of simple structures and for low-frequencies, limiting its application. This is because simple analytical models, such as the rod model or the Euler-Bernoulli beam, are not able to describe high-frequency behaviour since as the frequency goes higher, the wavelength becomes comparable with the waveguide cross-section, and the assumptions (e.g. limited numbers of DOF, displacement in one DOF does not affect the displacements in other DOF and so on) in these models are no longer valid. This is illustrated in Chapter 5, where a beam waveguide is modeled using plane elements and the WFE results are compared to analytical results. As the frequency goes higher, more refined theory, involving less assumption and restrictive hypothesis, must be used in order to model the structural behaviour under the passage of high frequency waves. However, even for simple structures, this results in systems of partial differential equations whose solution is very complicated or even impossible.

A number of numerical methods have been proposed to overcome the limitation of standard analytical approaches in the prediction of high frequency wave propagation. Some methods have proposed a combination of numerical FE modelling and wave propagation. Amongst them we can cite the Dynamic Stiffness Method, e.g. Banerjee (1997), the Spectral Finite Element Method (ROY MAHAPATRA; GOPALAKRISHNAN, 2003), and the Wave Finite Element Method , (MACE *et al.*, 2005; MACE; MANCONI, 2008)

In this work, the Wave Finite Element (WFE) method is used, and this chapter is devoted to the presentation of the method for the evaluation of scattering matrix.

In the following section, the WFE method is introduced following the formulations of the method presented in the literature by Mace *et al.* (2005) and Mace and Manconi (2008). In particular, the procedure to obtain the wavenumbers and wavemodes is described and the nature of the wavemodes are described. To obtain these, an eigenvalue problem must be solved. Formulations of the WFE eigenvalue problem are introduced and some numerical issues are addressed. Once the eigenvalue problem has been solved, the equation of the scattering matrix as a function of the wave modes can be determined (MITROU; FERGUSON; RENNO, 2017; HARLAND, MACE; JONES, 2001). The same formulation is extended for two consecutive discontinuities according to the kind of damage that can be of zero or finite length, which is the case that most closely describes the behaviour of a corroded waveguide.

2.2 WFE METHOD

In this section, the WFE method for wave characterization of one-dimensional waveguides is introduced. In particular, the WFE eigenvalue problem formulation is discussed and two cases are evaluated: the first one is a standard eigenvalue problem formulation, where the wavenumbers of the waveguide are real and given and the frequency is found; the second is a polynomial eigenvalue problem, where a frequency of interest is pre-established and the complex wavenumbers and wavemodes are found (MANCONI, 2008). In this work, the main interest lies in the second problem since the objective is to predict all the waves, including propagating, nearfield and attenuated waves.

Consider a generic one-dimensional waveguide. The FE model of an arbitrary small segment of this waveguide is considered as shown in Figure 1. Discretization is achieved using a standard FE analysis, typically using commercial FE software.

Figure 1 – Small section of a waveguide modelled by FEM.

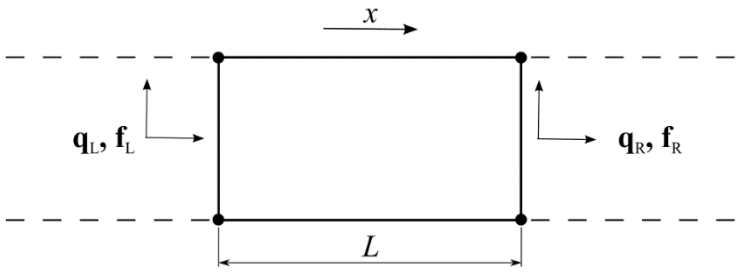

Source: Elaborated by the author

In Figure 1, $\mathbf{q}_L$ and $\mathbf{q}_R$ are the nodal Degrees of Freedom (DOF), viz. displacements and $\mathbf{f}_L$ and $\mathbf{f}_R$ are the nodal forces at each side of the segment of length L. The vectors of the total DOF and nodal forces are organized as

$$\mathbf{q} = \begin{Bmatrix} \mathbf{q}_L \\ \mathbf{q}_R \end{Bmatrix} \text{ and } \mathbf{f} = \begin{Bmatrix} \mathbf{f}_L \\ \mathbf{f}_R \end{Bmatrix} \tag{1}$$

The equation of motion of the FE model of the segment is given by

$$\left[\mathbf{K} + i\omega\mathbf{C} - \omega^2\mathbf{M}\right]\mathbf{q} = \mathbf{f} \tag{2}$$

where **K, C** and **M** are the stiffness, damping and mass matrices, i is the imaginary unit which is given by $i^2 = -1$ and ω is the frequency in radians per seconds.

Using the periodicity condition (BRILLOUIN, 1953), the displacements at the right side can be written in terms of those of the left side using the propagation constant λ

$$\mathbf{q}_R = \lambda\mathbf{q}_L \tag{3}$$

where λ is given by

$$\lambda = e^{-ikL} \tag{4}$$

and k is the wavenumber.

Using the periodic conditions in Eq. (3), the displacement vector can be rewritten as

$$\mathbf{q} = \mathbf{\Lambda}_R\mathbf{q}_L \tag{5}$$

where

$$\mathbf{\Lambda}_R = \begin{bmatrix} \mathbf{I} & \lambda\mathbf{I} \end{bmatrix}^T \tag{6}$$

and **I** is the identity matrix and its dimension is the number of degrees of freedom considered. Assuming no external forces, the sum of the internal nodal forces must be zero, therefore

$$\mathbf{\Lambda}_{\mathrm{L}}\mathbf{f}=\mathbf{0} \tag{7}$$

where

$$\mathbf{\Lambda}_{\mathrm{L}}=\begin{bmatrix}\mathbf{I} & \lambda^{-1}\mathbf{I}\end{bmatrix} \tag{8}$$

Substituting Eqs. (5) and (7) in Eq. (2) and pre-multiplying both sides of the equation by $\mathbf{\Lambda}_{\mathrm{L}}$

$$\mathbf{\Lambda}_{\mathrm{L}}\left[\mathbf{K}+i\omega\mathbf{C}-\omega^{2}\mathbf{M}\right]\mathbf{\Lambda}_{\mathrm{R}}\mathbf{q}_{\mathrm{L}}=\mathbf{0} \tag{9}$$

which can be rewritten as

$$\left[\bar{\mathbf{K}}+i\omega\bar{\mathbf{C}}-\omega^{2}\bar{\mathbf{M}}\right]\mathbf{q}_{\mathrm{L}}=\mathbf{0} \tag{10}$$

where

$$\begin{aligned}\bar{\mathbf{K}}&=\mathbf{\Lambda}_{\mathrm{L}}\mathbf{K}\mathbf{\Lambda}_{\mathrm{R}};\\ \bar{\mathbf{C}}&=\mathbf{\Lambda}_{\mathrm{L}}\mathbf{C}\mathbf{\Lambda}_{\mathrm{R}};\\ \bar{\mathbf{M}}&=\mathbf{\Lambda}_{\mathrm{L}}\mathbf{M}\mathbf{\Lambda}_{\mathrm{R}}\end{aligned} \tag{11}$$

are the reduced stiffness and mass matrices (MACE; MANCONI, 2008). In the following, damping is neglected and the waveguide is assumed to be conservative. By solving the eigenvalue problem in Eq. (9), the dispersion curves and the wavemodes can be found. These give the relationship between the frequency and the wavenumber and the cross-section displacement under the passage of a wave.

The dynamic stiffness matrix of the FE model, that is $\mathbf{D}=\mathbf{K}-\omega^{2}\mathbf{M}$ can be divided into submatrices as

$$\mathbf{D} = \begin{bmatrix} \mathbf{D}_{\mathrm{LL}} & \mathbf{D}_{\mathrm{LR}} \\ \mathbf{D}_{\mathrm{RL}} & \mathbf{D}_{\mathrm{RR}} \end{bmatrix} \tag{12}$$

Equation (9) can be written as

$$\left[\boldsymbol{\Lambda}_{\mathrm{L}} \mathbf{D} \boldsymbol{\Lambda}_{\mathrm{R}}\right] \mathbf{q}_{\mathrm{L}} = \mathbf{0} \tag{13}$$

which gives the WFE eigenvalue problem. This can take different forms as described in the next sections. In the following sections, it is assumed that the frequency is given and real and all the wavenumbers, real, imaginary and complex, must be found.

2.2.1 Polynomial eigenvalue problem

By substituting Eq. (12) in Eq. (13), a polynomial eigenvalue problem is obtained

$$\left[\boldsymbol{\lambda}^2 \mathbf{D}_{\mathrm{LR}} + \boldsymbol{\lambda}\left(\mathbf{D}_{\mathrm{LL}} + \mathbf{D}_{\mathrm{RR}}\right) + \mathbf{D}_{\mathrm{RL}}\right] \mathbf{q}_{\mathrm{L}} = 0 \tag{14}$$

where $\mathbf{q}_{\mathrm{L}}$ is the vector of nodal displacements on the left side of the element. In this case, the solution of this eigenvalue problem yields a vector of eigenvalues $\lambda = e^{-ikL}$ and a matrix of eigenvector $\boldsymbol{\Phi}_{\mathrm{q}}$, which gives the wavenumbers and wavemodes respectively. The latter represents the nodal displacements of the cross-section under the passage of a wave. The matrix of nodal forces $\boldsymbol{\Phi}_{\mathrm{f}}$ can be obtained by $\boldsymbol{\Phi}_{\mathrm{f}} = \mathbf{D}\boldsymbol{\Phi}_{\mathrm{q}}$. The matrices of nodal displacements and forces give the displacements and forces in each degree of freedom of **D** and can be used to draw the wavemode shapes. More on the relationship between wavenumbers and wavemodes can be found in Section 2.2.3.

The dimensions of $\boldsymbol{\lambda}$ and $\boldsymbol{\Phi}$ depends on the number of degrees of freedom in the FE model. As an example, considering axial vibration of a rod, $\boldsymbol{\lambda} = e^{-i\mathbf{k}L}$ is a vector of two elements which gives two wavenumbers: one related to a propagating wave in the positive direction and the other related to propagating wave in the negative direction, so that $\lambda^- = 1/\lambda^+$ where λ^+ relates to the positive propagating wave and λ^- to the negative propagating wave. The eigenvalues, in fact, always occur in pairs $\lambda^- = 1/\lambda^+$ (MACE *et al.*, 2005).

The polynomial eigenvalue problem can be easily solved using Matlab® and using the function *polyeig* or can be recast in a standard eigenvalue problem.

2.2.2 Transfer matrix formulation

Another possible solution is to rewrite the eigenvalue problem into a transfer matrix problem of the form (MACE *et al.*, 2005)

$$\mathbf{T}\begin{Bmatrix}\mathbf{q}_L\\ \mathbf{f}_L\end{Bmatrix} = \lambda\begin{Bmatrix}\mathbf{q}_L\\ \mathbf{f}_L\end{Bmatrix} \tag{15}$$

where **T**, in this case, is a transfer matrix and is given by

$$\mathbf{T} = \begin{bmatrix} -\mathbf{D}_{LR}^{-1}\mathbf{D}_{LL} & \mathbf{D}_{LR}^{-1} \\ -\mathbf{D}_{RL} + \mathbf{D}_{RR}\mathbf{D}_{LR}^{-1}\mathbf{D}_{LL} & -\mathbf{D}_{RR}\mathbf{D}_{LR}^{-1} \end{bmatrix} \tag{16}$$

The eigenvalue problem then becomes a standard eigenvalue problem of the form

$$\mathbf{T}\boldsymbol{\Phi} = \lambda\boldsymbol{\Phi} \tag{17}$$

where $\boldsymbol{\Phi} = [\boldsymbol{\Phi}_q{}^T \quad \boldsymbol{\Phi}_f{}^T]^T$.

Care must be taken when solving the eigenvalue problem using the transfer matrix in Eq. (17). The eigenvalues may have very high and very low values, giving rise to numerical problems. To reduce this problem, Zhong and Williams (1995) proposed an alternative approach rewriting the eigenvalue problem as a generalized eigenvalue problem as

$$\mathbf{A}\boldsymbol{\Phi} = \lambda\mathbf{B}\boldsymbol{\Phi} \tag{18}$$

where

$$\mathbf{A} = \begin{bmatrix} \mathbf{Z} & \mathbf{I} \\ -\mathbf{D}_{RL} & -\mathbf{D}_{RR} \end{bmatrix} \text{ and } \mathbf{B} = \begin{bmatrix} \mathbf{I} & \mathbf{Z} \\ \mathbf{D}_{LL} & \mathbf{D}_{LR} \end{bmatrix} \tag{19}$$

$\boldsymbol{\Phi}$ is again the matrix of eigenvectors, **Z** is a matrix of zeros, and **I** is the identity matrix.

As indicated by Fan *et al.* (2016), the differences in the magnitudes of the submatrices **I** and $\mathbf{D}$ can make the matrices **A** and **B** ill-conditioned. The solution proposed by Fan *et al.*

(2016) is to use a correction factor σ which is normalized according to the $\mathbf{D}_{\mathrm{RR}}$ submatrix. The new matrices **A** and **B** are then written as

$$\mathbf{A}=\begin{bmatrix} \mathbf{Z} & \sigma\mathbf{I} \\ -\mathbf{D}_{\mathrm{RL}} & -\mathbf{D}_{\mathrm{RR}} \end{bmatrix} \text{ and } \mathbf{B}=\begin{bmatrix} \sigma\mathbf{I} & \mathbf{Z} \\ \mathbf{D}_{\mathrm{LL}} & \mathbf{D}_{\mathrm{LR}} \end{bmatrix} \tag{20}$$

where the correction factor is given by

$$\sigma=\frac{\left\|\mathbf{D}_{\mathrm{RR}}\right\|_2}{N^2} \tag{21}$$

where N is the number of columns in $\mathbf{D}_{\mathrm{RR}}$ and $\left\| \right\|_2$ indicates the 2-norm, also known as the Euclidean norm.

2.2.3 Wavenumbers and the corresponding wavemodes

When solving the eigenvalue problem, the vector of wavenumbers **k** and the matrix of wavemodes $\mathbf{\Phi}_{\mathrm{q}}$ and $\mathbf{\Phi}_{\mathrm{f}}$ are sorted according to the numerical routines used to solve the eigenvalue problem, so that the wavemode and wavenumber must be selected according to their nature (propagating, nearfield, attenuated) and direction of propagation. One way to sort them is by verifying if the wavenumber is a real (propagating wave), imaginary (nearfield wave) or complex (attenuated wave) and if its real part is positive or negative. Assuming that $\boldsymbol{\lambda}_i = e^{-i\mathbf{k}_i L}$ and $k_i = a + ib$, the nature of the wave according to the nature of the wavenumbers are shown in Table 1.

Table 1 – Convention for the nature of the wavenumbers.

λ_i	a	b	**Mode**	**Direction**
Real	>0	0	Propagating (P)	Positive (+)
	<0	0		Negative (-)
Imaginary	0	<0	Nearfield (N)	Positive (+)
	0	>0		Negative (-)
Complex	>0	<0	Attenuating (A+)	Positive (+)
	>0	>0	Attenuating (A-)	
	<0	<0	Attenuating (A+)	Negative (-)
	<0	>0	Attenuating (A-)	

Source: Adapted from Hinke, Mace and Brennan (2004).

For conservative waveguides, complex wavenumbers with both real and imaginary parts different from zero, always occur in two pairs of complex conjugate solutions showing positive and negative real parts. These correspond to four different wavemodes, with two A+ wave modes that decay (attenuates) in the positive direction and two A- wave modes that decay in the negative direction. These combine respectively to form standing waves with no transport of energy. To better understand the types of waves, Table 2 shows how each mode looks like.

Table 2 – Representation of the wave modes.

	$a=0$	$a>0$	$a<0$
$b=0$	---	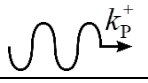	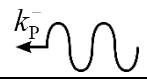
$b>0$	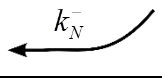	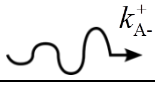	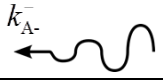
$b<0$	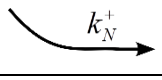	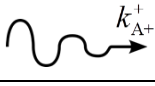	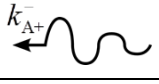

Source: Elaborated by the author

It is important to note that, for conservative structures, the complex modes occurs conjugate pairs and they neither propagate nor carry any energy along the propagation direction.

Considering this, one possible sorting order for the wavenumbers can be

$$\begin{aligned}\mathbf{k}^{+} &= \begin{bmatrix}\mathbf{k}_{\mathrm{P}}^{+} & \mathbf{k}_{\mathrm{N}}^{+} & \mathbf{k}_{\mathrm{A-}}^{+} & \mathbf{k}_{\mathrm{A+}}^{+}\end{bmatrix} \\ \mathbf{k}^{-} &= \begin{bmatrix}\mathbf{k}_{\mathrm{P}}^{-} & \mathbf{k}_{\mathrm{N}}^{-} & \mathbf{k}_{\mathrm{A-}}^{-} & \mathbf{k}_{\mathrm{A+}}^{-}\end{bmatrix}\end{aligned} \tag{22}$$

where the subscripts and superscripts follow the notation in Table 1, in which the superscripts indicate the travel direction and the subscripts indicate the type of wave. The wavemodes follow the same order of $\mathbf{k}$, so if $\mathbf{\Phi}$ is also sorted as in Eq. (22), the type of wavemode and direction can be organized as follows

$$\begin{aligned}\mathbf{\Phi}_{\mathrm{q}}^{+} &= \begin{bmatrix}\mathbf{\Phi}_{\mathrm{q,P}}^{+} & \mathbf{\Phi}_{\mathrm{q,N}}^{+} & \mathbf{\Phi}_{\mathrm{q,A-}}^{+} & \mathbf{\Phi}_{\mathrm{q,A+}}^{+}\end{bmatrix} \\ \mathbf{\Phi}_{\mathrm{q}}^{-} &= \begin{bmatrix}\mathbf{\Phi}_{\mathrm{q,P}}^{-} & \mathbf{\Phi}_{\mathrm{q,N}}^{-} & \mathbf{\Phi}_{\mathrm{q,A-}}^{-} & \mathbf{\Phi}_{\mathrm{q,A+}}^{-}\end{bmatrix}\end{aligned} \tag{23}$$

The eigenvectors corresponding to the nodal forces $\mathbf{\Phi}_{\mathrm{f}}$ can be sorted using the same convention.

As shown in the following sections, the boundary conditions must be imposed and this requires a matrix inversion. Since the matrices that model the boundary conditions are usually sparse matrices (matrices composed mainly by zeroes or numbers with small absolute values) the matrix inversion can be difficult. Also, it is possible that the number of nodes in the two connected waveguides can be different resulting in non-square matrices. In this case, the use of a pseudo-inverse is required to calculate the scattering matrix. One alternative is to use the left eigenvalue $\mathbf{\Psi}$ as shown for example in (WAKI; MACE; BRENNAN, 2009b; RENNO; MACE, 2011). If the right eigenproblem is described as in Eq. (17), the left eigenvectors are obtained as

$$\mathbf{\Psi A} = \mathbf{\lambda}_{\mathrm{T}}\mathbf{\Psi} \tag{24}$$

where the left and right eigenvectors are orthogonal and can be normalized so that

$$\mathbf{\Psi\Phi} = \mathbf{I} \tag{25}$$

Note that $\mathbf{\Psi}$ must be sorted according to the convention used in $\mathbf{k}$ and $\mathbf{\Phi}$.

2.3 WFE MODELLING OF THE SCATTERING MATRIX

Here the wave matrix formulation is studied using a similar formulation as those proposed by Harland, Mace and Jones (2001) and Zhao and Rose (2003). The wave equations

are written in a general matrix form, which can be applied to any kind of waveguide to solve the scattering problem, including more complicated cases.

Now consider two generic waveguides connected by a discontinuity, as shown in Figure 2. In this figure, the box between the two waveguides schematically represents a generic **point** discontinuity, e.g. a spring connecting the two waveguides, a point mass, a change of cross-sectional area, and so on.

Figure 2 – Two generic waveguides separated by a discontinuity.

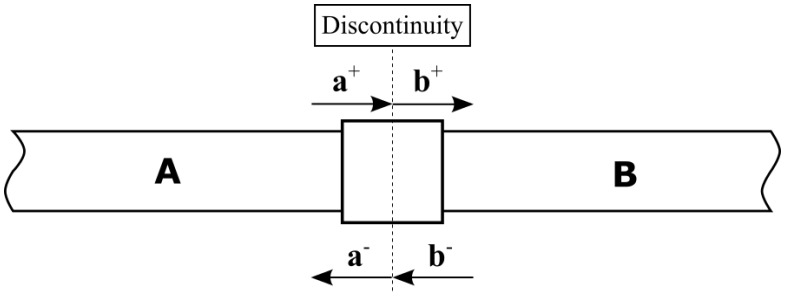

Source: Elaborated by the author

In this case, four wave amplitude vectors are considered, where $\mathbf{a}^+$ and $\mathbf{a}^-$ are the wave's amplitudes in waveguide **A** going to the positive and negative directions respectively and $\mathbf{b}^+$ and $\mathbf{b}^-$ are those in waveguide **B**.

The wave displacements and forces can be written as functions of the wave amplitudes and wavemodes $\mathbf{\Phi}$ as

$$\begin{aligned}
\mathbf{q}_A &= \mathbf{\Phi}^+_{q,A}\mathbf{a}^+ + \mathbf{\Phi}^-_{q,A}\mathbf{a}^- \\
\mathbf{f}_A &= \mathbf{\Phi}^+_{f,A}\mathbf{a}^+ + \mathbf{\Phi}^-_{f,A}\mathbf{a}^- \\
\mathbf{q}_B &= \mathbf{\Phi}^+_{q,B}\mathbf{b}^+ + \mathbf{\Phi}^-_{q,B}\mathbf{b}^- \\
\mathbf{f}_B &= \mathbf{\Phi}^+_{f,B}\mathbf{b}^+ + \mathbf{\Phi}^-_{f,B}\mathbf{b}^-
\end{aligned} \tag{26}$$

where $\mathbf{\Phi}_q$ are the nodal displacements, $\mathbf{\Phi}_f$ the nodal forces, the subscripts A and B refer to the waveguides and + and – indicate the direction of propagation as shown in the previous section and in Figure 2. This procedure to expand displacements and forces using wavemodes in matrix formulation is called here "wave matrix approach". The wavemodes can be either obtained from analytical solutions or by using numerical methods, such as the WFE as in this work.

Continuity of displacements and equilibrium of forces at the discontinuity can be written in a matrix form as

$$\begin{aligned} \mathbf{C}_A\mathbf{q}_A &= \mathbf{C}_B\mathbf{q}_B \\ \mathbf{D}_A\mathbf{f}_A &= \mathbf{D}_B\mathbf{f}_B \end{aligned} \tag{27}$$

where the matrices **C** and **D** are the boundary conditions at the discontinuity.

Substituting Eq. (26)into Eq. (27) results in

$$\begin{Bmatrix} \mathbf{a}^- \\ \mathbf{b}^+ \end{Bmatrix} = \begin{bmatrix} \mathbf{C}_A\boldsymbol{\Phi}^-_{q,A} & -\mathbf{C}_B\boldsymbol{\Phi}^+_{q,B} \\ \mathbf{D}_A\boldsymbol{\Phi}^-_{f,A} & -\mathbf{D}_B\boldsymbol{\Phi}^+_{f,B} \end{bmatrix}^{-1} \begin{bmatrix} -\mathbf{C}_A\boldsymbol{\Phi}^+_{q,A} & \mathbf{C}_B\boldsymbol{\Phi}^-_{q,B} \\ -\mathbf{D}_A\boldsymbol{\Phi}^+_{f,A} & \mathbf{D}_B\boldsymbol{\Phi}^-_{f,B} \end{bmatrix} \begin{Bmatrix} \mathbf{a}^+ \\ \mathbf{b}^- \end{Bmatrix} \tag{28}$$

therefore the scattering matrix $\mathbf{S}$, which is a matrix containing the reflection and transmission coefficients, can be obtained

$$\begin{Bmatrix} \mathbf{a}^- \\ \mathbf{b}^+ \end{Bmatrix} = \mathbf{S} \begin{Bmatrix} \mathbf{a}^+ \\ \mathbf{b}^- \end{Bmatrix} \tag{29}$$

where

$$\mathbf{S} = \begin{bmatrix} \mathbf{C}_A\boldsymbol{\Phi}^-_{q,A} & -\mathbf{C}_B\boldsymbol{\Phi}^+_{q,B} \\ \mathbf{D}_A\boldsymbol{\Phi}^-_{f,A} & -\mathbf{D}_B\boldsymbol{\Phi}^+_{f,B} \end{bmatrix}^{-1} \begin{bmatrix} -\mathbf{C}_A\boldsymbol{\Phi}^+_{q,A} & \mathbf{C}_B\boldsymbol{\Phi}^-_{q,B} \\ -\mathbf{D}_A\boldsymbol{\Phi}^+_{f,A} & \mathbf{D}_B\boldsymbol{\Phi}^-_{f,B} \end{bmatrix} \tag{30}$$

Equation (30) can be rewritten as

$$\mathbf{S} = \begin{bmatrix} \mathbf{S}^{AA} & \mathbf{S}^{AB} \\ \mathbf{S}^{BA} & \mathbf{S}^{BB} \end{bmatrix} \tag{31}$$

Where the **S** matrix is divided into submatrices containing the reflection and transmission matrices for each wavemode. In Eq. (31) the first letter in the superscripts represents the waveguide to where the wave is scattered, and the second indicates from where it is incident. As an example, $\mathbf{S}^{BA}$ is the transmission submatrix for an incident wave coming

from **A** and a transmitted wave travelling in **B.** These can be a single number as in the rod case or *m* by *n* matrices, where *n* is the number of wavemodes considered and *m* is the number of DOFs used to model the waveguide. In Chapter 3 the matrix formulation for the rod and beam are studied and the results are compared with those obtained using an analytical formulation.

In experimental applications, the sensors that measure the wave amplitudes in a waveguide with a discontinuity are not positioned exactly on the discontinuity, therefore there will be a distance from both sensors in **A** and **B** from the discontinuity as depicted in Figure 3.

Figure 3 – Measuring points far from the discontinuity.

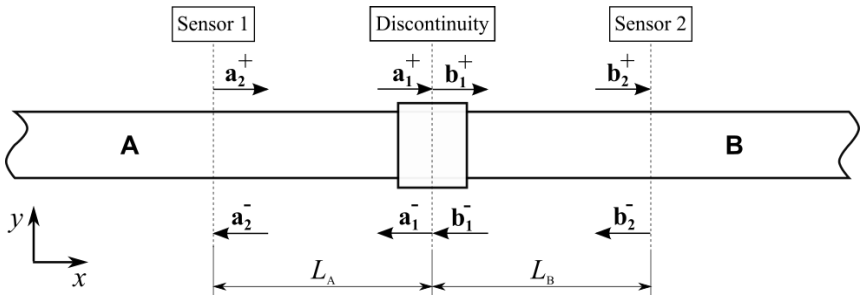

Source: Elaborated by the author

It is assumed that the sensors are applied far enough from the discontinuity, viz. far-field condition. This implies that only propagating waves are impinging upon the damage (no complex and nearfield waves must be considered) and that the sensors do not affect the wave scattering in the region close to the discontinuity. Suppose that the scattered waves are to be measured at a distance L_A and L_B from the discontinuity. If the new amplitudes are called $\mathbf{a}_2$ and $\mathbf{b}_2$, they can be written as

$$\mathbf{a}_2^+ = \mathbf{T}_A \mathbf{a}_1^+, \qquad \mathbf{a}_2^- = \mathbf{T}_A \mathbf{a}_1^- \tag{32}$$

$$\mathbf{b}_2^+ = \mathbf{T}_B \mathbf{b}_1^+, \qquad \mathbf{b}_2^- = \mathbf{T}_B \mathbf{b}_1^- \tag{33}$$

where

$$\mathbf{T}_A = \mathrm{diag}\left(e^{i\mathbf{k}_A L_A}\right), \qquad \mathbf{T}_B = \mathrm{diag}\left(e^{-i\mathbf{k}_B L_B}\right) \tag{34}$$

are the spatial transformation matrices and $\mathbf{k}_A$ and $\mathbf{k}_B$ are the vectors of wavenumbers of waveguides **A** and **B**, see also (BRENNAN; ELLIOTT; PINNINGTON, 1997). Substituting Eqs. (32) and (33) in (29) gives

$$\begin{Bmatrix} \mathbf{a}_2^- \\ \mathbf{b}_2^+ \end{Bmatrix} = \bar{\mathbf{S}} \begin{Bmatrix} \mathbf{a}_2^+ \\ \mathbf{b}_2^+ \end{Bmatrix} \tag{35}$$

where

$$\bar{\mathbf{S}} = \begin{bmatrix} \mathbf{T}_A \mathbf{S}^{AA} \mathbf{T}_A^{-1} & \mathbf{T}_A \mathbf{S}^{AB} \mathbf{T}_B^{-1} \\ \mathbf{T}_B \mathbf{S}^{BA} \mathbf{T}_A^{-1} & \mathbf{T}_B \mathbf{S}^{BB} \mathbf{T}_B^{-1} \end{bmatrix} \tag{36}$$

which is the same as those in Eq. (31) when L_A=L_B=0. If, for example, one wishes to evaluate the amplitudes in some point in waveguide **B** distant from the discontinuity by a distance L and the reflected waves in **A** are not to be measured, then $\mathbf{T}_A = \mathbf{I}$ and the equation can still be used.

2.3.1 Finite length discontinuity

In this section, a waveguide with a finite length discontinuity is modelled as composed by two discontinuities. The general formulation for two generic discontinuities can be found in Gravenkamp, Birk and Song (2015).

Figure 4 – Waveguide with two consecutive discontinuities.

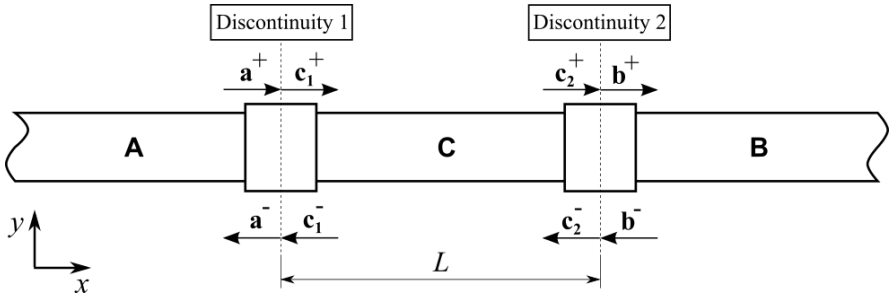

Source: Elaborated by the author

Where L is the distance between the two point discontinuities. Again, the aim is to find the scattering matrix and the reflected and transmitted in waveguides **A** and **B**. To formulate this, each discontinuity is solved individually and the waveguide is divided into three sections as indicated in

Figure 4.

Each component of the wave amplitude is named according to the waveguide they are travelling. e.g. $\mathbf{a}^+$, $\mathbf{b}^+$, $\mathbf{c}_1{}^+$ represents the vectors of wave amplitudes propagating in the positive direction in waveguides **A**, **B** and **C** respectively.

Amplitudes $\mathbf{c}_2^+$ and $\mathbf{c}_1^-$ can be transformed from $\mathbf{c}_1^+$ and $\mathbf{c}_2^-$ as previously described

$$\mathbf{c}_2^+ = \mathbf{T}_C \mathbf{c}_1^+, \qquad \mathbf{c}_1^- = \mathbf{T}_C{}^{-1} \mathbf{c}_2^- \tag{37}$$

where $\mathbf{T}_C$ is a spatial transformation matrix, see Eq. (34).

Applying Eqs. (28) and (31) to each discontinuity, the scattering relationships are given by

$$\begin{Bmatrix} \mathbf{a}^- \\ \mathbf{c}_1^+ \end{Bmatrix} = \begin{bmatrix} \mathbf{S}_1^{AA} & \mathbf{S}_1^{AC} \\ \mathbf{S}_1^{CA} & \mathbf{S}_1^{CC} \end{bmatrix} \begin{Bmatrix} \mathbf{a}^+ \\ \mathbf{c}_1^- \end{Bmatrix} \tag{38}$$

$$\begin{Bmatrix} \mathbf{c}_2^- \\ \mathbf{b}^+ \end{Bmatrix} = \begin{bmatrix} \mathbf{S}_2^{CC} & \mathbf{S}_2^{CB} \\ \mathbf{S}_2^{BC} & \mathbf{S}_2^{BB} \end{bmatrix} \begin{Bmatrix} \mathbf{c}_2^+ \\ \mathbf{b}^- \end{Bmatrix} \tag{39}$$

Substituting Eq. (37) into (38) and (39), results in

$$\begin{Bmatrix} \mathbf{a}^- \\ \mathbf{c}_1^+ \end{Bmatrix} = \begin{bmatrix} \mathbf{S}_1^{AA} & \mathbf{S}_1^{AC}\mathbf{T}_C{}^{-1} \\ \mathbf{S}_1^{CA} & \mathbf{S}_1^{CC}\mathbf{T}_C{}^{-1} \end{bmatrix} \begin{Bmatrix} \mathbf{a}^+ \\ \mathbf{c}_2^- \end{Bmatrix} \tag{40}$$

$$\begin{Bmatrix} \mathbf{c}_2^- \\ \mathbf{b}^+ \end{Bmatrix} = \begin{bmatrix} \mathbf{S}_2^{CC}\mathbf{T}_C & \mathbf{S}_2^{CB} \\ \mathbf{S}_2^{BC}\mathbf{T}_C & \mathbf{S}_2^{BB} \end{bmatrix} \begin{Bmatrix} \mathbf{c}_1^+ \\ \mathbf{b}^- \end{Bmatrix} \tag{41}$$

Since both equations have the **c** amplitudes in common, Eqs. (40) and (41) can be combined into a single matrix, to give

$$\begin{Bmatrix} \mathbf{a}^- \\ \mathbf{b}^+ \end{Bmatrix} = \begin{bmatrix} \mathbf{S}^{AA} & \mathbf{S}^{AB} \\ \mathbf{S}^{BA} & \mathbf{S}^{BB} \end{bmatrix} \begin{Bmatrix} \mathbf{a}^+ \\ \mathbf{b}^- \end{Bmatrix} \tag{42}$$

The reflection and transmission coefficients submatrices in Eq. (42) can be written individually as

$$
\begin{aligned}
\mathbf{S}^{AB} &= \mathbf{S}_1^{AC}\mathbf{T}_C\left(\mathbf{I}-\mathbf{T}_C^{-1}\mathbf{S}_2^{CC}\mathbf{T}_C\mathbf{S}_1^{CC}\right)^{-1}\mathbf{S}_2^{CB} \\
\mathbf{S}^{AA} &= \mathbf{S}_1^{AA}+\mathbf{S}_1^{AC}\mathbf{T}_C\left(\mathbf{I}-\mathbf{T}_C^{-1}\mathbf{S}_2^{CC}\mathbf{T}_C\mathbf{S}_1^{CC}\right)^{-1}\mathbf{S}_2^{CC}\mathbf{T}_C\mathbf{S}_1^{CA} \\
\mathbf{S}^{BA} &= \mathbf{S}_2^{BC}\mathbf{T}_C^{-1}\left(\mathbf{I}-\mathbf{T}_C\mathbf{S}_1^{CC}\mathbf{T}_C^{-1}\mathbf{S}_2^{CC}\right)^{-1}\mathbf{S}_1^{CA} \\
\mathbf{S}^{BB} &= \mathbf{S}_2^{BB}+\mathbf{S}_2^{BC}\mathbf{T}_C^{-1}\left(\mathbf{I}-\mathbf{T}_C\mathbf{S}_1^{CC}\mathbf{T}_C^{-1}\mathbf{S}_2^{CC}\right)^{-1}\mathbf{S}_1^{CC}\mathbf{T}_C^{-1}\mathbf{S}_2^{CB}
\end{aligned}
\tag{43}
$$

where $\mathbf{I}$ is the identity matrix and $\mathbf{b}^- = 0$, since it is considered that there are no waves coming from waveguide **B**.

2.4 ENERGY RELATED QUANTITIES

2.4.1 Introduction

In this section, the formulations for evaluating the energy flow in a waveguide and the power reflection and transmission coefficients are described. These quantities are important when energy is of interest in the analysis. They can also be used as a validation of the numerical results. For example, for conservative discontinuities, the energy flowing into and out of the discontinuity must be equal and therefore the sum of the reflection and transmission power coefficients must be one. In this section, the formulation of the time-averaged kinetic energy and potential energy are also studied. The formulation for the kinetic energy can be evaluated for each DOF, giving important information about the mode conversion that may occur when non-symmetric discontinuities are involved.

2.4.2 Time-averaged energy flow

The increment of work in a particle in movement is given by the product of the force and the displacement (MEIROVITCH, 1970). Also, it is well known that the power, which is the energy flux in a given time interval, is obtained by dividing the energy by the time interval. Therefore, in a general way, the instantaneous power (or energy flow) can be calculated by the product of the instantaneous force and the velocity

$$
\tilde{P} = \frac{\partial(fq)}{\partial t} = f\frac{\partial q}{\partial t} = f\dot{q} \tag{44}
$$

where f is the force and q is the displacement. Here the force is considered constant in time.

Typically, the power is a complex quantity. The imaginary part of the power is called the *reactive part*. This *reactive part* represents the cyclic energy variations, which are due to

the restoring forces from the stiffness and mass of the material. The reactive part is essential for creating the cyclic nature of the waves but does not result in any energy transport (NILSSON; RIEDEL, 1983), therefore in most cases, it is disregarded in the power evaluation. Making an analogy with the electrical systems (OGATA, 1978), the reactive power exists due to capacitances and inductances present in the system and while it is essential for the power to flow in the system, it does not produce work (directly). If the capacitors are analogous to the masses and the inductors to the springs (OGATA, 1978), the reactive power exists due to the mass and stiffness of the structure, however, it does not result in any net energy being transported. As for the *active part*, using the electrical system analogy, it is related to the resistances, which is in turn analogous to the dampers in mechanical systems. The active part of the power corresponds to the real component of the complex power and it is the portion which actually performs work and it is dissipated by the damping of the system. Therefore, the *active part* is the component responsible for making the wave propagate, which results in the actual transportation of energy from one point to another (NILSSON; RIEDEL, 1983).

Although these equations can be directly applied to calculate the power propagated by waves travelling through a waveguide, since the wave motion is a time-dependent harmonic function, the instantaneous power will oscillate with time, making it difficult to evaluate the energy flow. In this case, the time-averaged power can be used.

In order to do this, recall that the real part of a complex number *c* is defined as

$$\mathrm{Re}(c) = \frac{c + c^*}{2} \tag{45}$$

and the imaginary part is defined as

$$\mathrm{Im}(c) = \frac{c - c^*}{2i} \tag{46}$$

Using a complex notation and assuming time-harmonic behaviour, *f* and q are defined as $f = \bar{f}e^{i\omega t}$ and $\dot{q} = (i\omega)\bar{q}e^{i\omega t}$, and are complex amplitudes. Substituting these into Eq. (44) gives

$$\tilde{P} = \mathrm{Re}(f)\,\mathrm{Re}(\dot{q}) = \frac{1}{2}\left(\bar{f}e^{i\omega t} + \bar{f}^* e^{-i\omega t}\right).\frac{1}{2}\left[(i\omega)\bar{q}e^{i\omega t} + (-i\omega)\bar{q}^* e^{-i\omega t}\right] \tag{47}$$

which gives

$$\tilde{P} = \frac{i\omega}{4}\left(-\bar{f}.\,\bar{q}^{*} + \bar{f}^{*}.\,\bar{q} + \bar{f}.\,\bar{q}e^{2i\omega t} - \bar{f}^{*}.\,\bar{q}^{*}e^{-2i\omega t}\right) \tag{48}$$

and can be rewritten as

$$\tilde{P} = \frac{i^2\omega}{2}\left[\frac{\bar{f}^{*}.\,\bar{q} - \left(\bar{f}^{*}.\,\bar{q}\right)^{*}}{2i}\right] + \frac{i^2\omega}{2}\left[\frac{\bar{f}.\,\bar{q}e^{2i\omega t} - \left(\bar{f}.\,\bar{q}e^{2i\omega t}\right)^{*}}{2i}\right] \tag{49}$$

Since the subtraction of a complex value by its conjugate divided by *2i* is the definition of the imaginary part of that complex value, Eq. (46), hence Eq. (49) can be written as a sum of imaginary components.

$$\tilde{P} = \frac{i^2\omega}{2}\left[\mathrm{Im}\left(\bar{f}^{*}.\,\bar{q}\right) + \mathrm{Im}\left(\bar{f}.\,\bar{q}e^{2i\omega t}\right)\right] \tag{50}$$

To evaluate the time-averaged power, the instant power is integrated over a period T and divided by the period itself, that is

$$\Pi = \frac{i^2\omega}{2T}\int_0^T \left[\mathrm{Im}\left(\bar{f}^{*}.\,\bar{q}\right) + \mathrm{Im}\left(\bar{f}.\,\bar{q}e^{2i\omega t}\right)\right] dt \tag{51}$$

Since the second term $\bar{f}.\,\bar{q}e^{2i\omega t}$ has a sinusoidal component, the result of integration is zero and the time-averaged energy flow (Π) is given by

$$\Pi = \frac{i^2\omega}{2}\mathrm{Im}\left(\bar{f}^{*}.\bar{q}\right) \tag{52}$$

2.4.3 Power reflection and transmission coefficients

Another way to evaluate the reflection and transmission in a discontinuity is by calculating the power reflection and transmission coefficients, which represent the power carried by the outgoing wave divided by the power carried by the incoming wave.

As seen previously, the force **f** and displacement **q** can be defined as a function of the eigenvectors $\mathbf{\Phi}_{\mathrm{f}}$ and $\mathbf{\Phi}_{\mathrm{q}}$ (MILLER; FLOTOW; HALL, 1987).

$$\mathbf{f}_{\mathrm{A}} = \boldsymbol{\Phi}^{+}_{\mathrm{f,A}}\mathbf{a}^{+} + \boldsymbol{\Phi}^{-}_{\mathrm{f,A}}\mathbf{a}^{-} = \begin{bmatrix}\boldsymbol{\Phi}^{+}_{\mathrm{f,A}} & \boldsymbol{\Phi}^{-}_{\mathrm{f,A}}\end{bmatrix}\begin{Bmatrix}\mathbf{a}^{+}\\ \mathbf{a}^{-}\end{Bmatrix} = \begin{bmatrix}\boldsymbol{\Phi}^{+}_{\mathrm{f,A}} & \boldsymbol{\Phi}^{-}_{\mathrm{f,A}}\end{bmatrix}\mathbf{a} \tag{53}$$

$$\mathbf{q}_{\mathrm{A}} = \boldsymbol{\Phi}^{+}_{\mathrm{q,A}}\mathbf{a}^{+} + \boldsymbol{\Phi}^{-}_{\mathrm{q,A}}\mathbf{a}^{-} = \begin{bmatrix}\boldsymbol{\Phi}^{+}_{\mathrm{q,A}} & \boldsymbol{\Phi}^{-}_{\mathrm{q,A}}\end{bmatrix}\begin{Bmatrix}\mathbf{a}^{+}\\ \mathbf{a}^{-}\end{Bmatrix} = \begin{bmatrix}\boldsymbol{\Phi}^{+}_{\mathrm{q,A}} & \boldsymbol{\Phi}^{-}_{\mathrm{q,A}}\end{bmatrix}\mathbf{a} \tag{54}$$

Substituting Eqs. (53) and (54) in (52)

$$\boldsymbol{\Pi}_{\mathrm{A}} = \frac{i^2\omega}{2}\,\mathrm{Im}\left(\mathbf{a}^{H}\begin{bmatrix}\boldsymbol{\Phi}^{+}_{\mathrm{f,A}} & \boldsymbol{\Phi}^{-}_{\mathrm{f,A}}\end{bmatrix}^{H}\begin{bmatrix}\boldsymbol{\Phi}^{+}_{\mathrm{q,A}} & \boldsymbol{\Phi}^{-}_{\mathrm{q,A}}\end{bmatrix}\mathbf{a}\right) \tag{55}$$

which becomes

$$\boldsymbol{\Pi}_{\mathrm{A}} = \frac{i^2\omega}{2}\mathbf{a}^{H}\,\mathrm{Im}\begin{bmatrix}{\boldsymbol{\Phi}^{+}_{\mathrm{f,A}}}^{H}\boldsymbol{\Phi}^{+}_{\mathrm{q,A}} & {\boldsymbol{\Phi}^{+}_{\mathrm{f,A}}}^{H}\boldsymbol{\Phi}^{-}_{\mathrm{q,A}}\\ {\boldsymbol{\Phi}^{-}_{\mathrm{f,A}}}^{H}\boldsymbol{\Phi}^{+}_{\mathrm{q,A}} & {\boldsymbol{\Phi}^{-}_{\mathrm{f,A}}}^{H}\boldsymbol{\Phi}^{-}_{\mathrm{q,A}}\end{bmatrix}\mathbf{a} \tag{56}$$

where the *H* is the Hermitian matrix operator and represents the complex conjugate transpose of a matrix.

Defining the power matrix $\mathbf{P}$ as (MILLER; FLOTOW; HALL, 1987)

$$\begin{aligned}\mathbf{P}_{\mathrm{A}} &= i^2\omega\,\mathrm{Im}\begin{bmatrix}{\boldsymbol{\Phi}^{+}_{\mathrm{f,A}}}^{H}\boldsymbol{\Phi}^{+}_{\mathrm{q,A}} & {\boldsymbol{\Phi}^{+}_{\mathrm{f,A}}}^{H}\boldsymbol{\Phi}^{-}_{\mathrm{q,A}}\\ {\boldsymbol{\Phi}^{-}_{\mathrm{f,A}}}^{H}\boldsymbol{\Phi}^{+}_{\mathrm{q,A}} & {\boldsymbol{\Phi}^{-}_{\mathrm{f,A}}}^{H}\boldsymbol{\Phi}^{-}_{\mathrm{q,A}}\end{bmatrix}\\ &= \frac{i\omega}{2}\left\{\begin{bmatrix}{\boldsymbol{\Phi}^{+}_{\mathrm{q,A}}}^{H}\boldsymbol{\Phi}^{+}_{\mathrm{f,A}} & {\boldsymbol{\Phi}^{+}_{\mathrm{q,A}}}^{H}\boldsymbol{\Phi}^{-}_{\mathrm{f,A}}\\ {\boldsymbol{\Phi}^{-}_{\mathrm{q,A}}}^{H}\boldsymbol{\Phi}^{+}_{\mathrm{f,A}} & {\boldsymbol{\Phi}^{-}_{\mathrm{q,A}}}^{H}\boldsymbol{\Phi}^{-}_{\mathrm{f,A}}\end{bmatrix} - \begin{bmatrix}{\boldsymbol{\Phi}^{+}_{\mathrm{f,A}}}^{H}\boldsymbol{\Phi}^{+}_{\mathrm{q,A}} & {\boldsymbol{\Phi}^{+}_{\mathrm{f,A}}}^{H}\boldsymbol{\Phi}^{-}_{\mathrm{q,A}}\\ {\boldsymbol{\Phi}^{-}_{\mathrm{f,A}}}^{H}\boldsymbol{\Phi}^{+}_{\mathrm{q,A}} & {\boldsymbol{\Phi}^{-}_{\mathrm{f,A}}}^{H}\boldsymbol{\Phi}^{-}_{\mathrm{q,A}}\end{bmatrix}\right\}\end{aligned} \tag{57}$$

the averaged power is then given by

$$\Pi_{\mathrm{A}} = \frac{1}{2}\mathbf{a}^{H}\mathbf{P}_{\mathrm{A}}\mathbf{a} \tag{58}$$

Equation (58) can be applied to incident, reflected and transmitted waves, giving

$$\begin{aligned}\Pi_{\mathrm{I}} &= \frac{1}{2}\left(\mathbf{a}^{+}\right)^{H} P^{ii}_{\mathrm{A}}\mathbf{a}^{+}\\ \Pi_{\mathrm{R}} &= \frac{1}{2}\left(\mathbf{a}^{-}\right)^{H} P^{rr}_{\mathrm{A}}\mathbf{a}^{-}\\ \Pi_{\mathrm{T}} &= \frac{1}{2}\left(\mathbf{b}^{+}\right)^{H} P^{tt}_{\mathrm{B}}\mathbf{b}^{+}\end{aligned} \tag{59}$$

where $P_{\mathsf{A}}^{ii}, P_{\mathsf{A}}^{rr}$ and P_{A}^{tt} are the elements of the **P** matrix which corresponds to the incident, reflected and transmitted waves respectively. Since the power matrix **P** has the dimension of *m* by *m* where *m* represents the number of wave modes; *i*, *r*, and *t* are the positions in the diagonal of the **P** matrix, corresponding to the positive going wave in **A**, negative going wave in **A** and positive going wave in **B** respectively.

If a wave travels from a waveguide **A**, which contains the $\mathbf{a}^{+}$ and $\mathbf{a}^{-}$ waves, to waveguide **B**, which contains the $\mathbf{b}^{+}$ and $\mathbf{b}^{-}$ waves, and the reflection and transmission coefficients are given by dividing the reflected and transmitted waves by the incident wave, the power reflection coefficients can be calculated in a similar way by

$$\begin{aligned} \upsilon &= \frac{\Pi_{\mathrm{R}}}{\Pi_{\mathrm{I}}} = \left|S^{\mathsf{AA}}\right|^2 \frac{P_{\mathsf{A}}^{rr}}{P_{\mathsf{A}}^{ii}} \\ \tau &= \frac{\Pi_{\mathrm{T}}}{\Pi_{\mathrm{I}}} = \left|S^{\mathsf{BA}}\right|^2 \frac{P_{\mathsf{B}}^{tt}}{P_{\mathsf{A}}^{ii}} \end{aligned} \tag{60}$$

where $\left(\mathbf{a}^{\pm}\right)^H \mathbf{a}^{\pm} = \left|\mathbf{a}^{\pm}\right|^2$ and $\left(\mathbf{b}^{\pm}\right)^H \mathbf{b}^{\pm} = \left|\mathbf{b}^{\pm}\right|^2$.

2.4.4 Time-averaged kinetic energy and potential energy

The formulations for the kinetic and potential energies of a travelling wave are here calculated. Consider the instantaneous kinetic and potential energies for a particle (MEIROVITCH, 1970)

$$\begin{aligned} \tilde{\Gamma} &= \frac{m\dot{q}^2}{2} \\ \tilde{\Delta} &= \frac{kq^2}{2} \end{aligned} \tag{61}$$

where $\tilde{\Gamma}$ is the instantaneous kinetic energy, $\tilde{\Delta}$ is the instantaneous potential energy, *m* is the mass and *k* is the stiffness of a particle system. Since only one particle is considered, the displacement is only a scalar (*q*).

Considering that the waveguide is modelled using FE and therefore the system is described by several discrete DOF, Eq. (61) can be written in a matrix form

$$\tilde{\Gamma} = \frac{1}{2}\dot{\mathbf{q}}^H \mathbf{M}\dot{\mathbf{q}}$$
$$\tilde{\Delta} = \frac{1}{2}\mathbf{q}^H \mathbf{K}\mathbf{q} \tag{62}$$

In this case, **M** and **K** are the mass and stiffness matrices of the waveguide.

Again, assuming time-harmonic behaviour, the time-average quantities are considered

$$\Gamma = \frac{(i\omega)^2}{4}\mathrm{Re}\left(\mathbf{q}^H \mathbf{M}\mathbf{q}\right)$$
$$\Delta = \frac{1}{4}\mathrm{Re}\left(\mathbf{q}^H \mathbf{K}\mathbf{q}\right) \tag{63}$$

Equations (53) and (54) can be substituted into Eq. (63), giving

$$\Gamma_{\mathrm{A}}^{\pm} = \frac{(i\omega)^2}{4}\left(\mathbf{a}^{\pm}\boldsymbol{\Phi}_{\mathrm{q,A}}^{\pm}\right)^H \mathbf{M}_{\mathrm{A}}\boldsymbol{\Phi}_{\mathrm{q,A}}^{\pm}\mathbf{a}^{\pm}$$
$$\Delta_{\mathrm{A}}^{\pm} = \frac{1}{4}\left(\mathbf{a}^{\pm}\boldsymbol{\Phi}_{\mathrm{q,A}}^{\pm}\right)^H \mathbf{K}_{\mathrm{A}}\boldsymbol{\Phi}_{\mathrm{q,A}}^{\pm}\mathbf{a}^{\pm} \tag{64}$$

where the superscript sign (plus or minus) represents the direction in which the considered wavemode is travelling.

Now suppose that the model considers two degrees of freedom per node, then the vectors of amplitudes are composed as follows

$$\mathbf{a}^{\pm} = \left\{a_{1,x_1}^{\pm} \quad a_{1,x_2}^{\pm} \quad \cdots \quad a_{n,x_1}^{\pm} \quad a_{n,x_2}^{\pm}\right\}^T \tag{65}$$

where *n* is the total number of nodes in the FE model and x_1 is the first degree of freedom and x_2 the second degree of freedom. By identifying each direction of movement in the vector of amplitudes, it is possible to decompose the eigenvectors $\boldsymbol{\Phi}$ in a way that the time-averaged energies are also decomposed into each of the directions of movement allowed by the degrees of freedom. As an example, if the two degrees of freedom are the linear movement in the *x* and *y* directions, the vector of amplitudes are

$$\mathbf{a}^{\pm} = \left\{a_{1,x}^{\pm} \quad a_{1,y}^{\pm} \quad \cdots \quad a_{n,x}^{\pm} \quad a_{n,y}^{\pm}\right\}^T \tag{66}$$

which can be divided into

$$\begin{aligned}\mathbf{a}_x^{\pm} &= \left\{ a_{1,x}^{\pm} \quad \cdots \quad a_{n,x}^{\pm} \right\}^T \\ \mathbf{a}_y^{\pm} &= \left\{ a_{1,y}^{\pm} \quad \cdots \quad a_{n,y}^{\pm} \right\}^T\end{aligned} \tag{67}$$

doing the same decomposition with the nodal displacement matrices $\mathbf{\Phi}_{\mathrm{q,A}}^{\pm}$

$$\begin{aligned}\mathbf{\Phi}_{\mathrm{q},x}^{\pm} &= \left\{ \mathbf{\Phi}_{1,x}^{\pm} \quad \cdots \quad \mathbf{\Phi}_{n,x}^{\pm} \right\}^T \\ \mathbf{\Phi}_{\mathrm{q},y}^{\pm} &= \left\{ \mathbf{\Phi}_{1,y}^{\pm} \quad \cdots \quad \mathbf{\Phi}_{n,y}^{\pm} \right\}^T\end{aligned} \tag{68}$$

applying Eq. (64), the time-averaged kinetic energy can be divided into the *x* and *y* components, giving

$$\begin{aligned}\Gamma_{\mathrm{A},x}^{\pm} &= \frac{(i\omega)^2}{4} \left(\mathbf{a}_x^{\pm} \mathbf{\Phi}_{\mathrm{q},x}^{\pm} \right)^H \mathbf{M}_{\mathrm{A}} \mathbf{\Phi}_{\mathrm{q},x}^{\pm} \mathbf{a}_x^{\pm} \\ \Gamma_{\mathrm{A},y}^{\pm} &= \frac{(i\omega)^2}{4} \left(\mathbf{a}_y^{\pm} \mathbf{\Phi}_{\mathrm{q},y}^{\pm} \right)^H \mathbf{M}_{\mathrm{A}} \mathbf{\Phi}_{\mathrm{q},y}^{\pm} \mathbf{a}_y^{\pm}\end{aligned} \tag{69}$$

The same procedure can be applied to the potential energy. The time-averaged energies can also be related to the incident, reflected and transmitted modes as follows:

- Energy propagating in the positive direction in **A** = incident energy;
- Energy propagating in the negative direction in **A** = reflected energy;
- Energy propagating in the positive direction in **B** = transmitted energy.

where **A** is the waveguide before the discontinuity and **B** is the waveguide after the discontinuity. With this, the time-averaged kinetic energies in the *x*-direction can be written as functions of the type of wave

$$\Gamma_{\mathrm{I}}^{x} = \frac{(i\omega)^2}{4}\left(\mathbf{a}_x^{+}\boldsymbol{\Phi}_{\mathrm{q,A},x}^{+}\right)^{H}\mathbf{M}_{\mathrm{A}}\boldsymbol{\Phi}_{\mathrm{q,A},x}^{+}\mathbf{a}_x^{+}$$
$$\Gamma_{\mathrm{R}}^{x} = \frac{(i\omega)^2}{4}\left(\mathbf{a}_x^{-}\boldsymbol{\Phi}_{\mathrm{q,A},x}^{-}\right)^{H}\mathbf{M}_{\mathrm{A}}\boldsymbol{\Phi}_{\mathrm{q,A},x}^{-}\mathbf{a}_x^{-} \tag{70}$$
$$\Gamma_{\mathrm{T}}^{x} = \frac{(i\omega)^2}{4}\left(\mathbf{b}_x^{+}\boldsymbol{\Phi}_{\mathrm{q,B},x}^{+}\right)^{H}\mathbf{M}_{\mathrm{B}}\boldsymbol{\Phi}_{\mathrm{q,B},x}^{+}\mathbf{b}_x^{+}$$

where the component in the *y*-direction can be calculated in the same way.

2.5 CONCLUSIONS

In this chapter, the procedure for modelling the wave scattering from a discontinuity was studied. In the first part, the WFE method was briefly introduced as a numerical technique to obtain dispersion curves and wavemodes. These were subsequently used to formulate the scattering matrix using a wave matrix formulation.

The evaluation of the scattering matrix for a point discontinuity was introduced and then the formulation was extended to the case of two consecutive discontinuities, which can be used to model a finite length discontinuity, e.g. a notch in a beam or plate.

The equations for calculating energy quantities where shown. In particular, the formulation to evaluate the time-averaged energy flow, the power reflection and transmission coefficients, and the time-averaged kinetic and potential energies were introduced. These quantities can be useful in many cases, for example, to predict the level of dissipation in the discontinuity. In particular, in the next chapters, the transmitted and reflected time-averaged kinetic energy will be studied in terms of their components in the vertical and horizontal direction in order to investigate the complicated mode scattering when multi-modes are involved.

In the next chapter, the wave scattering in rods and beams with different kinds of discontinuities are obtained through analytical formulation, with particular interest on the change of cross-sectional area discontinuity. Later in Chapter 4, the WFE approach is applied to the same problems in Chapter 3, and the results from both approaches are compared.

3 REFLECTION AND TRANSMISSION OF WAVES IN RODS AND BEAMS - ANALYTICAL SOLUTIONS

3.1 INTRODUCTION

In this chapter, the analytical solutions of wave scattering for simple structures are studied. The reflection and transmission of axial and bending waves are studied considering a conservative discontinuity in a rod and in an Euler-Bernoulli beam (GRAFF, 1975). Two kinds of discontinuities are studied using analytical models: an elastic discontinuity modelled as a discrete, spring type point discontinuity and a change of cross-sectional area. The change of cross-sectional area problem is used since it can be representative of damage due to corrosion (DEMMA *et al.*, 2004).

Analytical models for axial vibration in a rod and flexural vibration in a beam are limited to low-frequency range since as the frequency increases, the assumptions in the models are no longer accurate and valid. The main reason for studying these cases is that they consist of simple problems, which can be used to investigate and understand the behaviour of more complicated problems. Moreover, the results can be used as a baseline with which to compare with results obtained by numerical methods such as the WFE, which is applied later.

Using the equations obtained from the analytical solution, the wave matrix formulation is shown and it is used to solve scattering problems. This formulation is later used in conjunction with the WFE.

The problem of two discontinuities is also studied and the scattering coefficients are evaluated. These coefficients are used to solve the problem of two changes in cross-sectional areas for both rods and beams. It is important to note that the problem of changes in cross-sectional areas for these simple cases considers only symmetric changes of cross-sectional area. Equations of motion related to the examples studied in this chapter can be found in the literature, e.g Graff (1975) and Rao (2009).

3.1 REFLECTION AND TRANSMISSION IN RODS

3.1.1 Introduction

In this section, three examples involving rods are studied using an analytical solution. The first case is the problem of a rod connected to an axial spring at a fixed boundary, where only a propagating reflected wave is present. The second case consists of two rods connected by a spring in the middle, where a transmitted wave is also present. The third case studied consists of a rod with a change of cross-sectional area.

3.1.2 Scattering in a rod with a linear spring fixed at its end

Consider the case of a rod connected to a fixed spring, as shown in Figure 5. In this case, the scattering of the waves are due to boundary conditions..

Figure 5 – Incident and reflected longitudinal waves at a spring discontinuity.

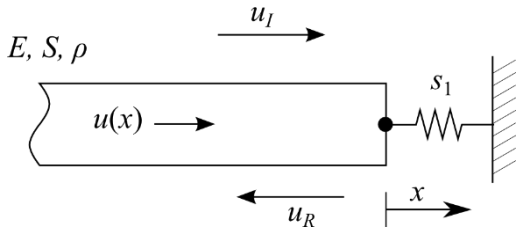

Source: Elaborated by the author

Referring to Figure 5, *E*, *S* and ρ are Young's modulus, cross-sectional area and density respectively. Also, *u* is the total longitudinal mode in the rod, u_I is the incident longitudinal wave and u_R is the reflected wave. The right end of the rod is located at $x = 0$.

By the definition of a rod-type structure or waveguide, only the displacement in the longitudinal direction is considered. Therefore only one kind of wave mode can exist in a rod: the longitudinal or axial mode (RAO, 2009). Assuming a harmonic motion at a frequency ω, the positive going wave is described by (GRAFF, 1975).

$$u_I(x,t) = U_I e^{(i\omega t - ikx)} \tag{71}$$

Where U_I is the complex wave amplitude given by

$$U_I = |U_I| e^{i\phi_I} \tag{72}$$

where ϕ_I is the phase of the complex wave's amplitude.

As this wave impinges upon the right boundary, it is reflected giving rise to a reflected wave u_R as shown in Figure 5, described by

$$u_R(x,t) = U_R e^{(i\omega t + ikx)} \tag{73}$$

where U_R is the complex reflected amplitude, which can also be described by

$$U_R = |U_R| e^{i\phi_R} \tag{74}$$

where ϕ_R is the phase of the complex wave amplitude.

The total longitudinal displacement is the sum of the incident and reflected waves, and is given by

$$u(x) = U_I e^{-ikx} + U_R e^{ikx} \tag{75}$$

Note that Eq. (75) only gives a spatial description of the longitudinal motion, the time component $e^{i\omega t}$ being suppressed for simplicity of the notation.

The axial and elastic forces at the boundary are

$$F(x=0) = ES \frac{\partial u(x=0)}{\partial x} \text{ and } F_s = s_1 u \tag{76}$$

where F is the force applied by the longitudinal wave and F_s is the force generated by the spring.

The equilibrium of forces means that

$$F(x=0) + F_s(x=0) = ES \left.\frac{\partial u}{\partial x}\right|_{x=0} + s_1 u(x=0) = 0 \tag{77}$$

Substituting Eq. (75) into Eq. (77) gives

$$ESk\left(-iU_I + iU_R\right) + s_1\left(U_I + U_R\right) = 0 \tag{78}$$

To solve this the reflection coefficient is defined as

$$R = \frac{U_I}{U_R} \tag{79}$$

Note that *R* is complex.

Substituting Eq. (79) into Eq. (78) gives

$$\left(-i+iR\right)+\alpha\left(1+R\right)=0 \tag{80}$$

where the dimensionless stiffness is defined as

$$\alpha=\frac{s_1}{ESk}=\frac{1}{\sqrt{E\rho S}}\frac{s_1}{\omega} \tag{81}$$

where α is a function of the frequency ω and stiffness s_1.

The reflection coefficient *R* is therefore calculated as

$$R=\frac{-\alpha+i}{\alpha+i} \tag{82}$$

Equation (82) can be evaluated at the limiting cases: $\alpha=0$ and $\alpha\to\infty$, which represents respectively free and fixed ends.

$$\begin{aligned}&\text{free end}\quad \alpha=0\ \ (s_1=0) && \phi_R=0;\ \ |R|=1;\\ &\text{fixed end}\quad \alpha\to\infty\ \ (s_1\to\infty) && \phi_R=180°;\ \ |R|=1\end{aligned} \tag{83}$$

Figure 6 shows the phase change ϕ_R and the magnitude of the reflection coefficient as a function of α. The reflection coefficient was calculated using the parameters from **Table** 3. The values are introduced arbitrarily to study numerical cases.

Table 3 – Rod parameters.

Property	Symbol	Value	Units
Young's Modulus	E	$70x10^{9}$	N/m^2
Density	ρ	$2,7x10^{3}$	kg/m^3
Width	b	14	mm
Thickness	h	2	mm
Element length	L	$12x10^{-3}$	m
Angular frequency	ω	1000	rad/s

Source: Elaborated by the author

Figure 6 – Longitudinal wave reflection coefficient in a rod fixed to a spring. a) Absolute value; b) Phase.

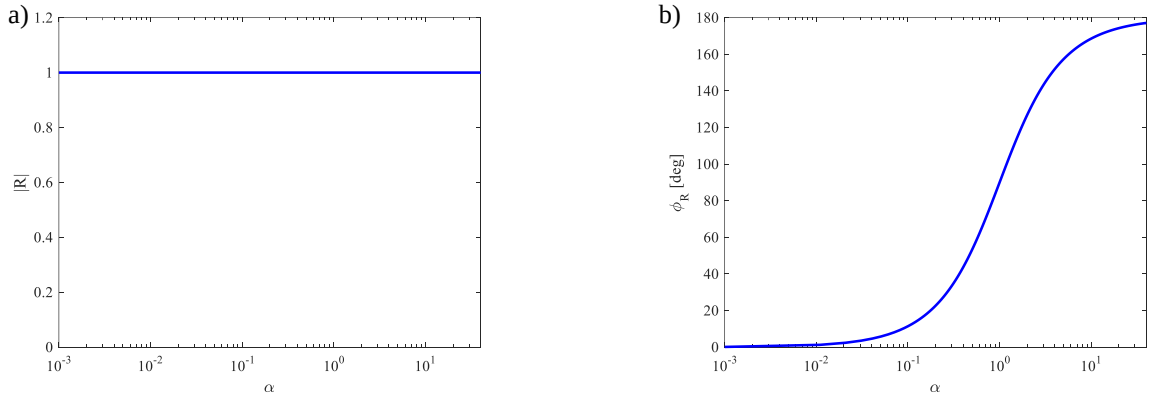

Source: Elaborated by the author

It can be seen from Figure 6 that when α tends to zero the absolute value tends to one with zero phase shift and when α gets larger the absolute value remains one but the phase is shifted to 180º. This result agrees with those presented in Mace (1984).

For this case, independent of the boundary condition, the absolute values of the reflection coefficient will remain 1, which means that the incident wave turns completely into the reflected wave, where the only difference between free and clamped end is the phase shift between the incident wave and reflected wave. This happens because the system is conservative.

According to Mace (1992b), the average energy flow in a waveguide is given by

$$\eta = -\frac{1}{2}\omega^2 Z |U|^2 \tag{84}$$

where η is the energy flux, Z is the characteristic impedance of a waveguide, which for the axial wave is given by $S\sqrt{E\rho}$, U is the displacement wave amplitude. It can be seen that

the energy transported by a wave travelling through a waveguide is proportional to the amplitude squared.

Therefore, if the energy flow of the incident wave is converted completely to the energy of the reflected wave (conservative system), and then the result would be

$$|U_I|^2 = |U_R|^2 \tag{85}$$

In this chapter, only a brief overview of the energy flow in wave scattering problems is shown as a means to verify the results. For the more complex cases, such as the change of cross-sectional area modelled using WFE, the time-averaged kinetic energy and the power coefficients shown in Chapter 2 are used.

3.1.3 Scattering in two rods connected by a spring

Now consider two rods connected by a linear spring modelled using Hooke's Law, as shown in Figure 7.

Figure 7 – Two semi-infinite rods connected by a spring.

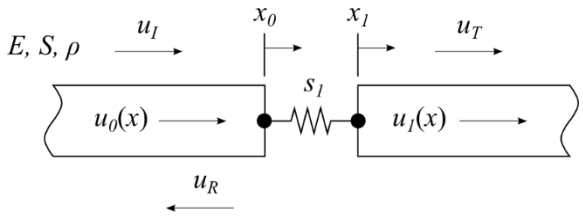

Source: Elaborated by the author

The rod is connected to another rod by a linear spring that acts as a discontinuity to the bar, which is modelled by a linear restoring force $F_s = s_1(u_1 - u_0)$.

Again, incident and reflected waves are defined as in Eq. (71) and Eq. (73).

When the incident wave impinges upon x_0, it is reflected, giving rise to a reflected wave u_R, and transmitted, generating the transmitted wave u_T. Equations (86) and (87) describe the longitudinal displacement at u_0 and u_1

$$u_0(x_0,t) = u_I(x_0,t) + u_R(x_0,t) = U_I e^{(i\omega t - ikx_0)} + U_R e^{(i\omega t + ikx_0)} \tag{86}$$

$$u_1(x_1,t) = u_T(x_1,t) = U_T e^{(i\omega t - ikx_1)} \tag{87}$$

The amplitude U_T is the transmitted wave amplitude, and the complex transmission coefficient can be rewritten as

$$T = \frac{U_T}{U_I}; \tag{88}$$

In this case, the forces at the discontinuity are

$$F_0 = ES \left.\frac{\partial u_0}{\partial x}\right|_{x=x_0} ; \; F_1 = -ES \left.\frac{\partial u_1}{\partial x}\right|_{x=x_1} \tag{89}$$

$$F_{s_0} = s_1\left(u_1 - u_0\right); \; F_{s_1} = -s_1\left(u_1 - u_0\right) \tag{90}$$

The equilibrium of forces at the end of the first rod and at the beginning of the second rod gives

$$F_0 + F_{s_0} = ES \left.\frac{\partial u_0}{\partial x}\right|_{x=x_0} + s_1\left(u_1 - u_0\right) = 0 \tag{91}$$

$$F_1 + F_{s_1} = -ES \left.\frac{\partial u_1}{\partial x}\right|_{x=x_1} - s_1\left(u_1 - u_0\right) = 0 \tag{92}$$

The reflection coefficient is obtained by dividing the problem into two parts. Consider the rightward bar. Substituting Eq. (87) into Eq. (92) it is possible to obtain the relationship between u_0 and u_1

$$u_1 = \frac{u_0}{\left(1 - \frac{i}{\alpha}\right)} \tag{93}$$

where the dimensionless stiffness α is defined in Eq. (81).

Eq. (93) can then be used to eliminate u_1 from Eq. (91)

$$-ES\frac{\partial u_0}{\partial x_0} = \frac{s_1 u_0}{\left(1-\frac{iESk}{s_1}\right)} - s_1 u_0 \tag{94}$$

The reflection coefficient R can be obtained by substituting Eq. (86) and (79) into (94)

$$R = \frac{i}{\left(-2\alpha + i\right)} = \frac{1-i2\alpha}{\left(4\alpha^2+1\right)} \tag{95}$$

Equation (95) can be simplified when $\alpha = 0$ and $\alpha \to \infty$ representing respectively common cases of simple boundary conditions.

$$\begin{array}{ll} \text{free end} \quad \alpha = 0 \ (s_1 = 0) & \phi_R = 0; \ |R| = 1; \\ \text{joined bars} \quad \alpha \to \infty \ (s_1 \to \infty) & \phi_R = -90°; \ |R| = 0 \end{array} \tag{96}$$

Figure 8 shows the phase change ϕ_R and the absolute value of the reflection coefficient as a function of α. In this case, the reflection and transmission coefficients were calculated using the parameters from Table 1 for both rods.

Figure 8 – Longitudinal wave reflection coefficient in a spring discontinuity. a) Absolute value; b) Phase.

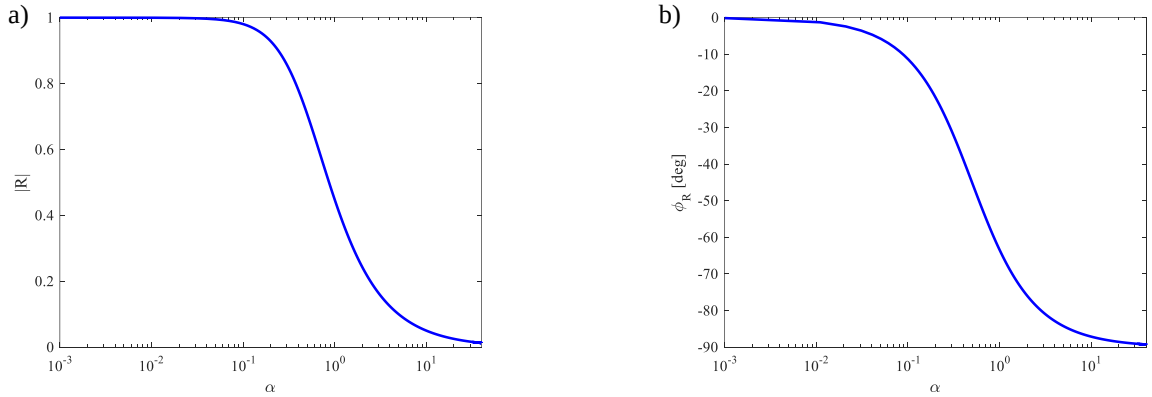

Source: Elaborated by the author

As for the coefficients, by substituting Eq. (95) into Eq. (79), the amplitude of the reflected wave is obtained

$$U_R = \frac{i}{(-2\alpha + i)} U_I \tag{97}$$

then substituting Eq. (97) in Eq. (92), the transmission coefficient becomes

$$T = \frac{-2\alpha}{-2\alpha + i} = 2\alpha \frac{2\alpha + i}{4\alpha^2 + 1} \tag{98}$$

Again, Eq. (98) can be simplified when $\alpha = 0$ and $\alpha \to \infty$ representing respectively common cases of simply boundary conditions.

$$\begin{aligned} &\text{free end} \quad \alpha = 0 \ (s_1 = 0) && \phi_T = 90°; \ |T| = 0; \\ &\text{joined bars} \quad \alpha \to \infty \ (s_1 \to \infty) && \phi_T = 0; \ |T| = 1 \end{aligned} \tag{99}$$

Figure 9 shows the phase change ϕ_T and the absolute value of the transmission coefficient as a function of α.

Figure 9 – Longitudinal wave transmission coefficient in a spring discontinuity. a) Absolute value; b) Phase.

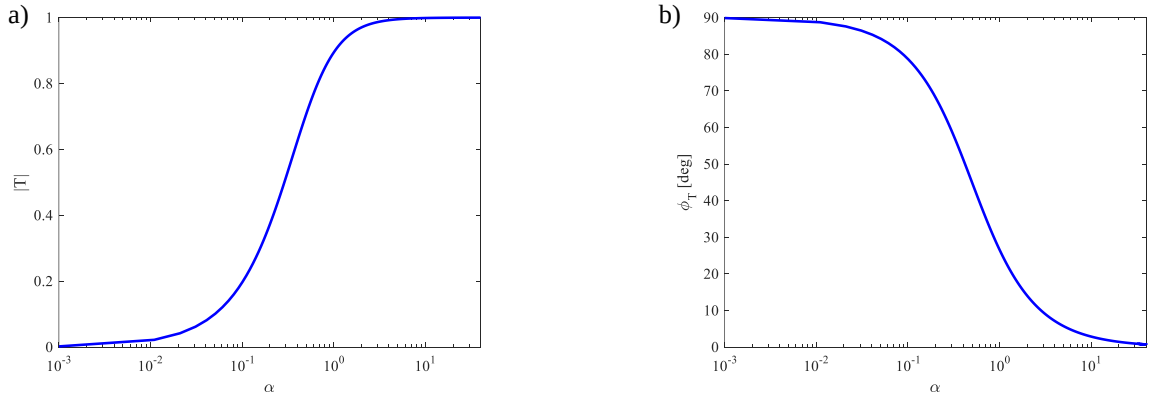

Source: Elaborated by the author

As in the previous case, the coefficients obtained correspond to the ones found in the literature.

3.1.4 Scattering in a rod at a change of cross-sectional area

Consider a rod connected to another rod with different thickness as shown in Figure 10.

Figure 10 – Longitudinal waves at a change of cross-sectional area.

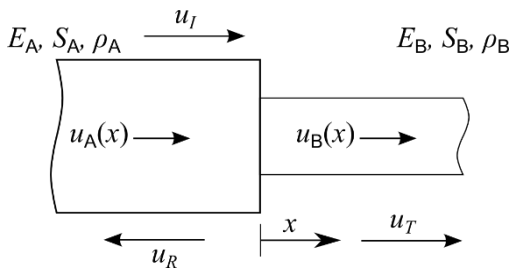

Source: Elaborated by the author

The rod is unbounded at the left side and connected to another unbounded rod to the right as shown in Figure 10. The right end of the first rod is located at $x = 0$.

With this, the wave displacements can be written as

$$u_A(x,t) = U_I e^{(i\omega t - ik_A x)} + U_R e^{(i\omega t + ik_A x)} \tag{100}$$

$$u_B(x,t) = U_T e^{(i\omega t - ik_B x)} \tag{101}$$

and the forces

$$f_A(x,t) = E_A S_A \frac{\partial u_A}{\partial x} \tag{102}$$

$$f_B(x,t) = E_B S_B \frac{\partial u_B}{\partial x} \tag{103}$$

in this case, there are two boundary conditions at x_0: equilibrium of forces (105) and continuity (104).

$$u_A - u_B = 0 \tag{104}$$

$$f_A - f_B = 0 \tag{105}$$

Using these equations, the reflection as transmission coefficients can be calculated, where the reflection and transmission coefficients are defined as

$$R = \frac{U_R}{U_I} \text{ and } T = \frac{U_T}{U_I} \tag{106}$$

substituting Eq. (100) and (101) in (104) and considering $x = 0$

$$U_I + U_R = U_T \tag{107}$$

which can be written as a function of the reflection and transmission coefficients in Eq. (106), giving

$$1 + R = T \tag{108}$$

doing the same with Eq. (105) gives

$$-1 + R = -\beta T \tag{109}$$

where the dimensionless proportionality constant is defined as

$$\beta = \frac{E_{\mathrm{B}} S_{\mathrm{B}} k_{\mathrm{B}}}{E_{\mathrm{A}} S_{\mathrm{A}} k_{\mathrm{A}}} = \frac{E_{\mathrm{B}} S_{\mathrm{B}}}{E_{\mathrm{A}} S_{\mathrm{A}}} \sqrt{\frac{\rho_{\mathrm{B}} E_{\mathrm{A}}}{\rho_{\mathrm{A}} E_{\mathrm{B}}}} \frac{\omega}{\omega} = \frac{\sqrt{E_{\mathrm{B}} \rho_{\mathrm{B}}} S_{\mathrm{B}}}{\sqrt{E_{\mathrm{A}} \rho_{\mathrm{A}}} S_{\mathrm{A}}} \tag{110}$$

Note that β is a function the area only if the material is the same in **A** and **B**. Additionally, if the width of the rod is fixed, β is a function of the thickness (*h*) only.

Isolating the reflection coefficient *R* gives

$$R = \frac{1 - \beta}{1 + \beta} \tag{111}$$

Equation (111) can be evaluated at the limiting cases: $\beta = 0$, $\beta = 1$ and $\beta \to \infty$, which represents respectively common cases of simple boundary conditions. When β is or tends to zero means that the cross-sectional area of the second rod is very small, which relates to the behaviour of a free end rod. When β tends to infinity means that the second rod is very big,

corresponding to the fixed end condition. When $\beta = 1$ the areas are equal, so the rod can be seen as a single homogeneous rod.

$$\begin{aligned} &\text{free end} \quad \beta = 0 \quad (S_{\mathrm{A}} \gg S_{\mathrm{B}}) && \phi_R = 0; \ |R| = 1; \\ &\text{continuous bar} \quad \beta = 1 \quad (S_{\mathrm{A}} = S_{\mathrm{B}}) && \phi_R = 0; \ |R| = 0; \\ &\text{fixed end} \quad \beta \to \infty \quad (S_{\mathrm{A}} \ll S_{\mathrm{B}}) && \phi_R = 180°; \ |R| = 1 \end{aligned} \tag{112}$$

Figure 11 shows the phase change ϕ_R and the absolute value of reflection coefficient *R* as a function of β. The reflection and transmission coefficients were calculated using the parameters from Table 1, but here the thickness of the second section depends on β.

Figure 11 – Longitudinal wave reflection coefficient in a cross-sectional area change. a) Absolute value; b) Phase.

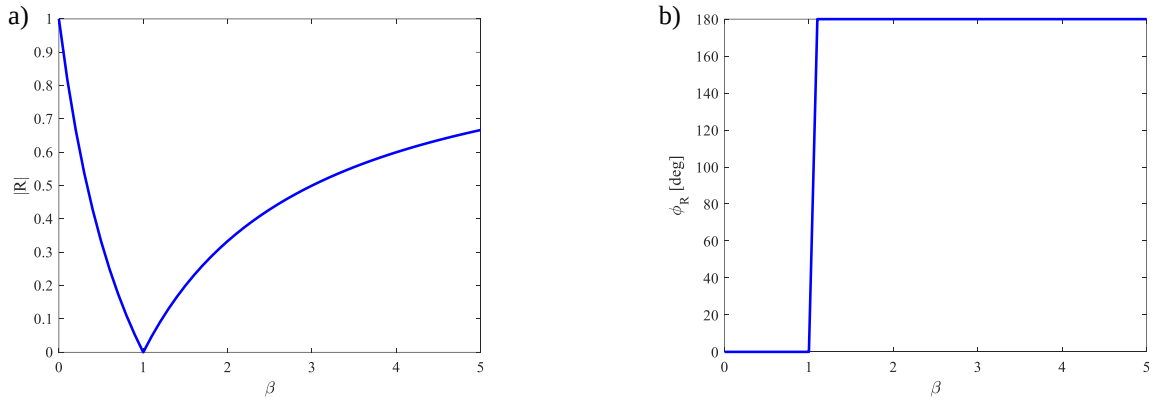

Source: Elaborated by the author

It can be noted that the results agree with the limiting case analysis in Eq. (112): if $\beta = 0$ then the longitudinal wave is reflected as in a free end, if $\beta = 1$ then there is no reflection since the cross-sectional areas are equal and as $\beta \to \infty$ the wave is reflected as a fixed end.

Now for the transmission coefficient, using Eq. (108) and Eq. (109) isolating *T*, giving

$$T = \frac{2}{1+\beta} \tag{113}$$

Again, Eq. (113) can be simplified when $\beta = 0$, $\beta = 1$ and $\beta \to \infty$ representing respectively common cases of simply boundary conditions, that is

$$\begin{aligned} &\text{free end} \quad \beta = 0 \ (S_A \gg S_B) && \phi_T = 0;\ |T| = 2; \\ &\text{continuous bar} \quad \beta = 1 \ \ (S_A = S_B) && \phi_T = 0;\ |T| = 1; \\ &\text{fixed end} \quad \beta \to \infty \ (S_A \ll S_B) && \phi_T = 0;\ |T| = 0 \end{aligned} \tag{114}$$

Figure 12 shows the phase change ϕ_T and the absolute value of transmission coefficient T as a function of β.

Figure 12 – Longitudinal wave transmission coefficient in a cross-sectional area change. a) Absolute value; b) Phase.

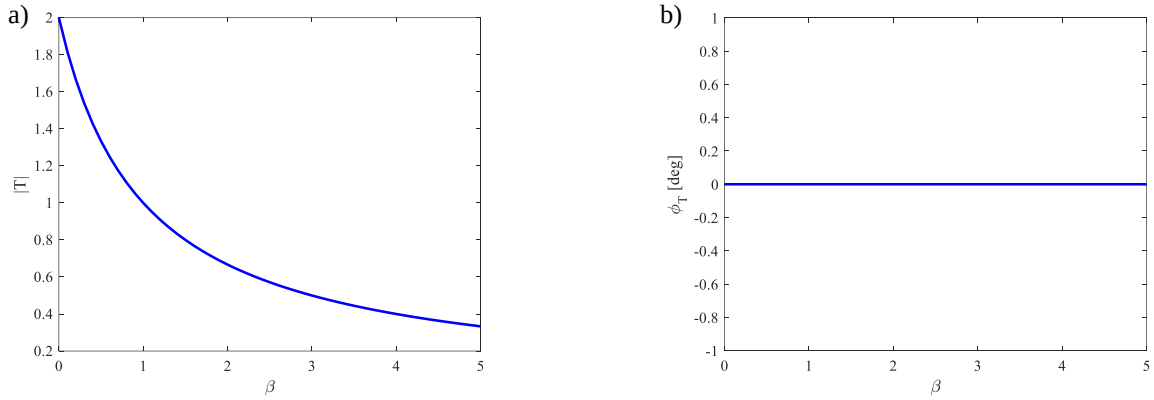

Source: Elaborated by the author

The results match the results shown by Graff (1975) and Kinsler (2000), but it can be noted that in this case, the amplitude of the transmission coefficients are bigger than 1 when the second area is smaller than the first area ($0 \le \beta < 1$). This means that the smaller is the second area, the bigger is the transmission coefficient. To understand this, the energy flow can be calculated. Eq. (115) and Eq. (116) show the reflected and transmitted power respectively obtained from Eq. (84).

$$P_R = |R|^2 \tag{115}$$

$$P_T = |T|^2 \ \beta = 1 - R \tag{116}$$

Using Eq. (111) and (113) in (115) and (116) respectively

$$P_R = \left(\frac{1-\beta}{1+\beta} \right)^2 \tag{117}$$

$$P_T = \frac{4\beta}{(1+\beta)^2} \tag{118}$$

Using Eq. (117) for $\beta \to 0$ it can be noted that the reflected power is 1 and Eq. (118) shows that the transmitted power is 0. This means that all the energy is carried by the reflected wave.

This analysis can be carried for $\beta = 1$, where $P_R = 0$ and $P_T = 1$ mean that the energy goes all to the transmitted wave, and for $\beta \to \infty$, where $P_R \simeq 1$ and $P_T \simeq 0$ mean that all the energy is carried by the reflected wave. Therefore, it can be seen that the power coefficient can be used as a way to check reflection and transmission results since, for a conservative structure, the sum of all the powers must be always unity, whereas the coefficients themselves can be bigger than one.

3.2 REFLECTION AND TRANSMISSION IN BEAMS

3.2.1 Introduction

In this section, three examples of discontinuities are studied considering a beam. In the first, the beam is fixed at its end by a linear transverse spring and a torsional spring. The second example consists of an infinite beam fixed in the middle by a transverse spring and the third case consists of a beam with a change of cross-sectional area.

3.2.2 Scattering in a beam fixed by springs at its end

Consider a semi-infinite Euler-Bernoulli beam with a linear spring in the transverse direction and a torsional spring at the end, as shown in Figure 13.

Figure 13 – Reflection of flexural waves at springs discontinuity.

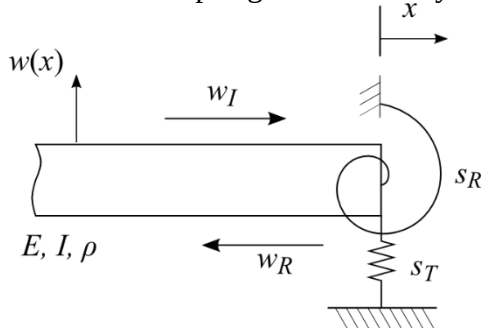

Source: Elaborated by the author

The beam is unbounded at the left side and constrained by a linear spring and a torsional spring at the right side. The linear spring exerts a transverse restoring linear force $F_s = s_T w$ and the torsion spring exerts a restoring bending moment $M_s = s_R \theta = s_R \dfrac{\partial w}{\partial x}$.

For the beam waveguide, the incident wave is composed of a bending propagating mode and a nearfield mode as

$$w_I(x,t) = W_{\mathrm{I_p}} e^{i\omega t - ikx} + W_{\mathrm{I_N}} e^{i\omega t - kx} \tag{119}$$

where $W_{\mathrm{I_p}}$ and $W_{\mathrm{I_N}}$ are the complex amplitudes of the bending propagating and nearfield modes respectively.

The incident wave is reflected at the right boundary, giving rise to a reflected propagating wave and a reflected evanescent wave.

$$w_R = W_{\mathrm{R_p}} e^{i\omega t + ikx} + W_{\mathrm{R_N}} e^{i\omega t + kx} \tag{120}$$

where $W_{\mathrm{R_p}}$ is the amplitude of the propagating reflected wave and $W_{\mathrm{R_N}}$ is the amplitude of the nearfield reflected wave, and they are related to the incident wave amplitude through the reflection coefficients. Both waves (propagating and nearfield) travels in the negative direction of x. With this, the transverse displacement at any point of the beam is given by

$$w(x,t) = w_I(x,t) + w_R(x,t) \tag{121}$$

For the bending case, the forces are composed of shear force and bending moment, which are calculated by

$$V = EI \frac{\partial^3 w}{\partial x^3} \text{ and } M = EI \frac{\partial^2 w}{\partial x^2} \tag{122}$$

therefore, the forces on the beam are

$$\begin{aligned} V_0 &= EI\frac{\partial^3 w}{\partial x^3};\ F_s = -s_T w \\ M_0 &= EI\frac{\partial^2 w}{\partial x^2};\ M_s = -s_R\frac{\partial w}{\partial x} \end{aligned} \tag{123}$$

and the equilibrium of forces becomes

$$\begin{cases} V_0(x_0) + F_s(x_0) = EI\left.\dfrac{\partial^3 w}{\partial x^3}\right|_{x_0} - s_T w(x_0) = 0 \\ M_0(x_0) + M_s(x_0) = EI\left.\dfrac{\partial^2 w}{\partial x^2}\right|_{x_0} - s_R\dfrac{\partial w(x_0)}{\partial x} = 0 \end{cases} \tag{124}$$

The reflected wave is given by Eq. (120). Substituting Eq. (119) and (120) into Eq. (124)

$$\begin{cases} EIk^3\left(iW_{\mathrm{I_P}} - W_{\mathrm{I_N}} - iW_{\mathrm{R_P}} + W_{\mathrm{R_N}}\right) - S_T\left(W_{\mathrm{I_P}} + W_{\mathrm{I_N}} + W_{\mathrm{R_P}} + W_{\mathrm{R_N}}\right) = 0 \\ EIk^2\left(-W_{\mathrm{I_P}} + W_{\mathrm{I_N}} - W_{\mathrm{R_P}} + W_{\mathrm{R_N}}\right) - S_R k\left(-iW_{\mathrm{I_P}} - W_{\mathrm{I_N}} + iW_{\mathrm{R_P}} + W_{\mathrm{R_N}}\right) = 0 \end{cases} \tag{125}$$

defining the dimensionless stiffness α_R and α_T

$$\alpha_T = \frac{s_T}{EIk^3} \tag{126}$$

$$\alpha_R = \frac{s_R}{EIk} \tag{127}$$

and rearranging the variables gives

$$\begin{cases} \left(1 - i\alpha_T\right)W_{\mathrm{R_P}} + \left(i - i\alpha_T\right)W_{\mathrm{R_N}} = \left(1 + i\alpha_T\right)W_{\mathrm{I_P}} + \left(i + i\alpha_T\right)W_{\mathrm{I_N}} \\ \left(-1 + i\alpha_R\right)W_{\mathrm{R_P}} + \left(1 + \alpha_R\right)W_{\mathrm{R_N}} = \left(1 + i\alpha_R\right)W_{\mathrm{I_P}} + \left(-1 + \alpha_R\right)W_{\mathrm{I_N}} \end{cases} \tag{128}$$

Following Mace's procedure (MACE, 1984), the wave amplitudes are grouped into 2x1 vectors of the incident and reflected waves as

$$\mathbf{w}_I = \begin{Bmatrix} W_{I_P} \\ W_{I_N} \end{Bmatrix}; \quad \mathbf{w}_R = \begin{Bmatrix} W_{R_P} \\ W_{R_N} \end{Bmatrix} \tag{129}$$

Using Eq. (129), the following matrix system can be obtained

$$\begin{bmatrix} 1-i\alpha_T & i-i\alpha_T \\ -1+i\alpha_R & 1+\alpha_R \end{bmatrix} \mathbf{w}_R = \begin{bmatrix} 1+i\alpha_T & i+i\alpha_T \\ 1+i\alpha_R & -1+\alpha_R \end{bmatrix} \mathbf{w}_I \tag{130}$$

which gives the reflection coefficient matrix

$$\mathbf{R} = \begin{bmatrix} 1-i\alpha_T & i-i\alpha_T \\ -1+i\alpha_R & 1+\alpha_R \end{bmatrix}^{-1} \begin{bmatrix} 1+i\alpha_T & i+i\alpha_T \\ 1+i\alpha_R & -1+\alpha_R \end{bmatrix} \tag{131}$$

The elements of the **R** matrix can be defined as

$$\mathbf{R} = \begin{bmatrix} R_{\mathrm{PP}} & R_{\mathrm{NP}} \\ R_{\mathrm{PN}} & R_{\mathrm{NN}} \end{bmatrix} = \begin{bmatrix} \left.\dfrac{W_{\mathrm{R_P}}}{W_{\mathrm{I_P}}}\right|_{W_{\mathrm{I_N}}=0} & \left.\dfrac{W_{\mathrm{R_P}}}{W_{\mathrm{I_N}}}\right|_{W_{\mathrm{I_P}}=0} \\ \left.\dfrac{W_{\mathrm{R_N}}}{W_{\mathrm{I_P}}}\right|_{W_{\mathrm{I_N}}=0} & \left.\dfrac{W_{\mathrm{R_N}}}{W_{\mathrm{I_N}}}\right|_{W_{\mathrm{I_P}}=0} \end{bmatrix} \tag{132}$$

where:

- R_{PP} is the reflection coefficient for the propagating reflected wave when there is a propagating incident wave;
- R_{PN} is the reflection coefficient for the nearfield reflected wave when there is a propagating incident wave;
- R_{NP} is the reflection coefficient for the propagating reflected wave when there is a nearfield incident wave;

- R_{NN} is the reflection coefficient for the nearfield reflected wave when there is a nearfield incident wave.

As an example, here the reflection matrix is calculated for the case where there is only a transverse linear spring.

If only a propagating wave $W_{\mathrm{I_P}} e^{(i\omega t - ikx)}$ is incident upon the boundary ($W_{\mathrm{I_N}} = 0$), the reflection coefficients R_{PP} and R_{PN} can be calculated using Eq. (133).

$$\begin{aligned} &|R_{\mathrm{PP}}| = 1; && |R_{\mathrm{PN}}| = \sqrt{2/(2\alpha_T{}^2 - 2\alpha_T + 1)}; \\ &\phi_{\mathrm{R_{PP}}} = \tan^{-1}\left[(2\alpha_T - 1)/(2\alpha_T - 2\alpha_T{}^2)\right]; && \phi_{\mathrm{R_{PN}}} = \tan^{-1}(2\alpha_T - 1). \end{aligned} \tag{133}$$

Equation (133) can be simplified when $\alpha_T = 0$ and $\alpha_T \to \infty$.

$$\begin{aligned} &\alpha_T = 0 \ (s_T = 0) && \phi_{\mathrm{R_{PP}}} = -90°;\ |R_{\mathrm{PP}}| = 1;\ \phi_{\mathrm{R_{PN}}} = -45°;\ |R_{\mathrm{PN}}| = \sqrt{2}; \\ &\alpha_T \to \infty \ (s_T \to \infty) && \phi_{\mathrm{R_{PP}}} = 180°;\ |R_{\mathrm{PP}}| = 1;\ \phi_{\mathrm{R_{PN}}} = 90°;\ |R_{\mathrm{PN}}| = 0; \end{aligned} \tag{134}$$

These two conditions correspond to the free end condition and simply supported condition respectively. The nearfield incident case is not studied in this work since generally, the nearfield mode does not travel considerable distances and it is not useful in practical applications.

When $\alpha_T = 0$, the response is analogous to the free end condition and when $\alpha_T \to \infty$ the response is analogous to the simply supported condition. The clamped condition would be obtained when $\alpha_T \to \infty$ and $\alpha_R \to \infty$.

The absolute value and phase of the reflection coefficients are given in Figure 14 as a function α_{T}. For the beam examples, the parameters used are those from **Table** 3.

Figure 14 – Flexural wave reflection at spring discontinuity – only incident propagating wave. a) Absolute value; b) Phase. Dashed red line **- -** : nearfield reflection coefficient R_{PN} ; solid blue line **—** : reflection coefficient R_{PP} .

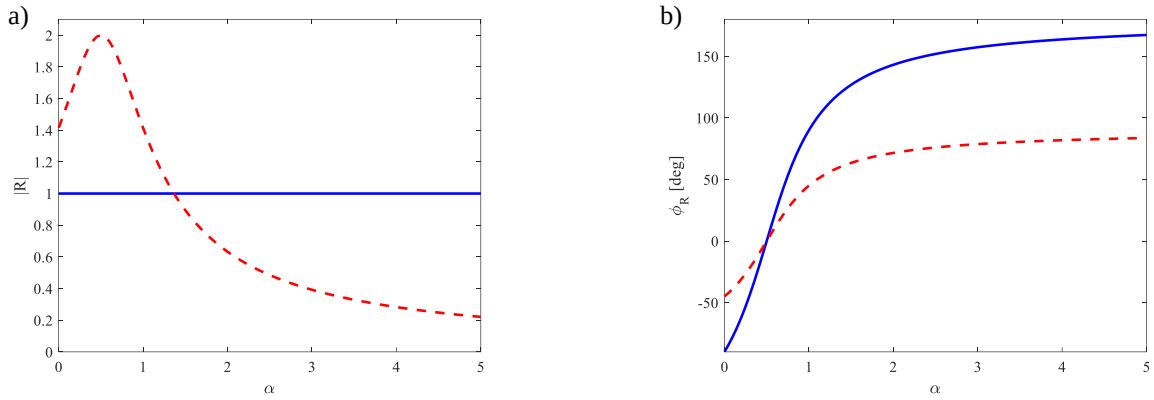

Source: Elaborated by the author

For low frequency range, these results match the limiting case results and the results found in the literature (MACE, 1984).

3.2.3 Scattering in an infinite beam fixed by springs in the middle

Consider an Euler-Bernoulli beam with a linear spring in the transverse direction and a torsional spring positioned in the middle, as depicted in Figure 15.

Figure 15 – Reflection and transmission of flexural waves at a spring discontinuity.

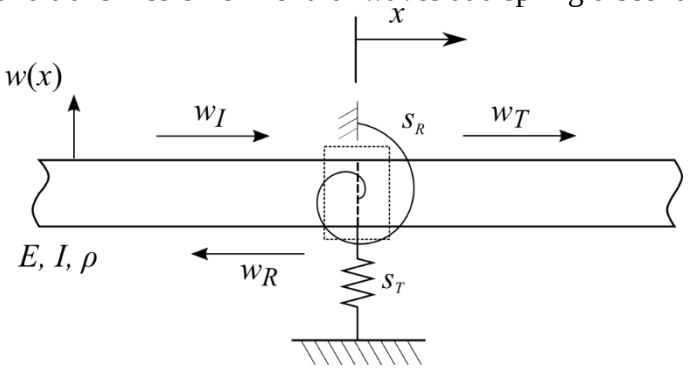

Source: Elaborated by the author

The incident and reflected waves are the same as those defined in Eq. (119) and Eq. (120) respectively, and the transmitted wave is defined by

$$w_t(x,t) = W_{T_P} e^{i\omega t - ikx} + W_{T_N} e^{i\omega t - kx} \tag{135}$$

Leftward and rightward vertical displacements w_0 and w_1 at $x=0$ are defined in Eq. (136).

$$w_0(x) = w_I + w_R;\ \ w_1(x) = w_{\mathrm{T}} \tag{136}$$

Equilibrium of forces and moments and continuity of displacements and rotations at $x=0$ are given in Eq. (137).

$$\begin{cases} w_0(0) = w_1(0) \\ w_0'(0) = w_1'(0) \\ V_0(0) + V_1(0) + V_s = 0 \\ M_0(0) + M_1(0) + M_s = 0 \end{cases} \tag{137}$$

where V and M are the shear force and bending moment, defined as

$$V_0 = EI\frac{\partial^3 w_0}{\partial x^3};\ V_1 = -EI\frac{\partial^3 w_1}{\partial x^3};\ V_{\mathrm{s}} = -s_T w \tag{138}$$

$$M_0 = EI\frac{\partial^2 w_0}{\partial x^2};\ M_1 = -EI\frac{\partial^2 w_1}{\partial x^2};\ M_s = -s_R\frac{\partial w}{\partial x} \tag{139}$$

using these Eq. (137) can be written as a function of the amplitudes

$$\begin{cases} W_{\mathrm{I_P}} + W_{\mathrm{I_N}} + W_{\mathrm{R_P}} + W_{\mathrm{R_N}} = W_{\mathrm{T_P}} + W_{\mathrm{T_N}} \\ -iW_{\mathrm{I_P}} - W_{\mathrm{I_N}} + iW_{\mathrm{R_P}} + W_{\mathrm{R_N}} = -iW_{\mathrm{T_P}} - W_{\mathrm{T_N}} \\ iW_{\mathrm{I_P}} - W_{\mathrm{I_N}} - iW_{\mathrm{R_P}} + W_{\mathrm{R_N}} = iW_{\mathrm{T_P}} - W_{\mathrm{T_N}} + \alpha_T W_{\mathrm{T_P}} + \alpha_T W_{\mathrm{T_N}} \\ -W_{\mathrm{I_P}} + W_{\mathrm{I_N}} - W_{\mathrm{R_P}} + W_{\mathrm{R_N}} = -W_{\mathrm{T_P}} + W_{\mathrm{T_N}} - i\alpha_R W_{\mathrm{T_P}} - \alpha_R W_{\mathrm{T_N}} \end{cases} \tag{140}$$

To simplify the solution of the equations system in Eq. (140) are grouped into two by two matrices as follows

$$\begin{bmatrix} 1 & 1 \\ -i & -1 \end{bmatrix}\mathbf{a}_I + \begin{bmatrix} 1 & 1 \\ i & 1 \end{bmatrix}\mathbf{a}_R = \begin{bmatrix} 1 & 1 \\ -i & -1 \end{bmatrix}\mathbf{a}_T \tag{141}$$

$$\begin{bmatrix} i & -1 \\ -1 & 1 \end{bmatrix}\mathbf{a}_I + \begin{bmatrix} -i & 1 \\ -1 & 1 \end{bmatrix}\mathbf{a}_R = \begin{bmatrix} \alpha_T + i & \alpha_T - 1 \\ -i\alpha_R - 1 & -\alpha_R + 1 \end{bmatrix}\mathbf{a}_T \tag{142}$$

where α_T and α_R are defined in Eq. (126) and (127) respectively, while $\mathbf{a}_I$, $\mathbf{a}_R$ and $\mathbf{a}_T$ are vectors containing the amplitudes as shown in Eq. (143).

$$\mathbf{a}_I = \begin{Bmatrix} W_{\mathrm{I_P}} \\ W_{\mathrm{I_N}} \end{Bmatrix};\ \mathbf{a}_R = \begin{Bmatrix} W_{\mathrm{R_P}} \\ W_{\mathrm{R_N}} \end{Bmatrix};\ \mathbf{a}_T = \begin{Bmatrix} W_{\mathrm{T_P}} \\ W_{\mathrm{T_N}} \end{Bmatrix} \tag{143}$$

Naming each matrix as

$$\begin{aligned} &\mathbf{A} = \begin{bmatrix} 1 & 1 \\ -i & -1 \end{bmatrix};\ \mathbf{B} = \begin{bmatrix} 1 & 1 \\ i & 1 \end{bmatrix};\ \mathbf{C} = \begin{bmatrix} 1 & 1 \\ -i & -1 \end{bmatrix} \\ &\mathbf{D} = \begin{bmatrix} i & -1 \\ -1 & 1 \end{bmatrix};\ \mathbf{E} = \begin{bmatrix} -i & 1 \\ -1 & 1 \end{bmatrix};\ \mathbf{F} = \begin{bmatrix} \alpha_T + i & \alpha_T - 1 \\ -i\alpha_R - 1 & -\alpha_R + 1 \end{bmatrix} \end{aligned} \tag{144}$$

Equations (141) and (142) then becomes

$$\mathbf{A}\mathbf{a}_I + \mathbf{B}\mathbf{a}_R = \mathbf{C}\mathbf{a}_T \tag{145}$$

$$\mathbf{D}\mathbf{a}_I + \mathbf{E}\mathbf{a}_R = \mathbf{F}\mathbf{a}_T \tag{146}$$

Again, considering the effect of the torsional spring and by using the notation from Eq. (145) and Eq. (146), the solution of the system is much simpler. Starting from Eq. (146)

$$\mathbf{F}^{-1}\left(\mathbf{D}\mathbf{a}_I + \mathbf{E}\mathbf{a}_R\right) = \mathbf{a}_T \tag{147}$$

substituting Eq. (147) into Eq. (145) gives

$$\mathbf{A}\mathbf{a}_I + \mathbf{B}\mathbf{a}_R = \mathbf{C}\left(\mathbf{F}^{-1}\mathbf{D}\mathbf{a}_I + \mathbf{F}^{-1}\mathbf{E}\mathbf{a}_R\right) \tag{148}$$

which can be simplified as follows

$$\mathbf{a}_R = \mathbf{R}\mathbf{a}_I \tag{149}$$

where

$$\mathbf{R} = \left(\mathbf{B} - \mathbf{C}\mathbf{F}^{-1}\mathbf{E}\right)^{-1}\left(\mathbf{C}\mathbf{F}^{-1}\mathbf{D} - \mathbf{A}\right) \tag{150}$$

The reflection coefficients matrix elements are defined in the same manner as in Eq. (132). The reflection coefficients R_{PP}, R_{PN} and the phases ϕ_{PP} and ϕ_{PN} can be calculated by defining the incident near field wave as zero ($W_{\mathrm{I_N}} = 0$)

$$\begin{aligned} &|R_{\mathrm{PP}}| = \sqrt{\alpha_T{}^2 / 2(\alpha_T{}^2 - 4\alpha_T + 8)}; \quad |R_{\mathrm{PN}}| = \sqrt{\alpha_T{}^2 / 2(\alpha_T{}^2 - 4\alpha_T + 8)}; \\ &\phi_{\mathrm{PP}} = \tan^{-1}\left[(\alpha_T - 4)/\alpha_T\right]; \qquad \phi_{\mathrm{PN}} = \tan^{-1}\left[-\alpha_T/(\alpha_T - 4)\right]. \end{aligned} \tag{151}$$

Limit cases where $\alpha = 0$ and $\alpha \to \infty$ can be considered, that is

$$\begin{aligned} &\alpha_T = 0 \ (s_T = 0) && \phi_{\mathrm{PP}} = 90°; \ |R_{\mathrm{PP}}| = 0; \ \phi_{\mathrm{PN}} = 0; \ |R_{\mathrm{PN}}| = 0 \\ &\alpha_T \to \infty \ (s_T \to \infty) && \phi_{\mathrm{PP}} = -135°; \ |R_{\mathrm{PP}}| = \sqrt{2}/2; \ \phi_{\mathrm{PN}} = 135°; \ |R_{\mathrm{PN}}| = \sqrt{2}/2; \end{aligned} \tag{152}$$

Again, $\alpha_T = 0$ is analogous to the free end condition and $\alpha_T \to \infty$ is analogous to the simply supported condition.

Figure 16 shows the absolute value of the reflection coefficients and the phases.

Figure 16 – Flexural wave reflection at spring discontinuity in the middle of an infinite beam. a) Absolute value; b) Phase. Dashed red line **- -** : nearfield reflection coefficient R_{PN} ; solid blue line **—** : reflection coefficient R_{PP} .

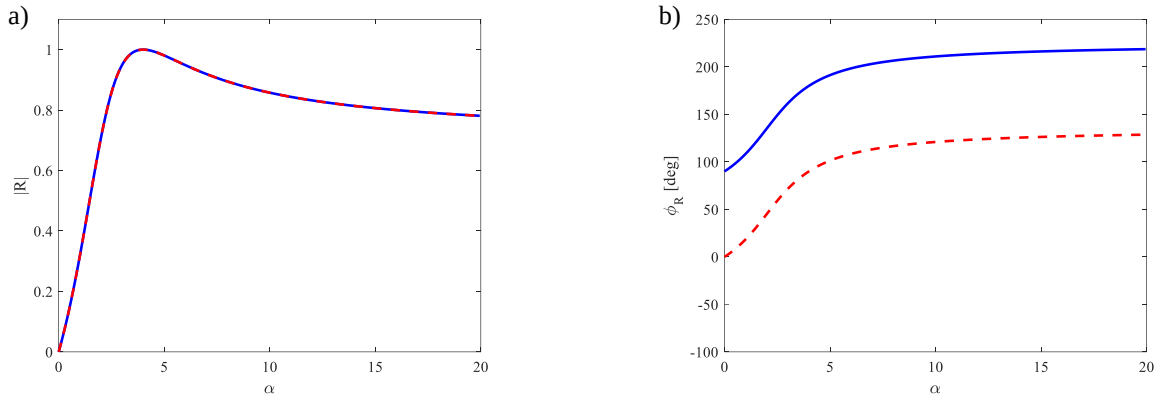

Source: Elaborated by the author

It can be seen that the limiting cases for $\alpha_t = 0$ and $\alpha_t \to \infty$ give correctly the results for the free and simply supported boundary conditions.

The results obtained in Figure 16 can be compared with the results from Mace (1984) and the results from Eq. (152). In both cases, the results match with the literature.

The transmission coefficients T_{PP} , T_{PN} and the phases ϕ_{PP} and ϕ_{PN} can be calculated by defining the incident near field wave as zero ($W_{I_N} = 0$).

$$\begin{aligned} |T_{PP}| &= \sqrt{(\alpha-4)^2 / 2(\alpha^2-4\alpha+8)}; \quad |T_{PN}| = \sqrt{\alpha^2 / 2(\alpha^2-4\alpha+8)}; \\ \phi_{PP} &= \tan^{-1}\left[-\alpha/(\alpha-4)\right]; \qquad \phi_{PN} = \tan^{-1}\left[-\alpha/(\alpha-4)\right]. \end{aligned} \tag{153}$$

For $\alpha = 0$ and $\alpha \to \infty$ Eq. (84) gives

$$\begin{aligned} &\alpha = 0 \ (s_1 = 0) && \phi_{PP} = 0;\ |T_{PP}| = 1;\ \phi_{PN} = 0;\ |T_{PN}| = 0 \\ &\alpha \to \infty \ (s_1 \to \infty) && \phi_{PP} = -45°;\ |T_{PP}| = \sqrt{2}/2;\ \phi_{PN} = 135°;\ |T_{PN}| = \sqrt{2}/2; \end{aligned} \tag{154}$$

Figure 17 shows the absolute value and phase of the transmission coefficients

Figure 17 – Flexural wave transmission at spring discontinuity in the middle of an infinite beam. a) Absolute value; b) Phase. Dashed red line **- -** : nearfield transmission coefficient T_{PP} ; solid blue line **—** : reflection coefficient T_{PN} .

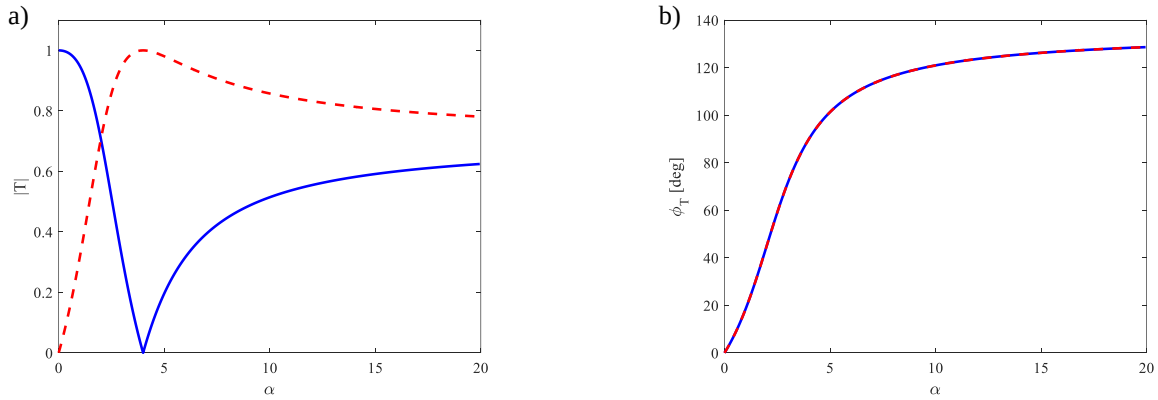

Source: Elaborated by the author

These results match exactly the results presented by Mace (1984).

3.2.4 Scattering in a beam at a change of cross-sectional area

In this section, the same problem of the previous section is studied for the bending wave considering a change in the cross-section. Figure 18 shows the representation of the problem, where **q** is the vector composed of the vertical and angular displacements.

Figure 18 – Flexural waves at a change of cross-sectional area.

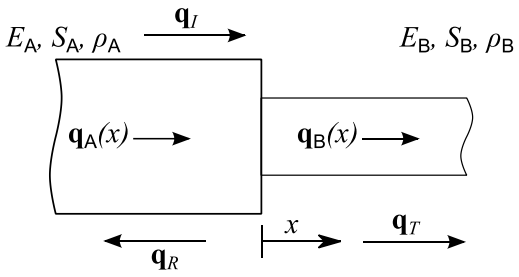

Source: Elaborated by the author

The displacements in **A** and **B** are given by

$$\mathbf{q}_A = \begin{Bmatrix} w_A(x_0,t) \\ \theta_A(x_0,t) \end{Bmatrix} \text{ and } \mathbf{q}_B = \begin{Bmatrix} w_B(x_0,t) \\ \theta_B(x_0,t) \end{Bmatrix} \tag{155}$$

while the internal forces are

$$\mathbf{f}_{\mathrm{A}}=\begin{Bmatrix} V_{\mathrm{A}}\left(x_0,t\right) \\ M_{\mathrm{A}}\left(x_0,t\right) \end{Bmatrix} \text{ and } \mathbf{f}_{\mathrm{B}}=\begin{Bmatrix} V_{\mathrm{B}}\left(x_0,t\right) \\ M_{\mathrm{B}}\left(x_0,t\right) \end{Bmatrix} \tag{156}$$

The individual displacements can be written as

$$\begin{cases} w_{\mathrm{A}}\left(x_0,t\right)=W_{\mathrm{IP}}e^{(i\omega t-ik_{\mathrm{A}}x_0)}+W_{\mathrm{IN}}e^{(i\omega t-k_{\mathrm{A}}x_0)}+W_{\mathrm{RP}}e^{(i\omega t+ik_{\mathrm{A}}x_0)}+W_{\mathrm{RN}}e^{(i\omega t+k_{\mathrm{A}}x_0)} \\ w_{\mathrm{B}}\left(x_0,t\right)=W_{\mathrm{TP}}e^{(i\omega t-ik_{\mathrm{B}}x_0)}+W_{\mathrm{TN}}e^{(i\omega t-k_{\mathrm{B}}x_0)} \\ \theta_{\mathrm{A}}\left(x_0,t\right)=\left.\dfrac{\partial w_{\mathrm{A}}}{\partial x}\right|_{x=0} \\ \theta_{\mathrm{B}}\left(x_0,t\right)=\left.\dfrac{\partial w_{\mathrm{B}}}{\partial x}\right|_{x=0} \end{cases} \tag{157}$$

The shear forces and bending moments are given by

$$\begin{cases} V_{\mathrm{A}}\left(x_0,t\right)=E_{\mathrm{A}}I_{\mathrm{A}}\left.\dfrac{\partial^3 w_{\mathrm{A}}}{\partial x^3}\right|_{x=0} \\ V_{\mathrm{B}}\left(x_0,t\right)=E_{\mathrm{B}}I_{\mathrm{B}}\left.\dfrac{\partial^3 w_{\mathrm{B}}}{\partial x^3}\right|_{x=0} \\ M_{\mathrm{A}}\left(x_0,t\right)=E_{\mathrm{A}}I_{\mathrm{A}}\left.\dfrac{\partial^2 w_{\mathrm{A}}}{\partial x^2}\right|_{x=0} \\ M_{\mathrm{B}}\left(x_0,t\right)=E_{\mathrm{B}}I_{\mathrm{B}}\left.\dfrac{\partial^2 w_{\mathrm{B}}}{\partial x^2}\right|_{x=0} \end{cases} \tag{158}$$

and the boundary conditions are

$$\begin{aligned} &\mathbf{q}_{\mathrm{A}}-\mathbf{q}_{\mathrm{B}}=\mathbf{0} \\ &\mathbf{f}_{\mathrm{A}}-\mathbf{f}_{\mathrm{B}}=\mathbf{0} \end{aligned} \tag{159}$$

Substituting Eq. (155) and (156) in (159) and writing in a matrix form gives

$$\begin{bmatrix} 1 & 1 \\ -i\sqrt{\beta} & -\sqrt{\beta} \end{bmatrix}\mathbf{w}_I+\begin{bmatrix} 1 & 1 \\ i\sqrt{\beta} & \sqrt{\beta} \end{bmatrix}\mathbf{w}_R=\begin{bmatrix} 1 & 1 \\ -i & 1 \end{bmatrix}\mathbf{w}_T \tag{160}$$

where

$$\mathbf{w}_I = \begin{Bmatrix} W_{\mathrm{IP}} \\ W_{\mathrm{IN}} \end{Bmatrix},\ \mathbf{w}_R = \begin{Bmatrix} W_{\mathrm{RP}} \\ W_{\mathrm{RN}} \end{Bmatrix} \text{ and } \mathbf{w}_T = \begin{Bmatrix} W_{\mathrm{TP}} \\ W_{\mathrm{TN}} \end{Bmatrix} \tag{161}$$

Here β is a proportion between h_{A} and h_{B} which are the thicknesses of the beams. Considering that the material and width of **A** and **B** are the same, β is defined as in Eq. (162).

$$\beta = \frac{h_{\mathsf{B}}}{h_{\mathsf{A}}} \tag{162}$$

Doing the same with the last two equations of Eq. (159) the matrix equation becomes

$$\begin{bmatrix} i & -1 \\ -1 & 1 \end{bmatrix} \mathbf{w}_I + \begin{bmatrix} -i & 1 \\ -1 & 1 \end{bmatrix} \mathbf{w}_R = \begin{bmatrix} j\gamma & -\gamma \\ -\varepsilon & \varepsilon \end{bmatrix} \mathbf{w}_T \tag{163}$$

where

$$\gamma = \frac{E_{\mathsf{B}} I_{\mathsf{B}} k_{\mathsf{B}}{}^3}{E_{\mathsf{A}} I_{\mathsf{A}} k_{\mathsf{A}}{}^3} = \left(\frac{h_{\mathsf{B}}}{h_{\mathsf{A}}} \right)^{3/2} = \beta^{3/2} \tag{164}$$

$$\varepsilon = \frac{E_{\mathsf{B}} I_{\mathsf{B}} k_{\mathsf{B}}{}^2}{E_{\mathsf{A}} I_{\mathsf{A}} k_{\mathsf{A}}{}^2} = \left(\frac{h_{\mathsf{B}}}{h_{\mathsf{A}}} \right)^{2} = \beta^{2} \tag{165}$$

The matrices of Eqs. (160) and (163) can be written in a compact form as

$$\mathbf{C}_1 \mathbf{W}_I + \mathbf{C}_2 \mathbf{W}_R = \mathbf{C}_3 \mathbf{W}_T \tag{166}$$

$$\mathbf{C}_4 \mathbf{W}_I + \mathbf{C}_5 \mathbf{W}_R = \mathbf{C}_6 \mathbf{W}_T \tag{167}$$

In this case, **R** and **T** are given by

$$\mathbf{R} = \mathbf{W}_I{}^{-1} \mathbf{W}_R \text{ and } \mathbf{T} = \mathbf{W}_I{}^{-1} \mathbf{W}_T \tag{168}$$

which gives

$$\mathbf{C}_1 + \mathbf{C}_2 \mathbf{R} = \mathbf{C}_3 \mathbf{T} \tag{169}$$

$$\mathbf{C}_4 + \mathbf{C}_5 \mathbf{R} = \mathbf{C}_6 \mathbf{T} \tag{170}$$

The reflection matrix is then calculated by

$$\mathbf{R} = \left(\mathbf{C}_5 - \mathbf{C}_6\mathbf{C}_3^{-1}\mathbf{C}_2\right)^{-1}\left(\mathbf{C}_6\mathbf{C}_3^{-1}\mathbf{C}_1 - \mathbf{C}_4\right) \tag{171}$$

Now consider only a propagating incident wave W_{I_p}. The reflection coefficients R_{PP} and R_{PN} can be calculated using Eq. (171), where the subscripts *P* and *N* indicates the type of wavemode, the first letter indicates the incident wave mode and the second the scattered wavemode, therefore R_{PN} indicates bending propagating incident and nearfield reflected.

Equation (171) can be simplified in the limit cases when $\beta = 0$, $\beta = 1$ and $\beta \to \infty$.

$$\begin{aligned}
&\text{free end} \quad \beta = 0 \ (S_A \gg S_B) && \phi_{R_{PP}} = -90^o;\ |R_{PP}| = 1;\ \phi_{R_{PN}} = -45^o;\ |R_{PN}| = \sqrt{2};\\
&\text{continuous beam} \quad \beta = 1 \ (S_A = S_B) && \phi_{R_{PP}} = 0;\ |R_{PP}| = 0;\ \phi_{R_{PN}} = 0;\ |R_{PN}| = 0;\\
&\text{fixed end} \quad \beta \to \infty \ (S_A \ll S_B) && \phi_{R_{PP}} = -90^o;\ |R_{PP}| = 1;\ \phi_{R_{PN}} = 135^o;\ |R_{PN}| = \sqrt{2}
\end{aligned} \tag{172}$$

As done in previous cases, the absolute value and phase of the reflection coefficients are given in Figure 19.

Figure 19 – Bending wave reflection at an area change discontinuity – only propagating incident wave. a) Absolute value. b) Phase. Dashed red line **- -** : nearfield reflection coefficient R_{PN}; solid blue line **—** : propagating reflection coefficient R_{PP}.

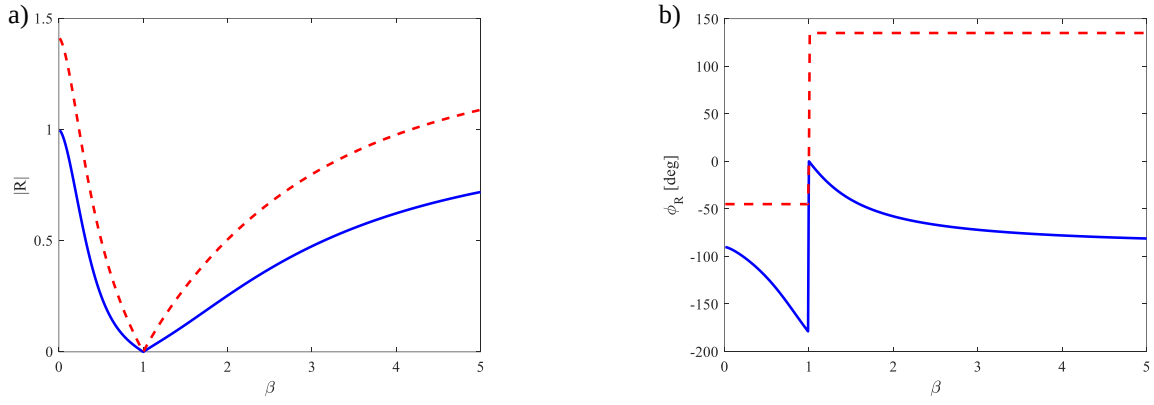

Source: Elaborated by the author

Again, to check the solutions, the results obtained for the free and fixed end for a beam in bending motion can be used. As it can be noted looking at the propagating reflected results in Figure 19, when $\beta = 0$ the absolute value is 1 and phase is -90°, when $\beta = 1$ the absolute

value is zero and phase is also zero and finally when $\beta \to \infty$ the absolute value tends to 1 and the phase is back to -90°.

Using the same procedure as with the reflection matrix, the transmission matrix is calculated by

$$\mathbf{T} = \left(\mathbf{C}_6 - \mathbf{C}_5\mathbf{C}_2^{-1}\mathbf{C}_3\right)^{-1}\left(-\mathbf{C}_5\mathbf{C}_2^{-1}\mathbf{C}_1 + \mathbf{C}_4\right) \tag{173}$$

Equation (173) can be simplified when $\beta = 0$, $\beta = 1$ and $\beta \to \infty$.

$$\begin{aligned}
&\text{free end} \quad \beta = 0 \ (S_\mathrm{A} \gg S_\mathrm{B}) && \phi_{T_{PP}} = 0^\mathrm{o};\ |T_{PP}| = 2;\ \phi_{T_{PN}} = -90^\mathrm{o};\ |T_{PN}| = 2; \\
&\text{continuous beam} \quad \beta = 1 \ (S_\mathrm{A} = S_\mathrm{B}) && \phi_{T_{PP}} = 0;\ |T_{PP}| = 1;\ \phi_{T_{PN}} = 0;\ |T_{PN}| = 0; \\
&\text{fixed end} \quad \beta \to \infty \ (S_\mathrm{A} \ll S_\mathrm{B}) && \phi_{T_{PP}} = 0^\mathrm{o};\ |T_{PP}| = 0;\ \phi_{T_{PN}} = 0^\mathrm{o};\ |T_{PN}| = 0
\end{aligned} \tag{174}$$

The absolute value and phase of the reflection coefficients are given in Figure 20.

Figure 20 – Bending wave transmission at an area change discontinuity – only incident propagating wave. a) Absolute value; b) Phase. Dashed red line **- -**: Nearfield transmission coefficient T_{PN}; solid blue line **—**: Propagating transmission coefficient T_{PP}.

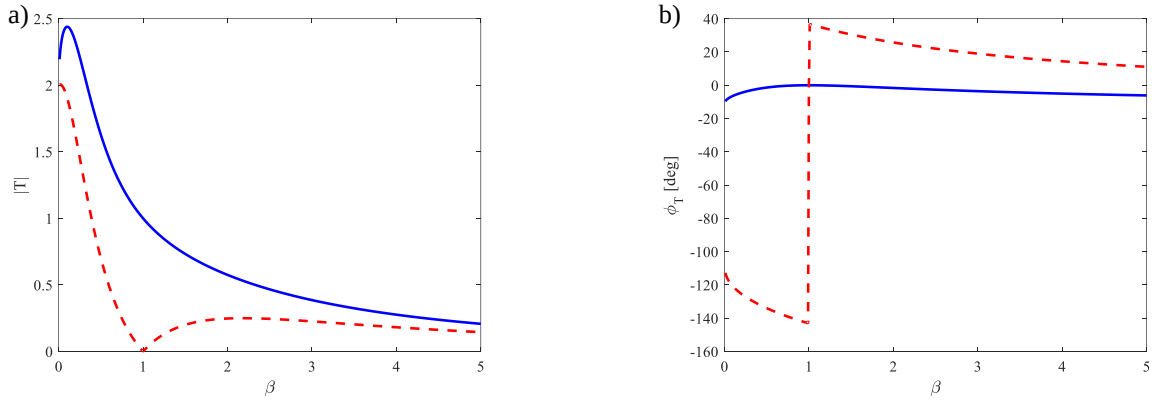

Source: Elaborated by the author

Again, the power flow is calculated for the propagating incident wave related to the reflected and transmitted propagating waves. This is done using Eq. (115) and Eq. (116).

$$\begin{aligned}
&\beta = 0 \ (S_\mathrm{A} \gg S_\mathrm{B}) && P_{R_{PP}} = 1;\ P_{T_{PP}} = 0; \\
&\beta = 1 \ (S_\mathrm{A} = S_\mathrm{B}) && P_{R_{PP}} = 0;\ P_{T_{PP}} = 1; \\
&\beta \to \infty \ (S_\mathrm{A} \ll S_\mathrm{B}) && P_{R_{PP}} = 1;\ P_{T_{PP}} = 0;
\end{aligned} \tag{175}$$

As shown in Eq. (175), the results are similar to the longitudinal wave example.

3.3 WAVE MATRIX FORMULATION

3.3.1 Introduction

In sections 3.1 and 3.2 analytical solutions for the reflection and transmission coefficients for rods and beams were shown. However, it was also shown that each type of waveguide requires its own equation, making it impractical for implementation of numerical methods such as the WFE (HARLAND; MACE; JONES, 2001). Here the wave matrix formulation shown in Section 2.3 is applied. The displacements and forces using wave matrix formulation are given by

$$\begin{aligned}
\mathbf{q}_{\mathrm{A}} &= \boldsymbol{\Phi}^{+}_{\mathrm{q,A}}\mathbf{a}^{+} + \boldsymbol{\Phi}^{-}_{\mathrm{q,A}}\mathbf{a}^{-} \\
\mathbf{f}_{\mathrm{A}} &= \boldsymbol{\Phi}^{+}_{\mathrm{f,A}}\mathbf{a}^{+} + \boldsymbol{\Phi}^{-}_{\mathrm{f,A}}\mathbf{a}^{-} \\
\mathbf{q}_{\mathrm{B}} &= \boldsymbol{\Phi}^{+}_{\mathrm{q,B}}\mathbf{b}^{+} + \boldsymbol{\Phi}^{-}_{\mathrm{q,B}}\mathbf{b}^{-} \\
\mathbf{f}_{\mathrm{B}} &= \boldsymbol{\Phi}^{+}_{\mathrm{f,B}}\mathbf{b}^{+} + \boldsymbol{\Phi}^{-}_{\mathrm{f,B}}\mathbf{b}^{-}
\end{aligned} \tag{176}$$

and the scattering matrix is written as

$$\begin{Bmatrix} \mathbf{a}^{-} \\ \mathbf{b}^{+} \end{Bmatrix} = \begin{bmatrix} \mathbf{C}_{\mathrm{A}}\boldsymbol{\Phi}^{-}_{\mathrm{q,A}} & -\mathbf{C}_{\mathrm{B}}\boldsymbol{\Phi}^{+}_{\mathrm{q,B}} \\ \mathbf{D}_{\mathrm{A}}\boldsymbol{\Phi}^{-}_{\mathrm{f,A}} & -\mathbf{D}_{\mathrm{B}}\boldsymbol{\Phi}^{+}_{\mathrm{f,B}} \end{bmatrix}^{-1} \begin{bmatrix} -\mathbf{C}_{\mathrm{A}}\boldsymbol{\Phi}^{+}_{\mathrm{q,A}} & \mathbf{C}_{\mathrm{B}}\boldsymbol{\Phi}^{-}_{\mathrm{q,B}} \\ -\mathbf{D}_{\mathrm{A}}\boldsymbol{\Phi}^{+}_{\mathrm{f,A}} & \mathbf{D}_{\mathrm{B}}\boldsymbol{\Phi}^{-}_{\mathrm{f,B}} \end{bmatrix} \begin{Bmatrix} \mathbf{a}^{+} \\ \mathbf{b}^{-} \end{Bmatrix} \tag{177}$$

As examples, the problem of a change of cross-sectional area for the rod and beam are solved using the wave matrix formulation.

3.3.2 Matrix Formulation for the Rod

Consider the displacement equations in Eq. (100) and Eq. (101) rewritten as follows

$$u_{\mathrm{A}} = U^{+}_{\mathrm{A}} e^{-ik^{+}_{\mathrm{A}}x_0} + U^{-}_{\mathrm{A}} e^{ik^{-}_{\mathrm{A}}x_0} \tag{178}$$

$$u_{\mathrm{B}} = U^{+}_{\mathrm{B}} e^{-ik^{+}_{\mathrm{B}}x_0} + U^{-}_{\mathrm{B}} e^{ik^{+}_{\mathrm{B}}x_0} \tag{179}$$

To simplify the notation, $u(x,t)=u$ and $f(x,t)=f$ are used, and the time and phase components are omitted since they do not interfere in the present equations.

The forces are obtained using Eq. (102) and Eq. (103), which becomes

$$f_{\mathrm{A}} = E_{\mathrm{A}} S_{\mathrm{A}} \left(-ik_{\mathrm{A}}^{+} U_{\mathrm{A}}^{+} e^{-ik_{\mathrm{A}}^{+} x_0} + ik_{\mathrm{A}}^{-} U_{\mathrm{A}}^{-} e^{ik_{\mathrm{A}}^{-} x_0} \right) \tag{180}$$

$$f_{\mathrm{B}} = E_{\mathrm{B}} S_{\mathrm{B}} \left(-ik_{\mathrm{B}}^{+} U_{\mathrm{B}}^{+} e^{-ik_{\mathrm{B}}^{+} x_0} + ik_{\mathrm{B}}^{-} U_{\mathrm{B}}^{-} e^{ik_{\mathrm{B}}^{-} x_0} \right) \tag{181}$$

Now defining the vector of wave amplitudes as

$$\mathbf{a}^{+} = U_{\mathrm{A}}^{+} e^{-ik_{\mathrm{A}}^{+} x_0},\ \mathbf{a}^{-} = U_{\mathrm{A}}^{-} e^{ik_{\mathrm{A}}^{-} x_0},\ \mathbf{b}^{+} = U_{\mathrm{B}}^{+} e^{-ik_{\mathrm{B}}^{+} x_0} \text{ and } \mathbf{b}^{-} = U_{\mathrm{B}}^{-} e^{ik_{\mathrm{B}}^{-} x_0} \tag{182}$$

The displacement equations can be written in the matrix notation, becoming

$$\mathbf{u}_{\mathrm{A}} = \mathbf{a}^{+} + \mathbf{a}^{-} \tag{183}$$

$$\mathbf{u}_{\mathrm{B}} = \mathbf{b}^{+} + \mathbf{b}^{-} \tag{184}$$

and the forces

$$\mathbf{f}_{\mathrm{A}} = E_{\mathrm{A}} S_{\mathrm{A}} \left(-ik_{\mathrm{A}}^{+} \mathbf{a}^{+} + ik_{\mathrm{A}}^{-} \mathbf{a}^{-} \right) \tag{185}$$

$$\mathbf{f}_{\mathrm{B}} = E_{\mathrm{B}} S_{\mathrm{B}} \left(-ik_{\mathrm{B}}^{+} \mathbf{b}^{+} + ik_{\mathrm{B}}^{-} \mathbf{b}^{-} \right) \tag{186}$$

In this particular case, since the rod waveguide only allows one degree of freedom, there is only one wavemode present, making the displacements vectors single scalars. The vector notation was kept to maintain a correspondence with Eq. (28).

With this, the wave mode matrices $\mathbf{\Phi}$ can be found by comparing Eqs. (183) – (186) with Eq. (176), giving

$$\mathbf{\Phi}_{\mathrm{q,A}}^{+} = 1,\ \mathbf{\Phi}_{\mathrm{q,A}}^{-} = 1,\ \mathbf{\Phi}_{\mathrm{q,B}}^{+} = 1,\ \mathbf{\Phi}_{\mathrm{q,B}}^{-} = 1 \tag{187}$$

$$\mathbf{\Phi}_{\mathrm{f,A}}^{+} = -iE_{\mathrm{A}} S_{\mathrm{A}} k_{\mathrm{A}}^{+},\ \mathbf{\Phi}_{\mathrm{f,A}}^{-} = iE_{\mathrm{A}} S_{\mathrm{A}} k_{\mathrm{A}}^{-},\ \mathbf{\Phi}_{\mathrm{f,B}}^{+} = -iE_{\mathrm{B}} S_{\mathrm{B}} k_{\mathrm{B}}^{+},\ \mathbf{\Phi}_{\mathrm{f,B}}^{-} = iE_{\mathrm{B}} S_{\mathrm{B}} k_{\mathrm{B}}^{-} \tag{188}$$

Again the wave mode matrices $\mathbf{\Phi}$ are also single scalars.

With this and by setting proper boundary conditions, the scattering matrix can be calculated using Eq. (28).The scattering coefficients obtained using wave matrix formulation are compared with the analytical solution obtained previously in Figure 21.

Figure 21 – Comparison of the reflection and transmission coefficients obtained with the wave matrix formulation for a rod. a) Absolute value of the reflection coefficient; b) Phase of the reflection coefficient; c) Absolute value of the transmission coefficient; d) Phase of the transmission coefficient. Blue continuous line —: Analytical solution; Red dashed line - -: wave matrix formulation solution.

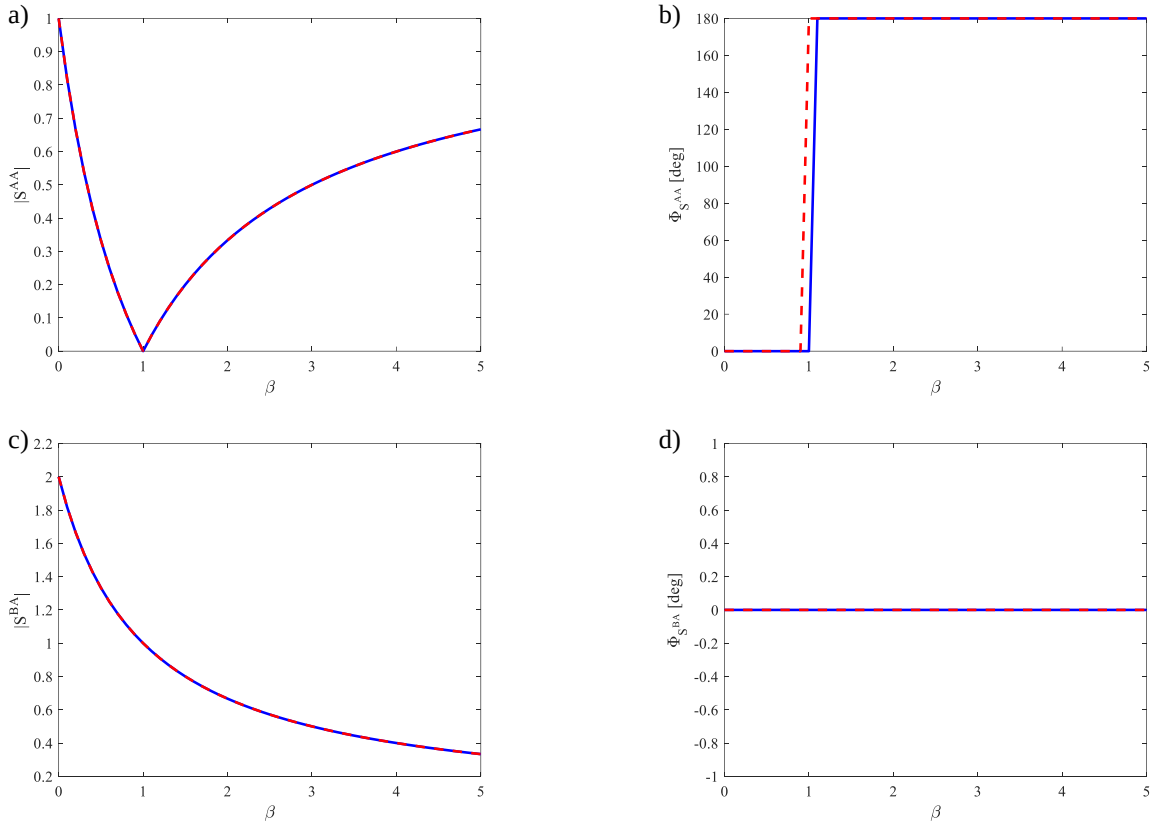

Source: Elaborated by the author

Since the solutions are obtained using the same equations but different formulations, they give the same results as expected.

3.3.3 Matrix Formulation for the Beam

Following the same procedure from the rod formulation, the displacement equations for a beam can be written as

$$w_{\mathrm{A}} = W^{+}_{\mathrm{P,A}} e^{-ik^{+}_{\mathrm{P,A}} x_0} + W^{+}_{\mathrm{N,A}} e^{-k^{+}_{\mathrm{N,A}} x_0} + W^{-}_{\mathrm{P,A}} e^{ik^{-}_{\mathrm{P,A}} x_0} + W^{-}_{\mathrm{N,A}} e^{k^{-}_{\mathrm{N,A}} x_0} \tag{189}$$

$$w_{\mathrm{B}} = W^{+}_{\mathrm{P,B}} e^{-ik^{+}_{\mathrm{P,B}} x_0} + W^{+}_{\mathrm{N,B}} e^{-k^{+}_{\mathrm{N,B}} x_0} + W^{-}_{\mathrm{P,B}} e^{ik^{-}_{\mathrm{P,B}} x_0} + W^{-}_{\mathrm{N,B}} e^{k^{-}_{\mathrm{N,B}} x_0} \tag{190}$$

$$\theta_{\mathrm{A}} = -ik^{+}_{\mathrm{P,A}} W^{+}_{\mathrm{P,A}} e^{-ik^{+}_{\mathrm{P,A}} x_0} - k^{+}_{\mathrm{N,A}} W^{+}_{\mathrm{N,A}} e^{-k^{+}_{\mathrm{N,A}} x_0} + ik^{-}_{\mathrm{P,A}} W^{-}_{\mathrm{P,A}} e^{ik^{-}_{\mathrm{P,A}} x_0} + k^{-}_{\mathrm{N,A}} W^{-}_{\mathrm{N,A}} e^{k^{-}_{\mathrm{N,A}} x_0} \tag{191}$$

$$\theta_{\mathrm{B}} = -ik^{+}_{\mathrm{P,B}} W^{+}_{\mathrm{P,B}} e^{-ik^{+}_{\mathrm{P,B}} x_0} - k^{+}_{\mathrm{N,B}} W^{+}_{\mathrm{N,B}} e^{-k^{+}_{\mathrm{N,B}} x_0} + ik^{-}_{\mathrm{P,B}} W^{-}_{\mathrm{P,B}} e^{ik^{-}_{\mathrm{P,B}} x_0} + k^{-}_{\mathrm{N,B}} W^{-}_{\mathrm{N,B}} e^{k^{-}_{\mathrm{N,B}} x_0} \tag{192}$$

The shear forces and bending moments are given by

$$M_{\mathrm{A}} = E_{\mathrm{A}} I_{\mathrm{A}} \left(-k_{\mathrm{P,A}}^{+\,2} W_{\mathrm{P,A}}^{+} e^{-ik_{\mathrm{P,A}}^{+} x_0} + k_{\mathrm{N,A}}^{+\,2} W_{\mathrm{N,A}}^{+} e^{-k_{\mathrm{N,A}}^{+} x_0} - k_{\mathrm{P,A}}^{-\,2} W_{\mathrm{P,A}}^{-} e^{ik_{\mathrm{P,A}}^{-} x_0} + k_{\mathrm{N,A}}^{-\,2} W_{\mathrm{N,A}}^{-} e^{k_{\mathrm{N,A}}^{-} x_0} \right) \quad (193)$$

$$M_{\mathrm{B}} = E_{\mathrm{B}} I_{\mathrm{B}} \left(-k_{\mathrm{P,B}}^{+\,2} W_{\mathrm{P,B}}^{+} e^{-ik_{\mathrm{P,B}}^{+} x_0} + k_{\mathrm{N,B}}^{+\,2} W_{\mathrm{N,B}}^{+} e^{-k_{\mathrm{N,B}}^{+} x_0} - k_{\mathrm{P,B}}^{-\,2} W_{\mathrm{P,B}}^{-} e^{ik_{\mathrm{P,B}}^{-} x_0} + k_{\mathrm{N,B}}^{-\,2} W_{\mathrm{N,B}}^{-} e^{k_{\mathrm{N,B}}^{-} x_0} \right) \quad (194)$$

$$V_{\mathrm{A}} = E_{\mathrm{A}} I_{\mathrm{A}} \left(ik_{\mathrm{P,A}}^{+\,3} W_{\mathrm{P,A}}^{+} e^{-ik_{\mathrm{P,A}}^{+} x_0} - k_{\mathrm{N,A}}^{+\,3} W_{\mathrm{N,A}}^{+} e^{-k_{\mathrm{N,A}}^{+} x_0} - ik_{\mathrm{P,A}}^{-\,3} W_{\mathrm{P,A}}^{-} e^{ik_{\mathrm{P,A}}^{-} x_0} + k_{\mathrm{N,A}}^{-\,3} W_{\mathrm{N,A}}^{-} e^{k_{\mathrm{N,A}}^{-} x_0} \right) \quad (195)$$

$$V_{\mathrm{B}} = E_{\mathrm{B}} I_{\mathrm{B}} \left(ik_{\mathrm{P,B}}^{+\,3} W_{\mathrm{P,B}}^{+} e^{-ik_{\mathrm{P,B}}^{+} x_0} - k_{\mathrm{N,B}}^{+\,3} W_{\mathrm{N,B}}^{+} e^{-k_{\mathrm{N,B}}^{+} x_0} - ik_{\mathrm{P,B}}^{-\,3} W_{\mathrm{P,B}}^{-} e^{ik_{\mathrm{P,B}}^{-} x_0} + k_{\mathrm{N,B}}^{-\,3} W_{\mathrm{N,B}}^{-} e^{k_{\mathrm{N,B}}^{-} x_0} \right) \quad (196)$$

Note that in this case the amplitudes *W* and wave numbers *k* are distinguished by the wavemode type (P for propagating and N for nearfield), waveguide (**A** or **B**) and direction of travel (+ or -). Now the displacement vectors are defined as

$$\mathbf{a}^{+} = \begin{Bmatrix} W_{\mathrm{P,A}}^{+} e^{-ik_{\mathrm{P,A}}^{+} x_0} \\ W_{\mathrm{N,A}}^{+} e^{-k_{\mathrm{N,A}}^{+} x_0} \end{Bmatrix},\ \mathbf{a}^{-} = \begin{Bmatrix} W_{\mathrm{P,A}}^{-} e^{ik_{\mathrm{P,A}}^{-} x_0} \\ W_{\mathrm{N,A}}^{-} e^{k_{\mathrm{N,A}}^{-} x_0} \end{Bmatrix},\ \mathbf{b}^{+} = \begin{Bmatrix} W_{\mathrm{P,B}}^{+} e^{-ik_{\mathrm{P,B}}^{+} x_0} \\ W_{\mathrm{N,B}}^{+} e^{-k_{\mathrm{N,B}}^{+} x_0} \end{Bmatrix} \text{ and } \mathbf{b}^{-} = \begin{Bmatrix} W_{\mathrm{P,B}}^{-} e^{ik_{\mathrm{P,B}}^{-} x_0} \\ W_{\mathrm{N,B}}^{-} e^{k_{\mathrm{N,B}}^{-} x_0} \end{Bmatrix} \quad (197)$$

grouping the displacements and forces as

$$\mathbf{q} = \begin{Bmatrix} w \\ \theta \end{Bmatrix} \text{ and } \mathbf{f} = \begin{Bmatrix} V \\ M \end{Bmatrix} \quad (198)$$

the equations of displacements and forces become

$$\mathbf{q}_{\mathrm{A}} = \begin{bmatrix} 1 & 1 \\ -ik_{\mathrm{P,A}}^{+} & -k_{\mathrm{N,A}}^{+} \end{bmatrix} \mathbf{a}^{+} + \begin{bmatrix} 1 & 1 \\ ik_{\mathrm{P,A}}^{-} & k_{\mathrm{N,A}}^{-} \end{bmatrix} \mathbf{a}^{-} \quad (199)$$

$$\mathbf{f}_{\mathrm{A}} = \begin{bmatrix} iEIk_{\mathrm{P,A}}^{+\,3} & -EIk_{\mathrm{N,A}}^{+\,3} \\ -EIk_{\mathrm{P,A}}^{+\,2} & EIk_{\mathrm{N,A}}^{+\,2} \end{bmatrix} \mathbf{a}^{+} + \begin{bmatrix} -iEIk_{\mathrm{P,A}}^{-\,3} & EIk_{\mathrm{N,A}}^{-\,3} \\ -EIk_{\mathrm{P,A}}^{-\,2} & EIk_{\mathrm{N,A}}^{-\,2} \end{bmatrix} \mathbf{a}^{-} \quad (200)$$

$$\mathbf{q}_{\mathrm{B}} = \begin{bmatrix} 1 & 1 \\ -ik_{\mathrm{P,B}}^{+} & -k_{\mathrm{N,B}}^{+} \end{bmatrix} \mathbf{b}^{+} + \begin{bmatrix} 1 & 1 \\ ik_{\mathrm{P,B}}^{-} & k_{\mathrm{N,B}}^{-} \end{bmatrix} \mathbf{b}^{-} \quad (201)$$

$$\mathbf{f}_{\mathrm{B}} = \begin{bmatrix} iEIk_{\mathrm{P,B}}^{+\,3} & -EIk_{\mathrm{N,B}}^{+\,3} \\ -EIk_{\mathrm{P,B}}^{+\,2} & EIk_{\mathrm{N,B}}^{+\,2} \end{bmatrix} \mathbf{b}^{+} + \begin{bmatrix} -iEIk_{\mathrm{P,B}}^{-\,3} & EIk_{\mathrm{N,B}}^{-\,3} \\ -EIk_{\mathrm{P,B}}^{-\,2} & EIk_{\mathrm{N,B}}^{-\,2} \end{bmatrix} \mathbf{b}^{-} \quad (202)$$

With this, the wave mode matrices $\mathbf{\Phi}$ can be found by comparing Eq. (199) with Eq. (26) and so on.

$$\begin{aligned}
\mathbf{\Phi}^{+}_{\mathrm{q,A}} &= \begin{bmatrix} 1 & 1 \\ -ik^{+}_{\mathrm{P,A}} & -k^{+}_{\mathrm{N,A}} \end{bmatrix}, \ \mathbf{\Phi}^{-}_{\mathrm{q,A}} = \begin{bmatrix} 1 & 1 \\ ik^{-}_{\mathrm{P,A}} & k^{-}_{\mathrm{N,A}} \end{bmatrix}, \\
\mathbf{\Phi}^{+}_{\mathrm{q,B}} &= \begin{bmatrix} 1 & 1 \\ -ik^{+}_{\mathrm{P,B}} & -k^{+}_{\mathrm{N,B}} \end{bmatrix}, \ \mathbf{\Phi}^{-}_{\mathrm{q,B}} = \begin{bmatrix} 1 & 1 \\ ik^{-}_{\mathrm{P,B}} & k^{-}_{\mathrm{N,B}} \end{bmatrix}
\end{aligned} \tag{203}$$

$$\begin{aligned}
\mathbf{\Phi}^{+}_{\mathrm{f,A}} &= \begin{bmatrix} iEIk^{+\,3}_{\mathrm{P,A}} & -EIk^{+\,3}_{\mathrm{N,A}} \\ -EIk^{+\,2}_{\mathrm{P,A}} & EIk^{+\,2}_{\mathrm{N,A}} \end{bmatrix}, \ \mathbf{\Phi}^{-}_{\mathrm{f,A}} = \begin{bmatrix} -iEIk^{-\,3}_{\mathrm{P,A}} & EIk^{-\,3}_{\mathrm{N,A}} \\ -EIk^{-\,2}_{\mathrm{P,A}} & EIk^{-\,2}_{\mathrm{N,A}} \end{bmatrix} \\
\mathbf{\Phi}^{+}_{\mathrm{f,B}} &= \begin{bmatrix} iEIk^{+\,3}_{\mathrm{P,B}} & -EIk^{+\,3}_{\mathrm{N,B}} \\ -EIk^{+\,2}_{\mathrm{P,B}} & EIk^{+\,2}_{\mathrm{N,B}} \end{bmatrix}, \ \mathbf{\Phi}^{-}_{\mathrm{f,B}} = \begin{bmatrix} -iEIk^{-\,3}_{\mathrm{P,B}} & EIk^{-\,3}_{\mathrm{N,B}} \\ -EIk^{-\,2}_{\mathrm{P,B}} & EIk^{-\,2}_{\mathrm{N,B}} \end{bmatrix}
\end{aligned} \tag{204}$$

Again, by applying the boundary conditions, Eq. (28) can be applied to obtain the scattering matrix. Figure 22 shows the comparison of the results from both formulations for the bending propagating wavemode.

Figure 22 – Comparison of the reflection and transmission coefficients obtained with the wave matrix formulation for a beam. a) Absolute value of the reflection coefficient; b) Phase of the reflection coefficient; c) Absolute value of the transmission coefficient; d) Phase of the transmission coefficient. Blue continuous line —: Analytical solution; Red dashed line - - : wave matrix formulation solution.

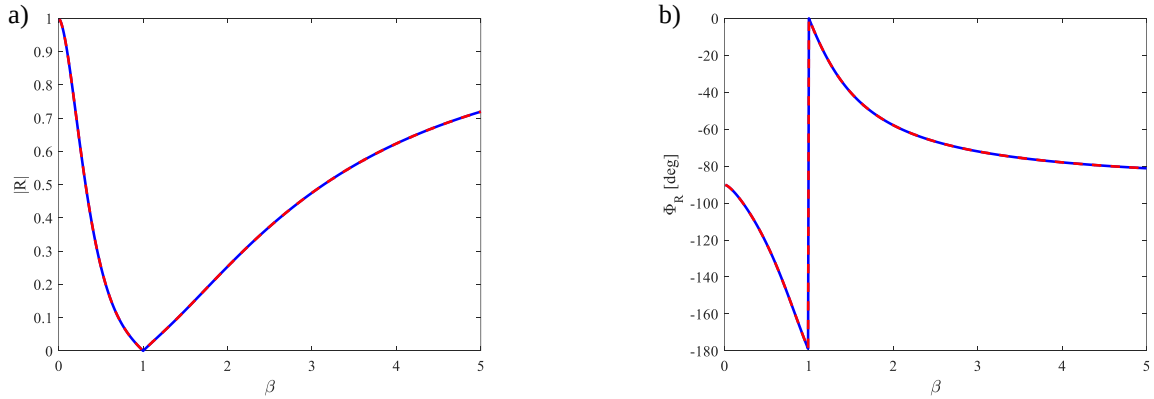

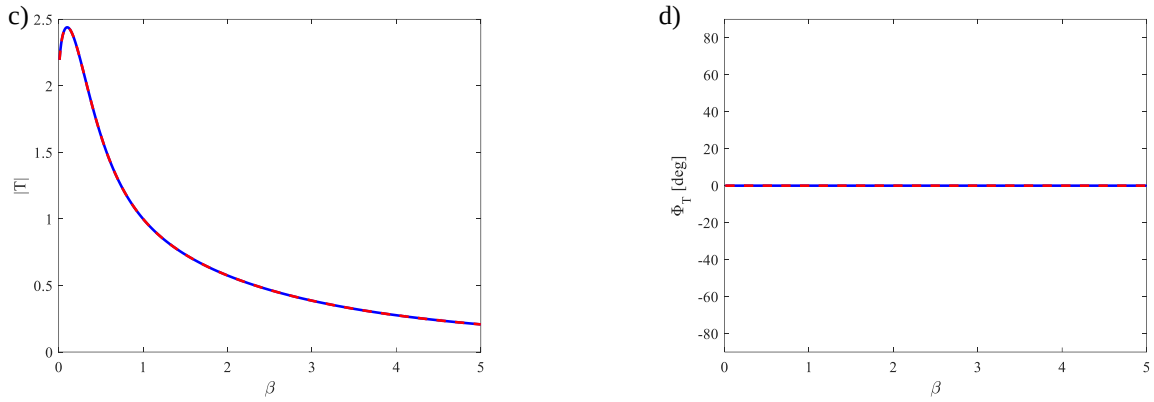

Source: Elaborated by the author

Again, it can be seen that results using both formulations are matching. Only the bending propagating reflected and transmitted results are shown.

3.4 REFLECTION AND TRANSMISSION IN WAVEGUIDES WITH TWO DISCONTINUITIES

3.4.1 Introduction

Here the problem of two discontinuities is studied. The generalized solution for two consecutive discontinuities shown on Section 2.3.1 is used. Using this, the solutions of two changes of cross-sectional areas in a rod and in a beam are shown.

Consider a waveguide laying on the *x*-axis with one area reduction in the first discontinuity and an area increase in discontinuity 2 as shown in Figure 23.

Figure 23 – Waveguide with two consecutive cross-sectional area changes.

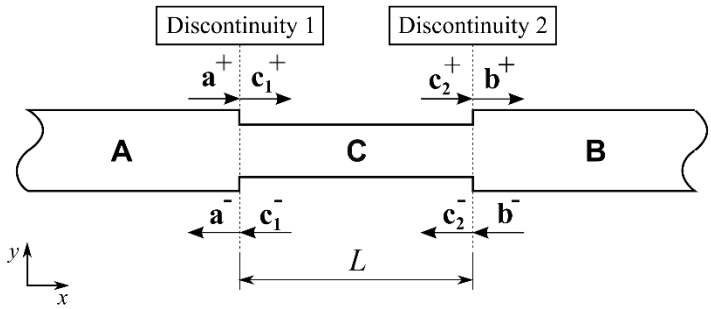

Source: Elaborated by the author

In this example both discontinuities are symmetric, that is the area reduction is centred around the *x*-axis and the reduction in discontinuity 1 is recovered in discontinuity 2.

As shown in Section 2.3.1, the scattering matrix for this case is given by

$$\begin{Bmatrix} \mathbf{a}^{-} \\ \mathbf{b}^{+} \end{Bmatrix} = \begin{bmatrix} \mathbf{S}^{AA} & \mathbf{S}^{AB} \\ \mathbf{S}^{BA} & \mathbf{S}^{BB} \end{bmatrix} \begin{Bmatrix} \mathbf{a}^{+} \\ \mathbf{b}^{-} \end{Bmatrix} \tag{205}$$

which can be written as a function of the individual scattering matrices of each discontinuity as

$$\begin{aligned} \mathbf{S}^{AB} &= \mathbf{S}_1^{AC}\mathbf{T}_C\left(\mathbf{I}-\mathbf{T}_C^{-1}\mathbf{S}_2^{CC}\mathbf{T}_C\mathbf{S}_1^{CC}\right)^{-1}\mathbf{S}_2^{CB} \\ \mathbf{S}^{AA} &= \mathbf{S}_1^{AA}+\mathbf{S}_1^{AC}\mathbf{T}_C\left(\mathbf{I}-\mathbf{T}_C^{-1}\mathbf{S}_2^{CC}\mathbf{T}_C\mathbf{S}_1^{CC}\right)^{-1}\mathbf{S}_2^{CC}\mathbf{T}_C\mathbf{S}_1^{CA} \\ \mathbf{S}^{BA} &= \mathbf{S}_2^{BC}\mathbf{T}_C^{-1}\left(\mathbf{I}-\mathbf{T}_C\mathbf{S}_1^{CC}\mathbf{T}_C^{-1}\mathbf{S}_2^{CC}\right)^{-1}\mathbf{S}_1^{CA} \\ \mathbf{S}^{BB} &= \mathbf{S}_2^{BB}+\mathbf{S}_2^{BC}\mathbf{T}_C^{-1}\left(\mathbf{I}-\mathbf{T}_C\mathbf{S}_1^{CC}\mathbf{T}_C^{-1}\mathbf{S}_2^{CC}\right)^{-1}\mathbf{S}_1^{CC}\mathbf{T}_C^{-1}\mathbf{S}_2^{CB} \end{aligned} \tag{206}$$

3.4.2 Scattering in a rod with two discontinuities

Since the coefficients at each discontinuity were already calculated in Section 3.1.4, the scattering coefficients for the case of two consecutive changes of cross-sectional area can be recovered from Eq. (43). To plot the results, different proportions of area change where calculated (0%, 10%, 30% and 50% of reduction in the cross-sectional area) and the coefficients were plotted as a function of both frequencies and L/λ, which is the ratio between the length of the damage and the wavelength λ. Figure 24 shows the displacement scattering coefficients.

Figure 24 – Reflection and transmission coefficients for the two area changes in a rod. a) Absolute value; b) Phase. Blue continuous line ——: 0% reduction; Red dashed line - - - -: 10% reduction; . Green dotted line ·····: 30% reduction; Cian dash-dot line – · – ·: 50% reduction.

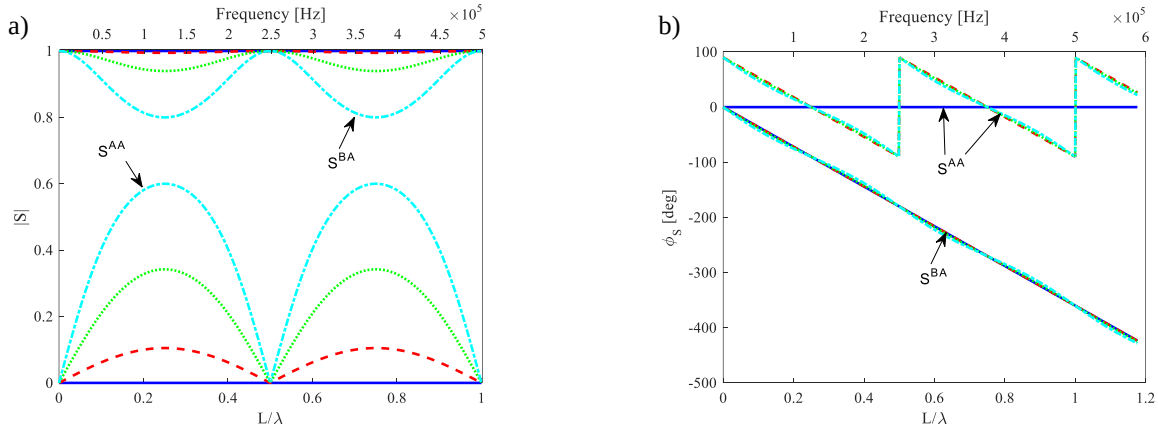

Source: Elaborated by the author

An interesting observation is that the reflection coefficient is much more sensitive to the variation of the section: while the transmission coefficient varies between 0.8 to 1.0, the

reflection varies from 0 to 0.6, which indicates that it should be easier to detect the variations of section by measuring the changes in the reflection coefficient.

The results are investigated considering the limiting case when the discontinuity length tends to zero. In this case, it is expected that the reflection coefficient tends to zero and the transmission coefficient tends to 1, which corresponds to the behaviour of a rod without discontinuity.

The limiting case when L tends to infinity is not studied since $\mathbf{S}^{BA}$ is calculated as the transmission of the wave arriving at discontinuity 1 and going out at 2.

It can be noted that the damaged section (waveguide **C**) behaves as a pass-band filter, and at some frequencies, there are no reflected waves. This result is supported by the results shown in Ayala Castillo, Lopes Junior and Brennan (2015).

As observed by Ayala Castillo, Lopes Junior and Brennan (2015) when $\frac{L}{\lambda}=\frac{n}{2}$ ($n=0,1,2...$) there is a maximum transmitted wave and minimum reflected. The cause of the predominance of transmission is due to the point in which the wave hits the discontinuity at discontinuity 2.

Figure 25 shows an explanation of this phenomenon using $\frac{L}{\lambda}=2$ as an example. Each step represents a time interval equivalent to 2 wavelengths travelled. The steps are described as follows:

I. the incident wave (blue line) arrives at interface 1;

II. at interface 1 the wave is reflected (red line) and transmitted (blue line). Since the wave travels from a bigger area to a smaller one, it reflects the wave as if it was a free end (no phase inversion) and the transmitted wave amplitude is slightly bigger than the incident wave. Since L is two times bigger than λ, the positive going wave at b arrives at interface 2 after exactly two wavelengths;

III. as the transmitted wave from 1 gets to 2, it also gets reflected (green line) and transmitted (blue line). In this case, the wave travels from a smaller area to a bigger one, which reflects the wave as if it was a fixed end (with a 180º phase shift). In this case, since the area reduction in 1 revert back to the original area in 2, the amplitude is also reverted back;

IV. because of the phase shift occurs at the interface 2, the reflected wave at 2 (green line) has a phase shift of 180º compared to the reflected wave at 1 (red line). When the second reflected wave arrives at interface 1, it gets transmitted with a

smaller amplitude, but since the area change from **B** to **C** is the inverse of **A** to **B**, the transmitted wave end up being of the same amplitude of the first reflected wave (red line), resulting in a destructive interference, so $\mathbf{S}^{AA}$.

Figure 25 – No reflection phenomenon. Blue line: Positive going waves (incident and transmitted); Red line: Wave reflected at interface 1; Green line: Wave reflected at interface 2 and eventually transmitted from b to a.

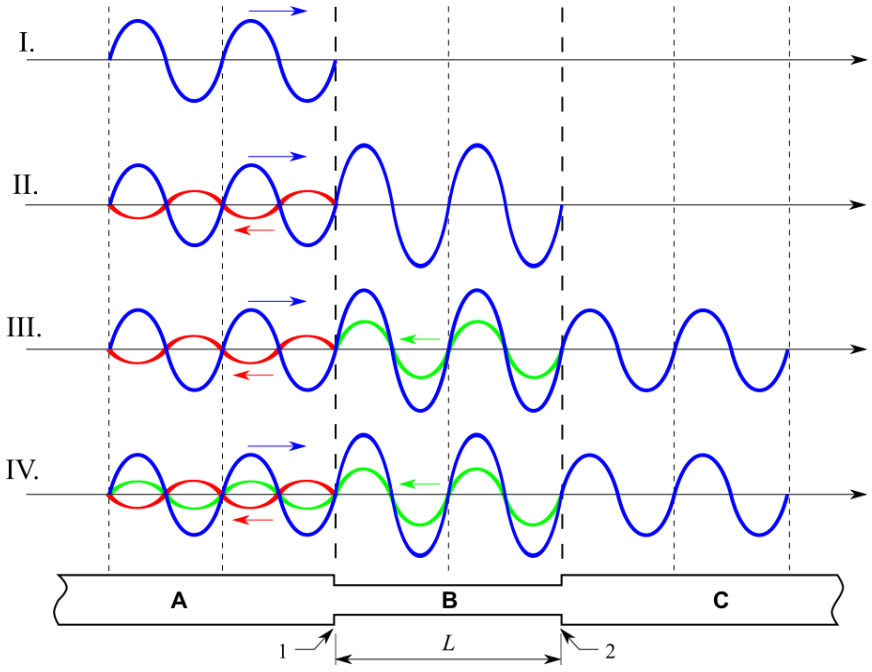

Source: Elaborated by the author

A similar process happens when $\frac{L}{\lambda} = \frac{2n-1}{4}$ In this case, the reflection shows a maximum and the transmission shows a minimum. The process is similar to the previous case, but this time the wave going to the positive direction in **B** arrives at discontinuity 2 at the peaks (or valleys) of the wave. This makes the reflected wave in green misalign from the reflected wave in red, creating a phase shift of 45º from each other, which in turn results in a constructive interference; therefore the total reflected wave $\mathbf{S}^{AA}$ reaches its maximum.

As for the transmitted wave $\mathbf{S}^{BA}$, the amplitude is smaller but it will only reach zero if the area of **C** tends to infinity when compared to the area of **B**. Since in this case there is no negative going wave in **C**, the only factor controlling $\mathbf{S}^{BA}$ is the transmission coefficient from **B** to **C**.

It is important to note that these two phenomena only happen because the area change in discontinuity 2 is the inverse of the area change in discontinuity 1, which means that the damage is symmetric both in the horizontal and the vertical axes. If this is not true, the reflection and transmission at each discontinuity would be completely different, thus the reflection only and transmission only phenomena probably would not occur in these cases and the maxima and minima would happen in different occasions.

3.4.3 Scattering in a beam with two discontinuities

In this section, the same case as in Figure 23 is studied for an Euler-Bernoulli beam. Figure 26 shows the bending propagating reflection coefficients and Figure 27 shows the bending propagating transmission coefficients. Here only the results for propagating incident wave are plotted.

Figure 26 – Bending propagating reflection coefficients for the two area changes in a beam. a) Absolute value; b) Phase. Blue continuous line ——: 0% reduction; Red dashed line - - - -: 10% reduction; . Green dotted line ·····: 30% reduction; Cian dash-dot line – · – ·: 50% reduction.

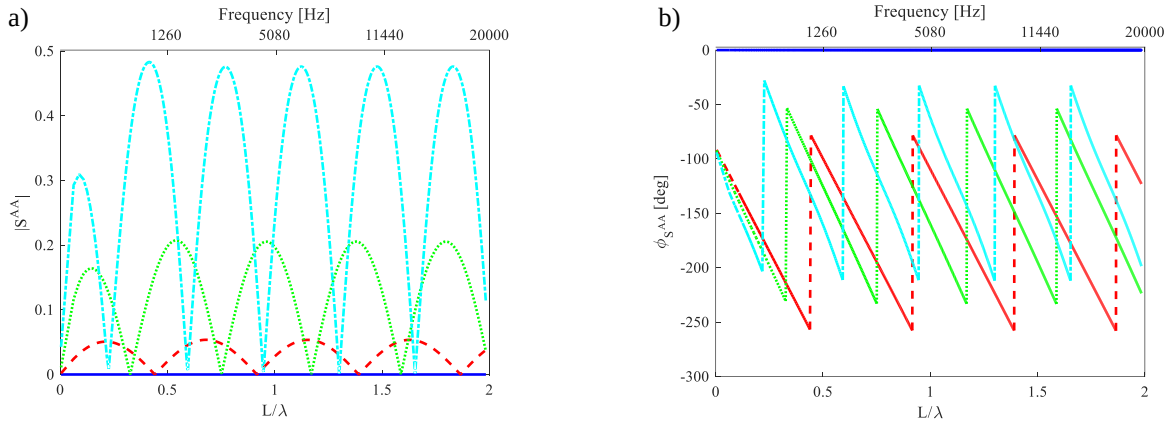

Source: Elaborated by the author

Figure 27 – Bending propagating transmission coefficients for the two area changes in a beam. a) Absolute value; b) Phase. Blue continuous line ——— : 0% reduction; Red dashed line - - - - : 10% reduction; . Green dotted line ····· : 30% reduction; Cian dash-dot line – · – · : 50% reduction.

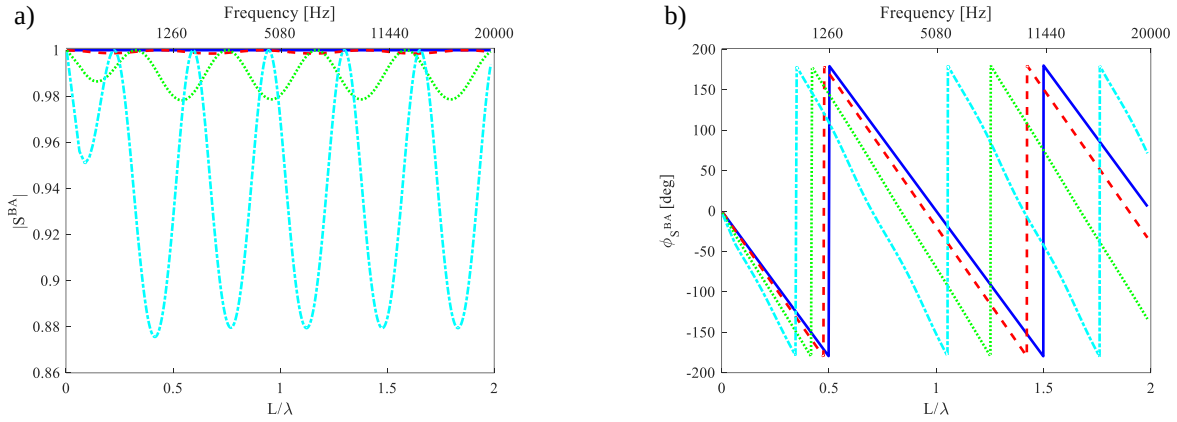

Source: Elaborated by the author

It can be seen that, compared to the previous case of a rod, the amplitudes of the first peak of the reflection coefficients are smaller than the following peaks. This may occur when the first peak occurs before $L = \lambda/4$ and similar behaviour is seen in the transmission coefficients. Since in the beam case the waves in **C** travels in a different speed from the incident wave, the oscillatory behaviour is formed not only by the L/λ ratio but also by the change in the phase velocity caused by the change of cross-sectional area generating a phase shift between the reflected and transmitted waves. This, in turn, causes the scattered waves to interact in a specific way, generating the oscillatory pattern seen in Figures 26 and 27. When this phase shift occurs at $L < \lambda/4$, the reflections and transmissions occur before the first wave reaches its first peak, therefore the reflected and transmitted amplitudes are smaller. The fact that at 10% reduction the difference in the peaks is small proves this since in this case, the first peak occurs slightly before $L = \lambda/4$. The same thing does not occur in the rod example since the oscillatory behaviour is generated by the L/λ ratio only, therefore the first peak always occurs at $L = \lambda/4$.

It is interesting to note that for the bending wave there are more points of maxima and minima, compared to the longitudinal case and when L is much smaller than λ the sensitivity of both coefficients seem to lower. This indicates that it should be slightly harder to detect section changes for bending waves, especially when the length of the discontinuity is very small.

Figures 28 and 29 show the nearfield scattering coefficients for a propagating incident wave.

Figure 28 – Bending nearfield reflection coefficients for the two area changes in a beam. a) Absolute value; b) Phase. Blue continuous line ——— : 0% reduction; Red dashed line - - - - : 10% reduction; . Green dotted line ····· : 30% reduction; Cian dash-dot line – · – · : 50% reduction.

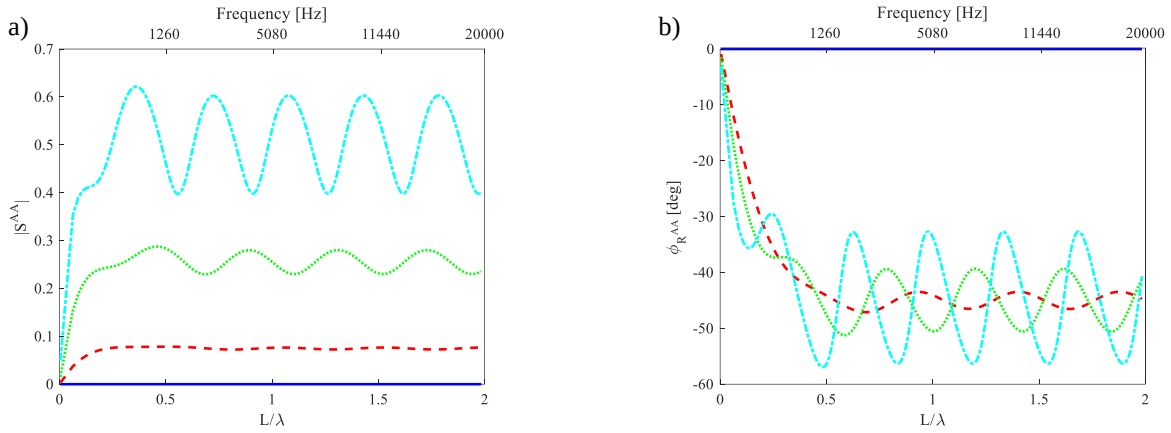

Source: Elaborated by the author

Figure 29 – Bending nearfield **T**ransmission coefficients for the two area changes in a beam. a) Absolute value; b) Phase. Blue continuous line ——— : 0% reduction; Red dashed line - - - - : 10% reduction; . Green dotted line ····· : 30% reduction; Cian dash-dot line – · – · : 50% reduction.

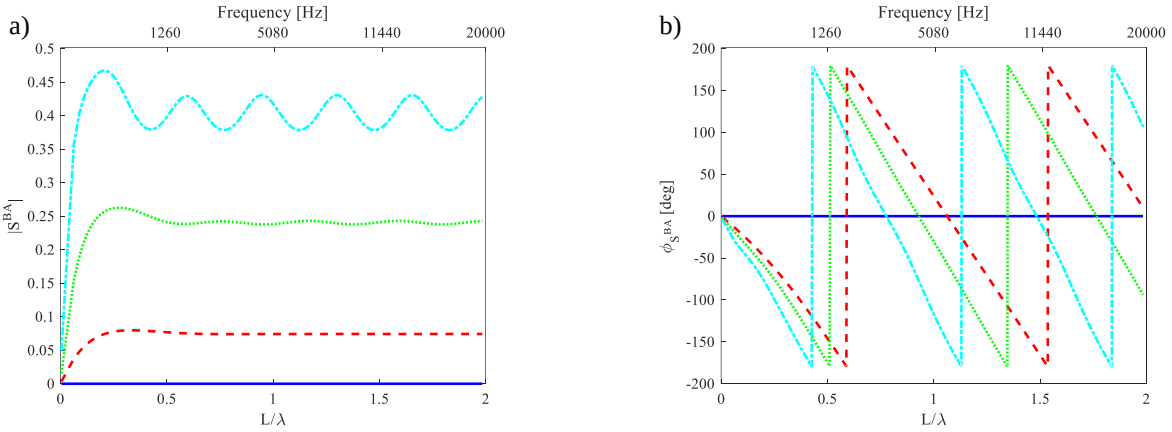

Source: Elaborated by the author

Here the first peaks are bigger than the other, as opposed to Figures 26 and 27. This is due to the fact that the nearfield waves have the biggest amplitude near the discontinuity. Because of this, if the waveguide **C** is very small, it means that the nearfield waves generated by the first discontinuity will immediately be scattered at the second discontinuity, maintaining its highest amplitude. As the value of L/λ gets bigger, the second discontinuity gets farther from the first, resulting in a smaller nearfield amplitude arriving at the second discontinuity. If the nearfield wave generated at the first discontinuity does not arrive at the second discontinuity, only the nearfield generated by the scattering propagating wave exist.

3.5 CONCLUSIONS

This chapter showed the analytical evaluation of the reflection and transmission coefficients for axial and flexural wave scattering from different boundary conditions and a change of the cross-sectional area. The results were validated considering limiting cases such as simple boundary conditions as free, fixed and no discontinuity (healthy waveguide), together with the results presented in the literature.

A wave matrix formulation was studied for the rod and beam cases as a general way to obtain the scattering matrix. Results considering a single discontinuity problem were discussed, then two consecutive changes of cross-sectional areas were studied. These were shown for both axial and flexural waves. It was shown that this kind of discontinuity behaves as pass-band and stop-band filters, depending on the frequency and the length of the discontinuity.

The steps to get the scattering matrix in a general case of a finite length change of the cross-sectional area were shown. These results can be used as a baseline to check numerical simulation results, these are shown in the next chapter, where the same scattering problems are studied using the WFE method.

4 SCATTERING IN BEAMS AND RODS - WFE SOLUTIONS

4.1 INTRODUCTION

In this chapter, the wave scattering in one-dimensional waveguides modelled as a rod and a beam is studied using the WFE method. The cases introduced in Chapter 3 using an analytical approach are obtained here numerically and the solutions are compared with those obtained previously. In particular, the WFE dynamic stiffness matrix is calculated and the WFE polynomial eigenvalue problem is solved in order to predict dispersion curves and wavemodes. Nodal displacements and nodal forces are here reformulated using the WFE wavemodes as a finite basis. These are then used to formulate equilibrium conditions and continuity of displacements at the discontinuities in order to obtain the scattering matrix as shown in Chapter 2. Comparison with the analytical solutions and solutions found in the literature is provided. Numerical issues related to the application of the method are also discussed.

The chapter is organized following the contents shown in Chapter 3 but using the WFE results to describe the displacement, nodal forces and boundary conditions.

4.2 WAVE SCATTERING IN RODS USING WFE ANALYSIS

4.2.1 Dispersion curves for a rod

In this section, the WFE analysis is applied to a rod. For simple cases as the rod, the FE mass and stiffness matrices can be easily obtained, e.g. Benmeddour *et al.* (2008). In this example, the FE mass and stiffness matrices are given by

$$\mathbf{M} = \frac{\rho SL}{6}\begin{bmatrix} 2 & 1 \\ 1 & 2 \end{bmatrix} \text{ and } \mathbf{K} = \frac{ES}{L}\begin{bmatrix} 1 & -1 \\ -1 & 1 \end{bmatrix} \tag{207}$$

Here the length L is the arbitrary length of a segment of the rod in the direction of wave propagation. Being a continuous structure, this can be considered as a periodic structure whose period is of length L. However, as indicated in Manconi (2008) and Waki, Mace and Brennan (2009b), if the length of the element is too big when compared to the wavelength in the frequency range of interest, the WFE results are not accurate. As a rule of thumb, L must be at least $1/6$ of the shortest wavelength. On the other hand, very small elements may incur in round-off errors as described in Waki, Mace and Brennan (2009b).

For the numerical calculation of **M** and **K**, the parameters in **Table** 3 are used. The dispersion curves are plotted both using analytical and WFE solutions. For the analytical solution, Eq. (208) was used (GRAFF, 1975).

$$k = \omega\sqrt{\frac{\rho}{E}} \tag{208}$$

Figure 30 shows the comparison between the analytical results and WFE results. For the rod element, only two real curves are obtained. These correspond to longitudinal modes propagating in the positive and negative direction respectively.

Figure 30 – Dispersion curves of a rod. Solid blue line —: Analytical solution; Dashed red line - - : WFE solution.

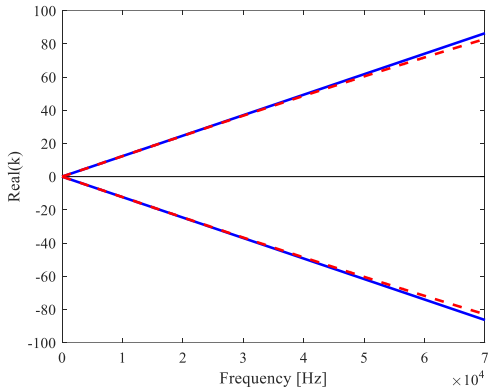

Source: Elaborated by the author

It can be seen that at the chosen frequency range, good agreement of the results can be found; differences at high frequency can be reduced by choosing a smaller *L* of the FE element.

4.2.2 Wave scattering in a rod with a linear spring fixed at its end

Consider the example of a rod fixed by a spring at its end as in Figure 5, Chapter 3. For this case, the equilibrium equation written in matrix notation is

$$\mathbf{f}_{\mathrm{A}} = s_1\mathbf{q}_{\mathrm{A}} \tag{209}$$

which can be written as a function of the wave amplitudes

$$E_{\mathrm{A}}S_{\mathrm{A}}k_{\mathrm{A}}\left[-i\mathbf{a}^{+} + i\mathbf{a}^{-}\right] + s_1\left[\mathbf{a}^{+} + \mathbf{a}^{-}\right] = \mathbf{0} \tag{210}$$

Since in this case, only one waveguide is present, the subscript indication is omitted, for reference see Section 3.4.2. The equation can be rewritten as

$$\frac{1}{ESk}\left(-iESk\mathbf{a}^{+}+iESk\mathbf{a}^{-}\right)=\alpha\left(\mathbf{a}^{+}+\mathbf{a}^{-}\right) \tag{211}$$

where $\alpha=\frac{s_1}{ESk}$ is the non-dimensional stiffness ratio

Equation (211) can be correlated to the equilibrium equations written as functions of the nodal displacement and nodal forces. The nodal displacement and nodal forces are approximated by a linear combination of wavemodes according to Eq. (26) as

$$\mathbf{D}_{\mathrm{A}}\left(-\mathbf{\Phi}_{\mathrm{f}}^{+}\mathbf{a}^{+}+\mathbf{\Phi}_{\mathrm{f}}^{-}\mathbf{a}^{-}\right)=\mathbf{D}_{\mathrm{A}}\left(\mathbf{\Phi}_{\mathrm{q}}^{+}\mathbf{a}^{+}+\mathbf{\Phi}_{\mathrm{q}}^{-}\mathbf{a}^{-}\right) \tag{212}$$

Using the notation from Eq. (27), the boundary condition matrices $\mathbf{D}_{\mathrm{A}}$ and $\mathbf{D}_{\mathrm{B}}$, and the nodal displacements and nodal forces can be found by comparing Eq. (211) with Eq. (212), giving

$$\mathbf{D}_{\mathrm{A}}=\frac{1}{ESk};\quad \mathbf{D}_{\mathrm{B}}=\alpha;\ \mathbf{\Phi}_{\mathrm{f}}^{+}=-1;\ \mathbf{\Phi}_{\mathrm{f}}^{-}=1;\ \mathbf{\Phi}_{\mathrm{q}}^{+}=1;\ \mathbf{\Phi}_{\mathrm{q}}^{-}=1 \tag{213}$$

and for this particular case, they are scalars.

Figure 31 shows the comparison between the WFE solution obtained by solving Eq. (30) and the analytical solution as in Chapter 2.

Figure 31 – Reflection of axial waves in a rod with a spring at its end. a) absolute value; b) phase. Solid blue line —: Analytical solution; dashed red line - - : WFE solution.

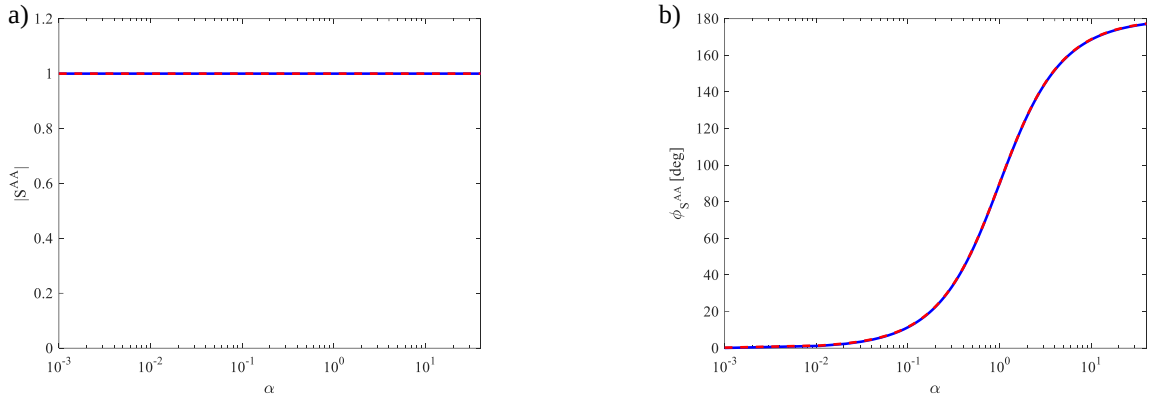

Source: Elaborated by the author

As it can be seen the results are in agreement. For this case, this agreement was expected due to the simple formulation for the rod.

4.2.3 Wave scattering in two semi-infinite rods connected by a spring

Consider again the example of two rods connected by a spring, see Figure 7 in Chapter 3. The equilibrium equations are

$$\begin{aligned}\mathbf{f}_{\mathsf{A}} &= s_1\left(\mathbf{q}_{\mathsf{A}} - \mathbf{q}_{\mathsf{B}}\right)\\ \mathbf{f}_{\mathsf{B}} &= s_1\left(\mathbf{q}_{\mathsf{A}} - \mathbf{q}_{\mathsf{B}}\right)\end{aligned} \tag{214}$$

In this case, since both waveguides **A** and **B** have the same properties, the subscripts indicating the waveguide are again omitted. Eq. (214) is written as functions of the wave amplitudes and the non-dimensional stiffness as

$$\begin{aligned}\frac{1}{ESk}\left(-iESk\mathbf{a}^{+} + iESk\mathbf{a}^{-}\right) &= \alpha\left(\mathbf{a}^{+} + \mathbf{a}^{-} - \mathbf{b}^{+} - \mathbf{b}^{-}\right)\\ \frac{1}{ESk}\left(-iESk\mathbf{b}^{+} + iESk\mathbf{b}^{-}\right) &= \alpha\left(\mathbf{a}^{+} + \mathbf{a}^{-} - \mathbf{b}^{+} - \mathbf{b}^{-}\right)\end{aligned} \tag{215}$$

Following the same procedure as in the previous section, the equations can be given as functions of the nodal displacements, nodal forces and boundary condition matrices

$$\begin{aligned}\mathbf{D}_{\mathrm{A}}\left(\boldsymbol{\Phi}^{+}_{\mathrm{f,a}}\mathbf{a}^{+} + \boldsymbol{\Phi}^{-}_{\mathrm{f,a}}\mathbf{a}^{-}\right) &= \mathbf{D}_{\mathrm{B}}\left(\boldsymbol{\Phi}^{+}_{\mathrm{q,a}}\mathbf{a}^{+} + \boldsymbol{\Phi}^{-}_{\mathrm{q,a}}\mathbf{a}^{-} - \boldsymbol{\Phi}^{+}_{\mathrm{q,b}}\mathbf{b}^{+} - \boldsymbol{\Phi}^{-}_{\mathrm{q,b}}\mathbf{b}^{-}\right)\\ \mathbf{D}_{\mathrm{A}}\left(\boldsymbol{\Phi}^{+}_{\mathrm{f,b}}\mathbf{b}^{+} + \boldsymbol{\Phi}^{-}_{\mathrm{f,b}}\mathbf{b}^{-}\right) &= \mathbf{D}_{\mathrm{B}}\left(\boldsymbol{\Phi}^{+}_{\mathrm{q,a}}\mathbf{a}^{+} + \boldsymbol{\Phi}^{-}_{\mathrm{q,a}}\mathbf{a}^{-} - \boldsymbol{\Phi}^{+}_{\mathrm{q,b}}\mathbf{b}^{+} - \boldsymbol{\Phi}^{-}_{\mathrm{q,b}}\mathbf{b}^{-}\right)\end{aligned} \tag{216}$$

and by correlating with Eq. (215)

$$\begin{aligned}
&\mathbf{D}_{\mathrm{A}} = \frac{1}{ESk} \text{ and } \mathbf{D}_{\mathrm{B}} = \alpha \\
&\mathbf{\Phi}^{+}_{\mathrm{q,a}} = 1;\ \mathbf{\Phi}^{-}_{\mathrm{q,a}} = 1;\ \mathbf{\Phi}^{+}_{\mathrm{f,a}} = -iESk;\ \mathbf{\Phi}^{-}_{\mathrm{f,a}} = iESk \\
&\mathbf{\Phi}^{+}_{\mathrm{q,b}} = 1;\ \mathbf{\Phi}^{-}_{\mathrm{q,b}} = 1;\ \mathbf{\Phi}^{+}_{\mathrm{f,b}} = -iESk;\ \mathbf{\Phi}^{-}_{\mathrm{f,b}} = iESk
\end{aligned} \tag{217}$$

In order to calculate the scattering matrix, Eq. (216) is organized according to Eq. (28), that is

$$\begin{aligned}
&\begin{bmatrix} \mathbf{D}_{\mathrm{A}}\mathbf{\Phi}^{-}_{\mathrm{f,a}} - \mathbf{D}_{\mathrm{B}}\mathbf{\Phi}^{-}_{\mathrm{q,a}} & \mathbf{D}_{\mathrm{B}}\mathbf{\Phi}^{+}_{\mathrm{q,b}} \\ -\mathbf{D}_{\mathrm{A}}\mathbf{\Phi}^{-}_{\mathrm{q,a}} & \mathbf{D}_{\mathrm{A}}\mathbf{\Phi}^{+}_{\mathrm{f,b}} + \mathbf{D}_{\mathrm{B}}\mathbf{\Phi}^{+}_{\mathrm{q,b}} \end{bmatrix} \begin{Bmatrix} \mathbf{a}^{-} \\ \mathbf{b}^{+} \end{Bmatrix} = \\
&\begin{bmatrix} -\mathbf{D}_{\mathrm{A}}\mathbf{\Phi}^{+}_{\mathrm{f,a}} + \mathbf{D}_{\mathrm{B}}\mathbf{\Phi}^{+}_{\mathrm{q,a}} & -\mathbf{D}_{\mathrm{B}}\mathbf{\Phi}^{-}_{\mathrm{q,b}} \\ \mathbf{D}_{\mathrm{B}}\mathbf{\Phi}^{-}_{\mathrm{q,a}} & -\mathbf{D}_{\mathrm{A}}\mathbf{\Phi}^{-}_{\mathrm{f,b}} - \mathbf{D}_{\mathrm{B}}\mathbf{\Phi}^{-}_{\mathrm{q,b}} \end{bmatrix} \begin{Bmatrix} \mathbf{a}^{+} \\ \mathbf{b}^{-} \end{Bmatrix}
\end{aligned} \tag{218}$$

Since in this case, the two rods are identical, $\mathbf{\Phi}_{\mathrm{f,b}} = \mathbf{\Phi}_{\mathrm{f,a}}$ and $\mathbf{\Phi}_{\mathrm{q,b}} = \mathbf{\Phi}_{\mathrm{q,a}}$.

Figure 32 shows the comparison between the WFE and the analytical results of the reflection coefficient for the two semi-infinite rods connected by a spring.

Figure 32 – Reflection of axial waves in two semi-infinite-rods connected by a spring. a) absolute value; b) phase. Solid blue line —: Analytical solution; dashed red line - - : WFE solution.

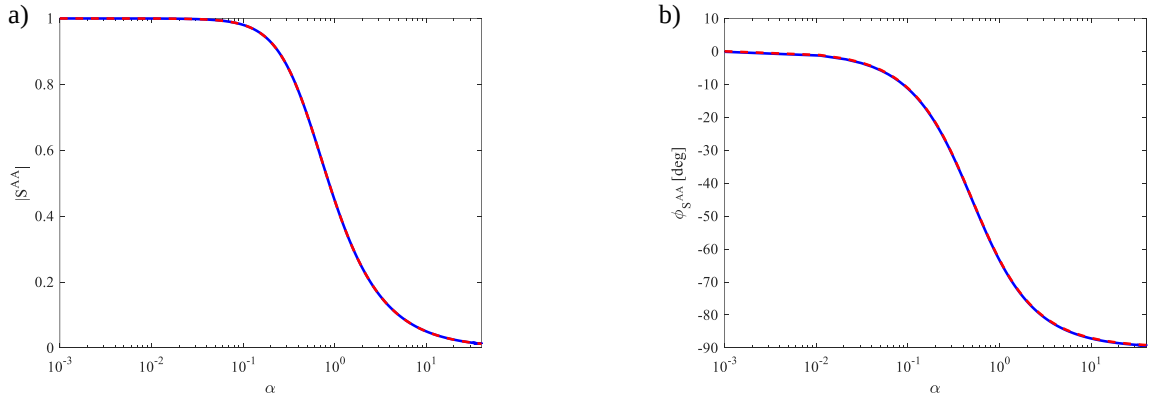

Source: Elaborated by the author

The results of the transmission coefficient are shown in Figure 33.

Figure 33 – Transmission of axial waves in two semi-infinite rods connected by a spring. a) absolute value; b) phase. Solid blue line —: Analytical solution; dashed red line - - : WFE solution.

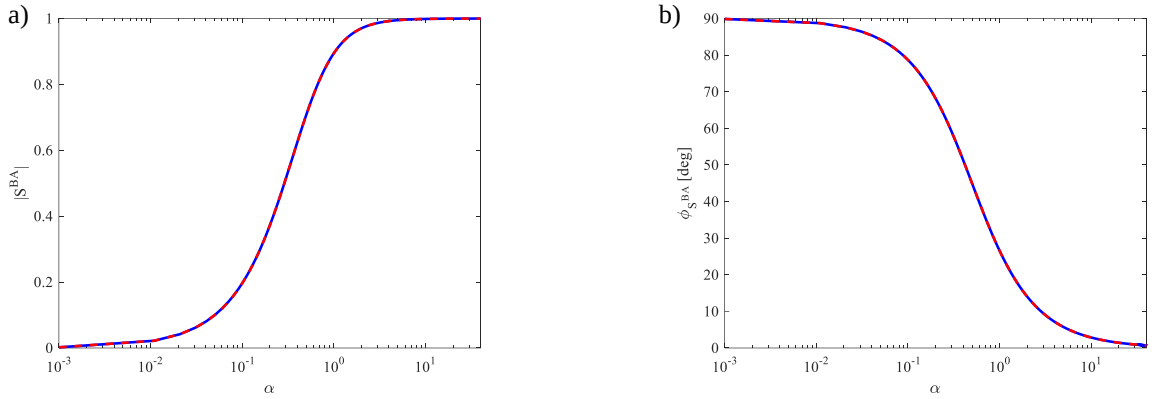

Source: Elaborated by the author

As shown in the previous case, the results are in perfect agreement.

4.2.4 Wave scattering in a rod with a change of cross-sectional area

Consider two rods with different cross-sectional areas as shown in Chapter 3, Figure 10. The equilibrium equations at the discontinuity are

$$\begin{aligned} \mathbf{q}_\mathrm{A} &= \mathbf{q}_\mathrm{B} \\ \mathbf{f}_\mathrm{A} &= \mathbf{f}_\mathrm{B} \end{aligned} \tag{219}$$

and therefore

$$\begin{aligned} &\mathbf{a}^+ + \mathbf{a}^- = \mathbf{b}^+ + \mathbf{b}^- \\ &-iE_\mathrm{A}S_\mathrm{A}k_\mathrm{A}\mathbf{a}^+ + iE_\mathrm{A}S_\mathrm{A}k_\mathrm{A}\mathbf{a}^- = -iE_\mathrm{B}S_\mathrm{B}k_\mathrm{B}\mathbf{b}^+ + iE_\mathrm{B}S_\mathrm{B}k_\mathrm{B}\mathbf{b}^- \end{aligned} \tag{220}$$

in a matrix form, the equilibrium of forces and continuity equations can be written as

$$\begin{aligned} &\mathbf{C}_\mathrm{A}\left(\boldsymbol{\Phi}^+_{\mathrm{q,a}}\mathbf{a}^+ + \boldsymbol{\Phi}^-_{\mathrm{q,a}}\mathbf{a}^-\right) = \mathbf{C}_\mathrm{B}\left(\boldsymbol{\Phi}^+_{\mathrm{q,b}}\mathbf{b}^+ + \boldsymbol{\Phi}^-_{\mathrm{q,b}}\mathbf{b}^-\right) \\ &\mathbf{D}_\mathrm{A}\left(\boldsymbol{\Phi}^+_{\mathrm{f,a}}\mathbf{a}^+ + \boldsymbol{\Phi}^-_{\mathrm{f,a}}\mathbf{a}^-\right) = \mathbf{D}_\mathrm{B}\left(\boldsymbol{\Phi}^+_{\mathrm{f,b}}\mathbf{b}^+ + \boldsymbol{\Phi}^-_{\mathrm{f,b}}\mathbf{b}^-\right) \end{aligned} \tag{221}$$

which gives the boundary conditions, nodal displacements and nodal forces as

$$\begin{aligned}
&\mathbf{C}_{\mathrm{A}} = 1 \text{ and } \mathbf{C}_{\mathrm{B}} = 1 \\
&\mathbf{D}_{\mathrm{A}} = 1 \text{ and } \mathbf{D}_{\mathrm{B}} = 1 \\
&\boldsymbol{\Phi}^{+}_{\mathrm{q,a}} = 1;\ \boldsymbol{\Phi}^{-}_{\mathrm{q,a}} = 1;\ \boldsymbol{\Phi}^{+}_{\mathrm{f,a}} = -iE_{\mathrm{A}}S_{\mathrm{A}}k_{\mathrm{A}};\ \boldsymbol{\Phi}^{-}_{\mathrm{f,a}} = iE_{\mathrm{A}}S_{\mathrm{A}}k_{\mathrm{A}} \\
&\boldsymbol{\Phi}^{+}_{\mathrm{q,b}} = 1;\ \boldsymbol{\Phi}^{-}_{\mathrm{q,b}} = 1;\ \boldsymbol{\Phi}^{+}_{\mathrm{f,b}} = -iE_{\mathrm{B}}S_{\mathrm{B}}k_{\mathrm{B}};\ \boldsymbol{\Phi}^{-}_{\mathrm{f,b}} = iE_{\mathrm{B}}S_{\mathrm{B}}k_{\mathrm{B}}
\end{aligned} \tag{222}$$

here because of the number of degrees of freedom, these are also scalars.

The scattering matrix as in Eq. (30) can be calculated easily in this case and it is

$$\mathbf{S} = \begin{bmatrix} \mathbf{C}_{\mathrm{A}}\boldsymbol{\Phi}^{-}_{\mathrm{q,a}} & -\mathbf{C}_{\mathrm{B}}\boldsymbol{\Phi}^{+}_{\mathrm{q,b}} \\ \mathbf{D}_{\mathrm{A}}\boldsymbol{\Phi}^{-}_{\mathrm{f,a}} & -\mathbf{D}_{\mathrm{B}}\boldsymbol{\Phi}^{+}_{\mathrm{f,b}} \end{bmatrix}^{-1} \begin{bmatrix} -\mathbf{C}_{\mathrm{A}}\boldsymbol{\Phi}^{+}_{\mathrm{q,a}} & \mathbf{C}_{\mathrm{B}}\boldsymbol{\Phi}^{-}_{\mathrm{q,b}} \\ -\mathbf{D}_{\mathrm{A}}\boldsymbol{\Phi}^{+}_{\mathrm{f,a}} & \mathbf{D}_{\mathrm{B}}\boldsymbol{\Phi}^{-}_{\mathrm{f,b}} \end{bmatrix} \tag{223}$$

Figures 34 and 35 show the comparison between the reflection and transmission coefficients calculated using the WFE and the analytical approach. It can be seen that the results correlate very well.

Figure 34 – Reflection of the axial wave at a change of cross-sectional area. a) absolute value; b) phase. Solid blue line —: Analytical solution; dashed red line - - : WFE solution.

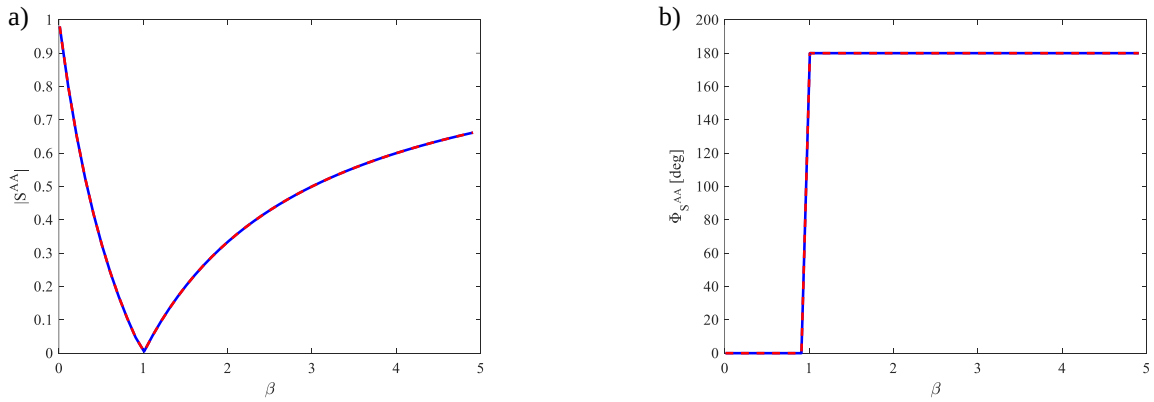

Source: Elaborated by the author

Figure 35 – Comparison of longitudinal wave transmission for a change of cross-sectional area. a) absolute value; b) phase. Solid blue line —: Analytical solution; dashed red line - - : WFE solution.

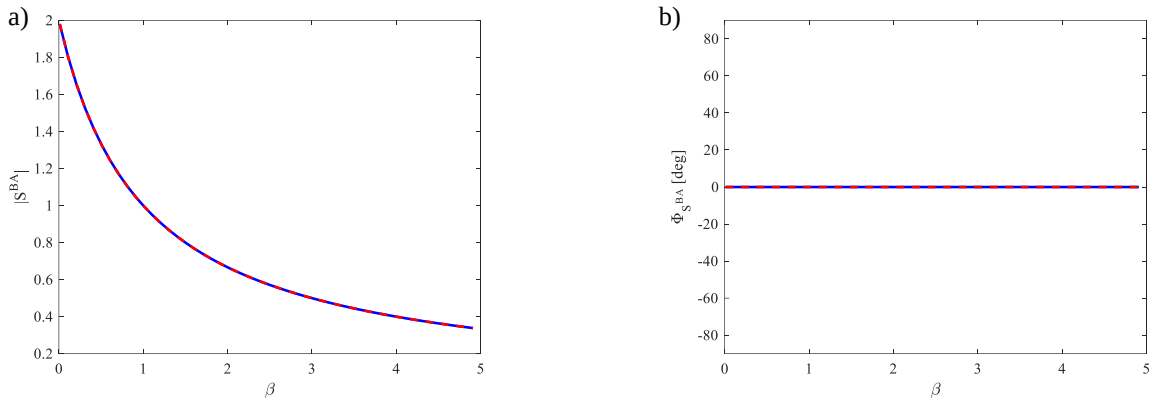

Source: Elaborated by the author

4.3 WAVE SCATTERING IN A BEAM USING WFE ANALYSIS

4.3.1 Dispersion curves for the beam

Consider the FE mass and stiffness matrices of an Euler-Bernoulli beam element of length L (BENMEDDOUR *et al.*, 2008).

$$\mathbf{M} = \frac{\rho SL}{420}\begin{bmatrix} 156 & 22L & 54 & -13L \\ 22L & 4L^2 & 13L & -3L^2 \\ 54 & 13L & 156 & -22L \\ -13L & -13L & -22L & 4L^2 \end{bmatrix} \text{ and } \mathbf{K} = \frac{EI}{L^3}\begin{bmatrix} 12 & 6L & -12 & 6L \\ 6L & 4L^2 & -6L & 2L^2 \\ -12 & -6L & 12 & -6L \\ 6L & 2L^2 & -6L & 4L^2 \end{bmatrix} \quad (224)$$

For the beam element, four wavemodes are considered: two bending modes propagating in the positive and negative directions, and two nearfield modes in the positive and negative direction. Dispersion curves are plotted in Figure 36 using the parameters in **Table** 3. For the analytical solution, Eq. (225) was used (GRAFF, 1975).

$$k = (\omega)^{\frac{1}{2}}\left(\frac{\rho S}{EI}\right)^{\frac{1}{4}} \quad (225)$$

Figure 36 – Dispersion curves of a beam. Solid blue line —: Analytical solution; Dashed red line --: WFE solution.

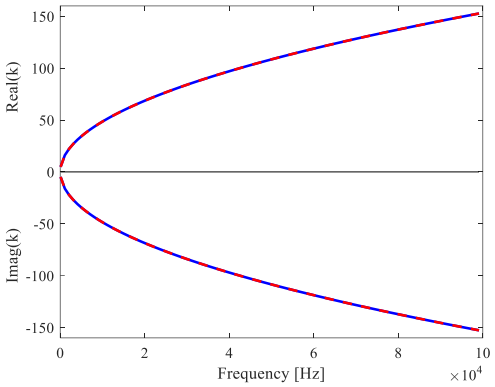

Source: Elaborated by the author

In this plot only the positive travelling waves are shown, that is those waves in which the wavenumbers are real positive and imaginary negative.

4.3.2 Wave scattering in a beam fixed by spring at its end

Consider now the example of a beam fixed by transverse and torsional springs at its end. The example is depicted in Figure 13, Chapter 3. The equilibrium of forces at the beam ends is

$$\mathbf{f}_{\mathrm{A}} = \begin{bmatrix} s_T & 0 \\ 0 & s_R \end{bmatrix} \mathbf{q}_{\mathrm{A}} \tag{226}$$

note that for the beam case the displacements and forces vectors are given by

$$\mathbf{q} = \begin{Bmatrix} w \\ \theta \end{Bmatrix} \text{ and } \mathbf{f} = \begin{Bmatrix} V \\ M \end{Bmatrix} \tag{227}$$

writing as a function of the wave amplitudes

$$\begin{Bmatrix} \begin{bmatrix} iEIk^3 & -EIk^3 \\ -EIk^2 & EIk^2 \end{bmatrix} \mathbf{a}^{+} + \begin{bmatrix} -iEIk^3 & EIk^3 \\ -EIk^2 & EIk^2 \end{bmatrix} \mathbf{a}^{-} \end{Bmatrix} = \begin{bmatrix} s_T & 0 \\ 0 & s_R \end{bmatrix} \begin{Bmatrix} \begin{bmatrix} 1 & 1 \\ -ik & -k \end{bmatrix} \mathbf{a}^{+} + \begin{bmatrix} 1 & 1 \\ ik & k \end{bmatrix} \mathbf{a}^{-} \end{Bmatrix} \tag{228}$$

which can be rewritten as

$$\begin{bmatrix} \dfrac{1}{EIk^3} & 0 \\ 0 & \dfrac{1}{EIk^2} \end{bmatrix} \left\{ \begin{bmatrix} iEIk^3 & -EIk^3 \\ -EIk^2 & EIk^2 \end{bmatrix} \mathbf{a}^+ + \begin{bmatrix} -iEIk^3 & EIk^3 \\ -EIk^2 & EIk^2 \end{bmatrix} \mathbf{a}^- \right\} = \\ \begin{bmatrix} \alpha_T & 0 \\ 0 & \alpha_R \end{bmatrix} \left\{ \begin{bmatrix} 1 & 1 \\ -ik & -k \end{bmatrix} \mathbf{a}^+ + \begin{bmatrix} 1 & 1 \\ ik & k \end{bmatrix} \mathbf{a}^- \right\} \tag{229}$$

Equation (229) can be rewritten as a function of the nodal displacements, nodal forces and boundary condition matrices, giving

$$\mathbf{D}_{\mathrm{A}} \left(\mathbf{\Phi}_{\mathrm{f}}^{+} \mathbf{a}^{+} + \mathbf{\Phi}_{\mathrm{f}}^{-} \mathbf{a}^{-} \right) = \mathbf{D}_{\mathrm{B}} \left(\mathbf{\Phi}_{\mathrm{q}}^{+} \mathbf{a}^{+} + \mathbf{\Phi}_{\mathrm{q}}^{-} \mathbf{a}^{-} \right) \tag{230}$$

where $\mathbf{D}_{\mathrm{A}}$ and $\mathbf{D}_{\mathrm{B}}$ are

$$\mathbf{D}_{\mathrm{A}} = \begin{bmatrix} \dfrac{1}{EIk^3} & 0 \\ 0 & \dfrac{1}{EIk^2} \end{bmatrix}; \quad \mathbf{D}_{\mathrm{B}} = \begin{bmatrix} \alpha_T & 0 \\ 0 & \alpha_R \end{bmatrix} \tag{231}$$

Figures 37 shows the comparison between the WFE and analytical solutions for the reflection coefficients and phase changes. As in Chapter 3, only the transverse spring was considered, therefore $\alpha = \alpha_T$. In this case, only the propagating flexural wave is assumed to impinge upon the spring. This is motivated by the fact that nearfiled waves are rapidly decaying. It can be seen that the WFE results match the analytical results.

Figure 37 – Reflection of flexural waves at spring discontinuity – only incident propagating wave. a) absolute value; b) phase. Solid blue line —: Analytical solution; Dashed red line - - : WFE solution.

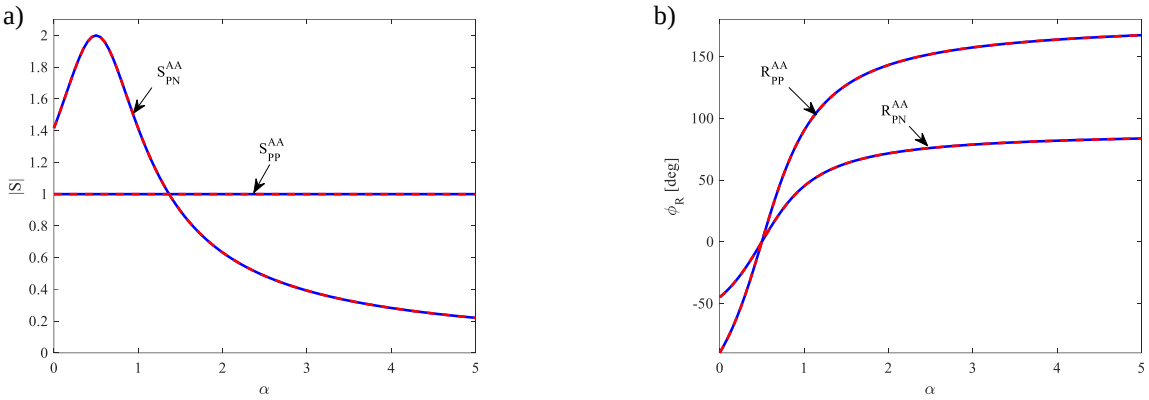

Source: Elaborated by the author

4.3.3 Wave scattering in an infinite beam fixed by a transverse spring

Consider Figure 15 where the beam fixed at a point by a transverse spring is considered. The equilibrium and continuity equations at the spring position in a matrix form are:

$$\begin{aligned}\mathbf{q}_{\mathrm{A}} &= \mathbf{q}_{\mathrm{B}} \\ \mathbf{f}_{\mathrm{A}} &= \begin{bmatrix} s_T & 0 \\ 0 & s_R \end{bmatrix}\mathbf{q}_{\mathrm{B}} + \mathbf{f}_{\mathrm{B}}\end{aligned} \tag{232}$$

Equation (232) can be re-written as functions of the wave amplitudes

$$\left(\begin{bmatrix} 1 & 1 \\ -i & -1 \end{bmatrix}\mathbf{a}^{+} + \begin{bmatrix} 1 & 1 \\ i & 1 \end{bmatrix}\mathbf{a}^{-}\right) = \left(\begin{bmatrix} 1 & 1 \\ -i & -1 \end{bmatrix}\mathbf{b}^{+} + \begin{bmatrix} 1 & 1 \\ i & 1 \end{bmatrix}\mathbf{b}^{-}\right) \tag{233}$$

$$\begin{aligned}&\left\{\begin{bmatrix} iEIk^3 & -EIk^3 \\ -EIk^2 & EIk^2 \end{bmatrix}\mathbf{a}^{+} + \begin{bmatrix} -iEIk^3 & EIk^3 \\ -EIk^2 & EIk^2 \end{bmatrix}\mathbf{a}^{-}\right\} = \\ &\begin{bmatrix} s_T & 0 \\ 0 & s_R \end{bmatrix}\begin{bmatrix} 1 & 1 \\ -i & -1 \end{bmatrix}\mathbf{b}^{+} + \left\{\begin{bmatrix} iEIk^3 & -EIk^3 \\ -EIk^2 & EIk^2 \end{bmatrix}\mathbf{b}^{+} + \begin{bmatrix} -iEIk^3 & EIk^3 \\ -EIk^2 & EIk^2 \end{bmatrix}\mathbf{b}^{-}\right\}\end{aligned} \tag{234}$$

The equations are reorganized according to Eqs. (176), Chapter 3, that is

$$\mathbf{I}\left(\begin{bmatrix} 1 & 1 \\ -i & -1 \end{bmatrix}\mathbf{a}^{+} + \begin{bmatrix} 1 & 1 \\ i & 1 \end{bmatrix}\mathbf{a}^{-}\right) = \mathbf{I}\left(\begin{bmatrix} 1 & 1 \\ -i & -1 \end{bmatrix}\mathbf{b}^{+} + \begin{bmatrix} 1 & 1 \\ i & 1 \end{bmatrix}\mathbf{b}^{-}\right) \tag{235}$$

$$\begin{bmatrix} \dfrac{1}{EIk^3} & 0 \\ 0 & \dfrac{1}{EIk^2} \end{bmatrix} \left\{ \begin{bmatrix} iEIk^3 & -EIk^3 \\ -EIk^2 & EIk^2 \end{bmatrix} \mathbf{a}^{+} + \begin{bmatrix} -iEIk^3 & EIk^3 \\ -EIk^2 & EIk^2 \end{bmatrix} \mathbf{a}^{-} \right\} =$$

$$\begin{bmatrix} \alpha_T & 0 \\ 0 & \alpha_R \end{bmatrix} \begin{bmatrix} 1 & 1 \\ -i & -1 \end{bmatrix} \mathbf{b}^{+} + \begin{bmatrix} \dfrac{1}{EIk^3} & 0 \\ 0 & \dfrac{1}{EIk^2} \end{bmatrix} \left\{ \begin{bmatrix} iEIk^3 & -EIk^3 \\ -EIk^2 & EIk^2 \end{bmatrix} \mathbf{b}^{+} + \begin{bmatrix} -iEIk^3 & EIk^3 \\ -EIk^2 & EIk^2 \end{bmatrix} \mathbf{b}^{-} \right\}$$

(236)

Equation (235) can be easily related to the continuity equation in Eq. (27) in Chapter 2, which can be written as

$$\mathbf{C}_{\mathrm{A}} \left(\mathbf{\Phi}^{+}_{\mathrm{q,a}} \mathbf{a}^{+} + \mathbf{\Phi}^{-}_{\mathrm{q,a}} \mathbf{a}^{-} \right) = \mathbf{C}_{\mathrm{B}} \left(\mathbf{\Phi}^{+}_{\mathrm{q,b}} \mathbf{b}^{+} + \mathbf{\Phi}^{-}_{\mathrm{q,b}} \mathbf{b}^{-} \right) \tag{237}$$

while the equilibrium of forces is

$$\mathbf{D}_{\mathrm{A}} \left(\mathbf{\Phi}^{+}_{\mathrm{f,a}} \mathbf{a}^{+} + \mathbf{\Phi}^{+}_{\mathrm{f,a}} \mathbf{a}^{-} \right) = \mathbf{C}_{\mathrm{B2}} \mathbf{\Phi}^{+}_{\mathrm{q,b}} \mathbf{b}^{+} + \mathbf{D}_{\mathrm{B}} \left(\mathbf{\Phi}^{+}_{\mathrm{f,b}} \mathbf{b}^{+} + \mathbf{\Phi}^{-}_{\mathrm{f,b}} \mathbf{b}^{-} \right) \tag{238}$$

where

$$\left[\mathbf{C}_{\mathrm{A}}\right] = \left[\mathbf{C}_{\mathrm{B}}\right] = \mathbf{I}; \;\; \left[\mathbf{D}_{\mathrm{A}}\right] = \left[\mathbf{D}_{\mathrm{B}}\right] = \begin{bmatrix} \dfrac{1}{EIk^3} & 0 \\ 0 & \dfrac{1}{EIk^2} \end{bmatrix}; \quad \left[\mathbf{C}_{\mathrm{B2}}\right] = \begin{bmatrix} \alpha_T & 0 \\ 0 & \alpha_R \end{bmatrix} \tag{239}$$

A simple way to obtain Eq. (238) is to relate each matrix to its function in the equation: the identity matrices relate the equations on the right with the equations on the left and indicate that they must be equal. These are clearly the boundary conditions; therefore, they are **C** (for displacement equations) or **D** (for forces equations) matrices. The matrices with the non-dimensional stiffness α and those related to α are also boundary condition matrices. Matrices multiplying the wave amplitudes **a** and **b** are the matrices of nodal forces and nodal displacements $\mathbf{\Phi}_{\mathrm{f}}$ and $\mathbf{\Phi}_{\mathrm{q}}$ respectively.

According to this, Eqs. (227) and (228) are reformulated as

$$\begin{bmatrix} \mathbf{C}_A\boldsymbol{\Phi}^{-}_{q,a} & -\mathbf{C}_B\boldsymbol{\Phi}^{+}_{q,b} \\ \mathbf{D}_A\boldsymbol{\Phi}^{-}_{f,a} & -\mathbf{C}_{B2}\boldsymbol{\Phi}^{+}_{q,b} - \mathbf{D}_B\boldsymbol{\Phi}^{+}_{f,b} \end{bmatrix} \begin{Bmatrix} \mathbf{a}^{-} \\ \mathbf{b}^{+} \end{Bmatrix} = \begin{bmatrix} -\mathbf{C}_A\boldsymbol{\Phi}^{-}_{q,a} & \mathbf{C}_B\boldsymbol{\Phi}^{-}_{q,b} \\ -\mathbf{D}_A\boldsymbol{\Phi}^{+}_{f,a} & \mathbf{D}_B\boldsymbol{\Phi}^{-}_{f,b} \end{bmatrix} \begin{Bmatrix} \mathbf{a}^{+} \\ \mathbf{b}^{-} \end{Bmatrix} \tag{240}$$

Figure 40 shows reflection and transmission coefficients, together with phase changes, when the positive propagating flexural wave is assumed as the incident wave. Wave scattering gives rise to reflected and transmitted propagating and nearfiled waves. In particular, Figure 39 and 41 show the scattering associated with the reflected and transmitted nearfiled waves for the same example.

Figure 38 – Reflection of propagating flexural waves in an infinite beam with at a transverse spring when only an incident propagating flexural wave is considered. a) absolute value; b) phase. Solid blue line —: Analytical solution; Dashed red line - -: WFE solution.

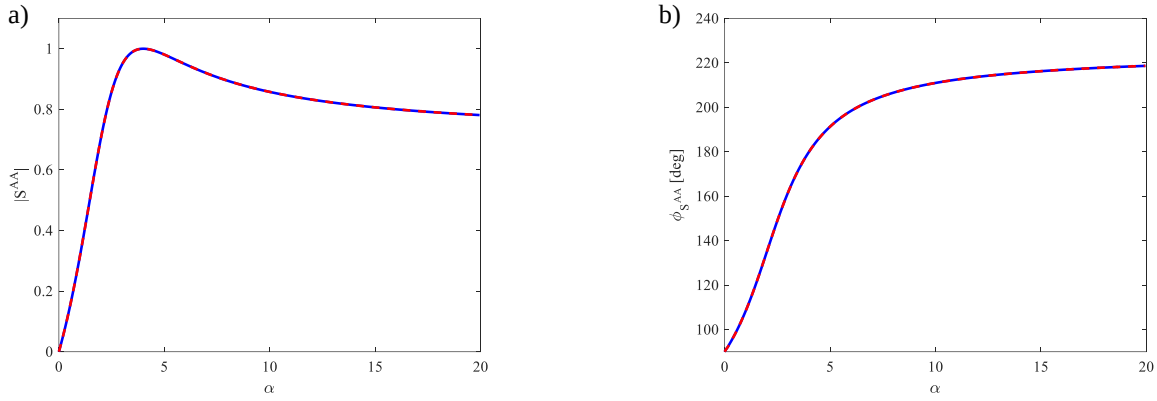

Source: Elaborated by the author

Figure 39 –Reflection of nearfiled flexural waves in an infinite beam with at a transverse spring when only an incident propagating flexural wave is considered. a) absolute value; b) phase. Solid blue line —: Analytical solution; Dashed red line - -: WFE solution.

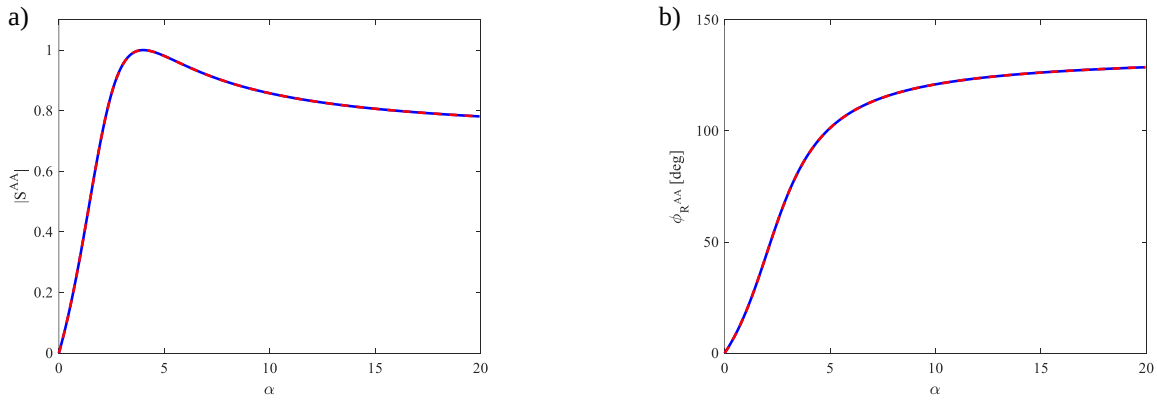

Source: Elaborated by the author

Figure 40 – Transmission of propagating flexural waves in an infinite beam with at a transverse spring when only an incident propagating flexural wave is considered. a) absolute value; b) phase. Solid blue line —: Analytical solution; Dashed red line - -: WFE solution.

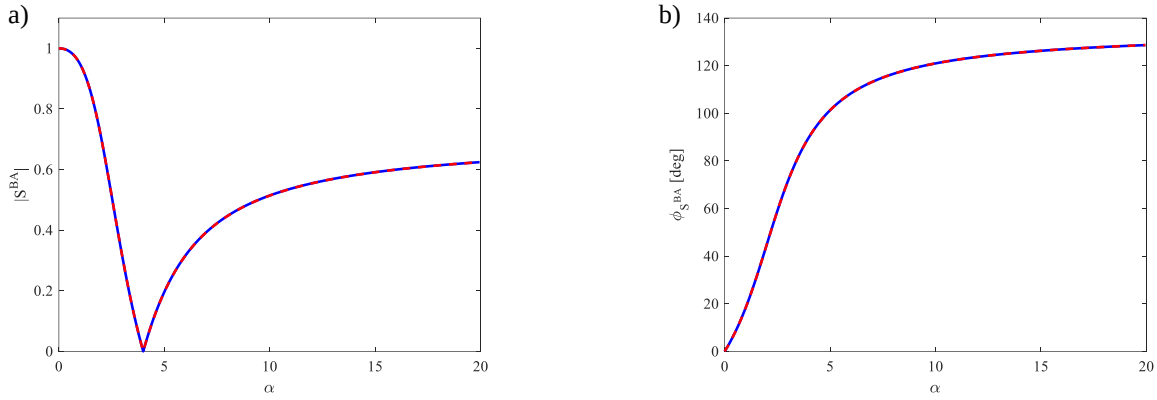

Source: Elaborated by the author

Figure 41 – Transmission of nearfield flexural waves in an infinite beam with at a transverse spring when only an incident propagating flexural wave is considered. a) absolute value; b) phase. Solid blue line —: Analytical solution; Dashed red line - -: WFE solution.

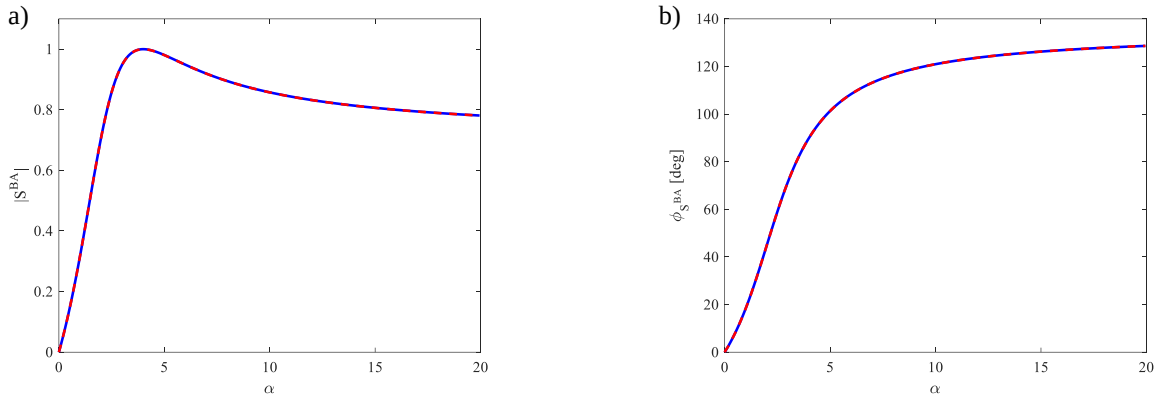

Source: Elaborated by the author

Again it can be seen that the WFE results agree very well with the analytical solutions. Results agree also very well with those presented in the literature, e.g. Mace (1984).

It can be pointed out, as discussed in Chapter 3, that the phase of the reflection and transmission coefficients can show discontinuity when they are evaluated numerically. This is due to small differences in the real or imaginary part of the coefficients, which may result in phase shifts of multiples of π radians when calculating the phase.

4.3.4 Scattering in a beam at a change of cross-sectional area

In this numerical example, two beams with different cross-sectional areas are considered as shown in Figure 18. The equilibrium conditions at the discontinuity in terms of nodal displacements and nodal forces are given by

$$\begin{aligned}\mathbf{q}_{\mathrm{A}} &= \mathbf{q}_{\mathrm{B}} \\ \mathbf{f}_{\mathrm{A}} &= \mathbf{f}_{\mathrm{B}}\end{aligned} \tag{241}$$

which can be written as functions of the wave amplitudes as

$$\begin{bmatrix} 1 & 1 \\ -ik_{\mathrm{A}} & -k_{\mathrm{A}} \end{bmatrix}\mathbf{a}^{+} + \begin{bmatrix} 1 & 1 \\ ik_{\mathrm{A}} & k_{\mathrm{A}} \end{bmatrix}\mathbf{a}^{-} = \begin{bmatrix} 1 & 1 \\ -ik_{\mathrm{B}} & k_{\mathrm{B}} \end{bmatrix}\mathbf{b}^{+} + \begin{bmatrix} 1 & 1 \\ ik_{\mathrm{B}} & k_{\mathrm{B}} \end{bmatrix}\mathbf{b}^{-} \tag{242}$$

$$\begin{bmatrix} iE_{\mathrm{A}}I_{\mathrm{A}}k_{\mathrm{A}}^{3} & -E_{\mathrm{A}}I_{\mathrm{A}}k_{\mathrm{A}}^{3} \\ -E_{\mathrm{A}}I_{\mathrm{A}}k_{\mathrm{A}}^{2} & E_{\mathrm{A}}I_{\mathrm{A}}k_{\mathrm{A}}^{2} \end{bmatrix}\mathbf{a}^{+} + \begin{bmatrix} -iE_{\mathrm{A}}I_{\mathrm{A}}k_{\mathrm{A}}^{3} & E_{\mathrm{A}}I_{\mathrm{A}}k_{\mathrm{A}}^{3} \\ -E_{\mathrm{A}}I_{\mathrm{A}}k_{\mathrm{A}}^{2} & E_{\mathrm{A}}I_{\mathrm{A}}k_{\mathrm{A}}^{2} \end{bmatrix}\mathbf{a}^{-} = \begin{bmatrix} iE_{\mathrm{B}}I_{\mathrm{B}}k_{\mathrm{B}}^{3} & -E_{\mathrm{B}}I_{\mathrm{B}}k_{\mathrm{B}}^{3} \\ -E_{\mathrm{B}}I_{\mathrm{B}}k_{\mathrm{B}}^{2} & E_{\mathrm{B}}I_{\mathrm{B}}k_{\mathrm{B}}^{2} \end{bmatrix}\mathbf{b}^{+} + \begin{bmatrix} -iE_{\mathrm{B}}I_{\mathrm{B}}k_{\mathrm{B}}^{3} & E_{\mathrm{B}}I_{\mathrm{B}}k_{\mathrm{B}}^{3} \\ -E_{\mathrm{B}}I_{\mathrm{B}}k_{\mathrm{B}}^{2} & E_{\mathrm{B}}I_{\mathrm{B}}k_{\mathrm{B}}^{2} \end{bmatrix}\mathbf{b}^{-} \tag{243}$$

using again a matrix notation, it gives

$$\begin{cases} \mathbf{C}_{\mathrm{A}}\left(\boldsymbol{\Phi}_{\mathrm{q,a}}^{+}\mathbf{a}^{+} + \boldsymbol{\Phi}_{\mathrm{q,a}}^{-}\mathbf{a}^{-}\right) = \mathbf{C}_{\mathrm{B}}\left(\boldsymbol{\Phi}_{\mathrm{q,b}}^{+}\mathbf{b}^{+} + \boldsymbol{\Phi}_{\mathrm{q,b}}^{-}\mathbf{b}^{-}\right) \\ \mathbf{D}_{\mathrm{A}}\left(\boldsymbol{\Phi}_{\mathrm{f,a}}^{+}\mathbf{a}^{+} + \boldsymbol{\Phi}_{\mathrm{f,a}}^{-}\mathbf{a}^{-}\right) = \mathbf{D}_{\mathrm{B}}\left(\boldsymbol{\Phi}_{\mathrm{f,b}}^{+}\mathbf{b}^{+} + \boldsymbol{\Phi}_{\mathrm{f,b}}^{-}\mathbf{b}^{-}\right) \end{cases} \tag{244}$$

therefore, the scattering matrix can be calculated by solving Eq. (245). In addition, in this case $\mathbf{C}_{\mathrm{A}} = \mathbf{C}_{\mathrm{B}} = \mathbf{D}_{\mathrm{A}} = \mathbf{D}_{\mathrm{B}} = \mathbf{I}$.

$$\mathbf{S} = \begin{bmatrix} \mathbf{C}_{\mathrm{A}}\boldsymbol{\Phi}_{\mathrm{q,a}}^{-} & -\mathbf{C}_{\mathrm{B}}\boldsymbol{\Phi}_{\mathrm{q,b}}^{+} \\ \mathbf{D}_{\mathrm{A}}\boldsymbol{\Phi}_{\mathrm{f,a}}^{-} & -\mathbf{D}_{\mathrm{B}}\boldsymbol{\Phi}_{\mathrm{f,b}}^{+} \end{bmatrix}^{-1}\begin{bmatrix} -\mathbf{C}_{\mathrm{A}}\boldsymbol{\Phi}_{\mathrm{q,a}}^{+} & \mathbf{C}_{\mathrm{B}}\boldsymbol{\Phi}_{\mathrm{q,b}}^{-} \\ -\mathbf{D}_{\mathrm{A}}\boldsymbol{\Phi}_{\mathrm{f,a}}^{+} & \mathbf{D}_{\mathrm{B}}\boldsymbol{\Phi}_{\mathrm{f,b}}^{-} \end{bmatrix} \tag{245}$$

For this case, the two sections are modelled using Euler-Bernoulli beam finite elements and the eigenvectors $\boldsymbol{\Phi}$ are found by solving the eigenvalue problem shown in Chapter 2. Figure 42 shows the comparison of the bending propagating reflection coefficient calculated for the case with an area change as in Figure 18 and a propagating incident wave. Figure 43

shows the comparison of the nearfield reflection coefficients and phase. The results for the transmission coefficient are shown in Figures 44 and 45, for the propagating bending and nearfield transmitted modes respectively.

Figure 42 – Reflection of propagating flexural waves in a beam with a change of cross-sectional area when only an incident propagating flexural wave is considered. a) absolute value; b) phase. Solid blue line —: Analytical solution; Dashed red line - -: WFE solution.

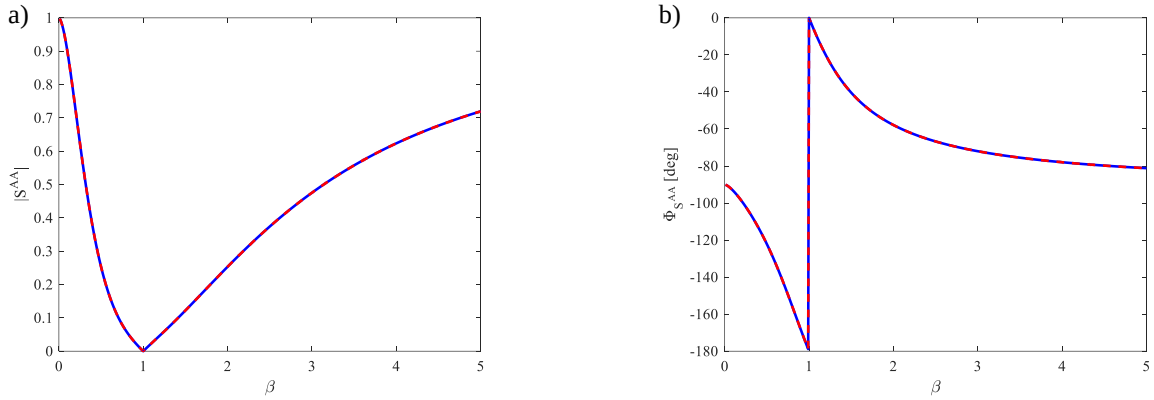

Source: Elaborated by the author

Figure 43 – Reflection of nearfield flexural waves in a beam with a change of cross-sectional area when only an incident propagating flexural wave is considered. a) absolute value; b) phase. Solid blue line —: Analytical solution; Dashed red line - -: WFE solution.

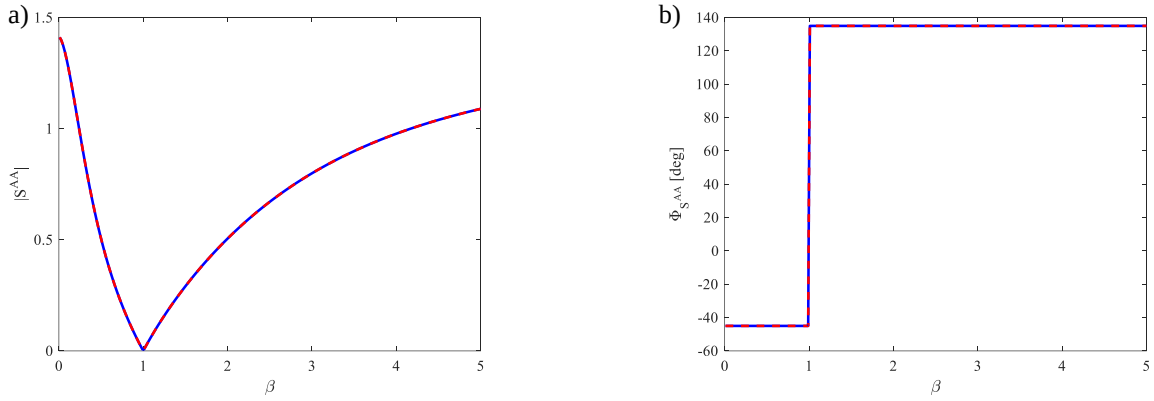

Source: Elaborated by the author

Figure 44 – Transmission of propagating flexural waves in a beam with a change of cross-sectional area when only an incident propagating flexural wave is considered. b) phase. Solid blue line —: Analytical solution; Dashed red line - - : WFE solution.

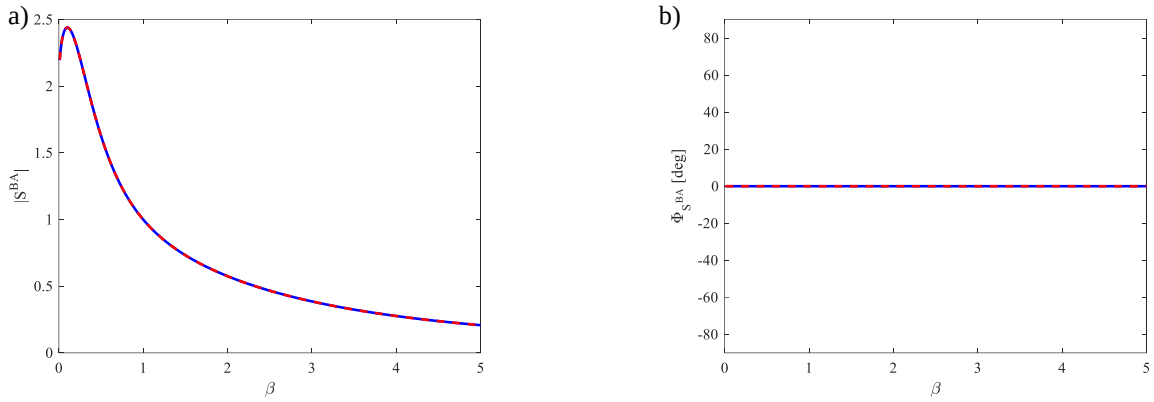

Source: Elaborated by the author

Figure 45 – Transmission of nearfield flexural waves in a beam with a change of cross-sectional area when only an incident propagating flexural wave is considered. a) absolute value; b) phase. Solid blue line —: Analytical solution; Dashed red line - - : WFE solution.

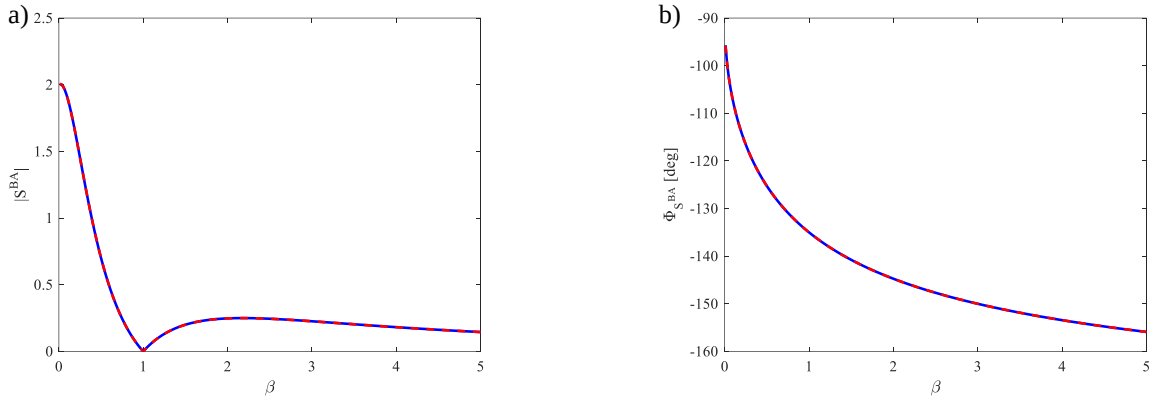

Source: Elaborated by the author

4.4 WAVE SCATTERING IN TWO CONSECUTIVE DISCONTINUITIES USING WFE ANALYSIS

4.4.1 Wave scattering in a rod with two discontinuities

In this numerical example, the case of a rod with a change of cross-sectional area of finite length as in Figure 23 is numerically studied using the WFE. As shown in Chapter 3, the scattering matrices are given by

$$
\begin{aligned}
\mathbf{S}^{AB} &= \mathbf{S}_1^{AC}\mathbf{T}_C\left(\mathbf{I}-\mathbf{T}_C^{-1}\mathbf{S}_2^{CC}\mathbf{T}_C\mathbf{S}_1^{CC}\right)^{-1}\mathbf{S}_2^{CB} \\
\mathbf{S}^{AA} &= \mathbf{S}_1^{AA}+\mathbf{S}_1^{AC}\mathbf{T}_C\left(\mathbf{I}-\mathbf{T}_C^{-1}\mathbf{S}_2^{CC}\mathbf{T}_C\mathbf{S}_1^{CC}\right)^{-1}\mathbf{S}_2^{CC}\mathbf{T}_C\mathbf{S}_1^{CA} \\
\mathbf{S}^{BA} &= \mathbf{S}_2^{BC}\mathbf{T}_C^{-1}\left(\mathbf{I}-\mathbf{T}_C\mathbf{S}_1^{CC}\mathbf{T}_C^{-1}\mathbf{S}_2^{CC}\right)^{-1}\mathbf{S}_1^{CA} \\
\mathbf{S}^{BB} &= \mathbf{S}_2^{BB}+\mathbf{S}_2^{BC}\mathbf{T}_C^{-1}\left(\mathbf{I}-\mathbf{T}_C\mathbf{S}_1^{CC}\mathbf{T}_C^{-1}\mathbf{S}_2^{CC}\right)^{-1}\mathbf{S}_1^{CC}\mathbf{T}_C^{-1}\mathbf{S}_2^{CB}
\end{aligned}
\tag{246}
$$

where **A** refers to the first waveguide, **B** to the waveguide in the middle (damage) and **C** to the last waveguide that is equal to **A**. By using the scattering coefficients obtained in Sections 4.3 and 4.4, Eq.(43) can be easily solved and gives the scattered wave amplitudes

$$
\begin{Bmatrix} \mathbf{a}^{-} \\ \mathbf{c}_1^{+} \end{Bmatrix} = \begin{bmatrix} \mathbf{S}_1^{AA} & \mathbf{S}_1^{AC}\mathbf{T}_C^{-1} \\ \mathbf{S}_1^{CA} & \mathbf{S}_1^{CC}\mathbf{T}_C^{-1} \end{bmatrix} \begin{Bmatrix} \mathbf{a}^{+} \\ \mathbf{c}_2^{-} \end{Bmatrix} \tag{247}
$$

$$
\begin{Bmatrix} \mathbf{c}_2^{-} \\ \mathbf{b}^{+} \end{Bmatrix} = \begin{bmatrix} \mathbf{S}_2^{CC}\mathbf{T}_C & \mathbf{S}_2^{CB} \\ \mathbf{S}_2^{BC}\mathbf{T}_C & \mathbf{S}_2^{BB} \end{bmatrix} \begin{Bmatrix} \mathbf{c}_1^{+} \\ \mathbf{b}^{-} \end{Bmatrix} \tag{248}
$$

The case of 50% reduction of the area to model the discontinuity, that is the cross-sectional area of **C** is half the cross-sectional area of **A** and **B** (note that **B** is equal to **A**), is considered. The scattering reflection and transmission coefficients are calculated and compared with the analytical solution as it can be seen in Figure 46.

Figure 46 – Scattering coefficients for the two consecutive area changes in a rod using WFE for 50% damage. a) absolute value; b) phase. Solid blue line —: Analytical solution; Dashed red line - - : WFE solution.

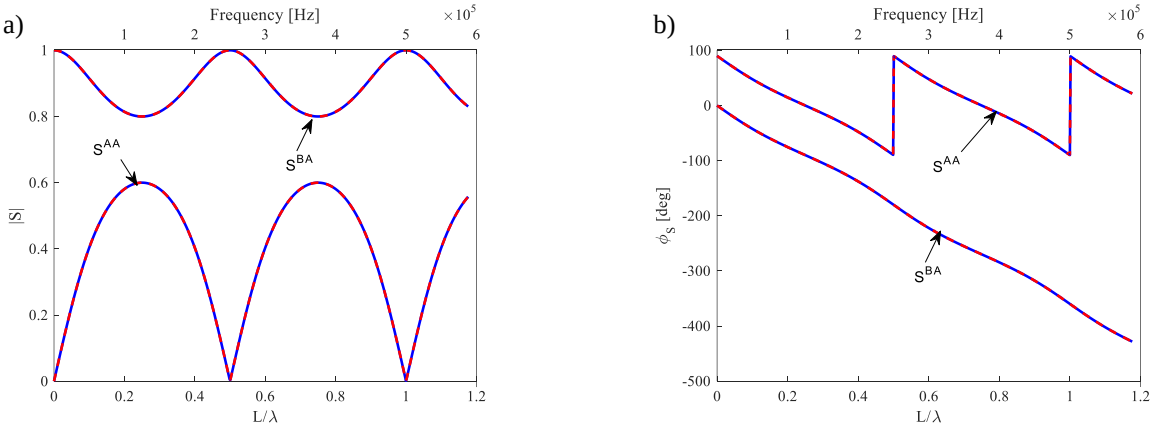

Source: Elaborated by the author

Figure 46 shows that the results agree very well with those obtained analytically. These are discussed in details in Section 3.4.2

4.4.2 Wave scattering in a beam with two discontinuities

Following the same procedure adopted for the rod example, a beam with a finite length discontinuity modelled as a change of the cross-sectional area is considered. The example is shown in Figure 23, Chapter 3. The WFE results are again compared with those obtained analytically. The results are plotted for the case of a propagating bending incident wave.

Figure 47 – Reflection coefficient of the flexural propagating wave in a beam with two consecutive area changes using WFE for 50% damage and an incident propagating flexural wave. a) absolute value; b) phase. Solid blue line —: Analytical solution; Dashed red line - - : WFE solution.

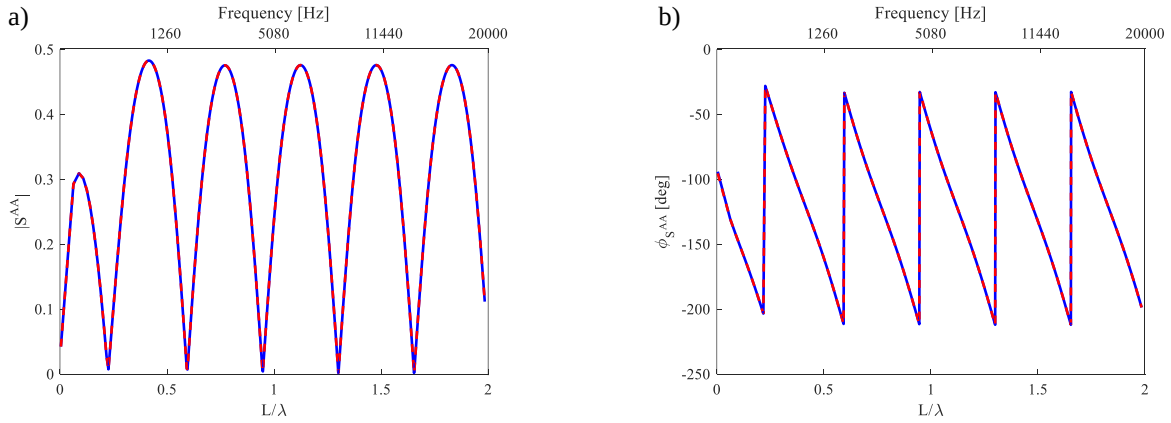

Source: Elaborated by the author

Figure 48 – Transmission coefficient of the flexural propagating wave in a beam with two consecutive area changes using WFE for 50% damage and an incident propagating flexural wave. a) absolute value; b) phase. Solid blue line —: Analytical solution; Dashed red line - - : WFE solution.

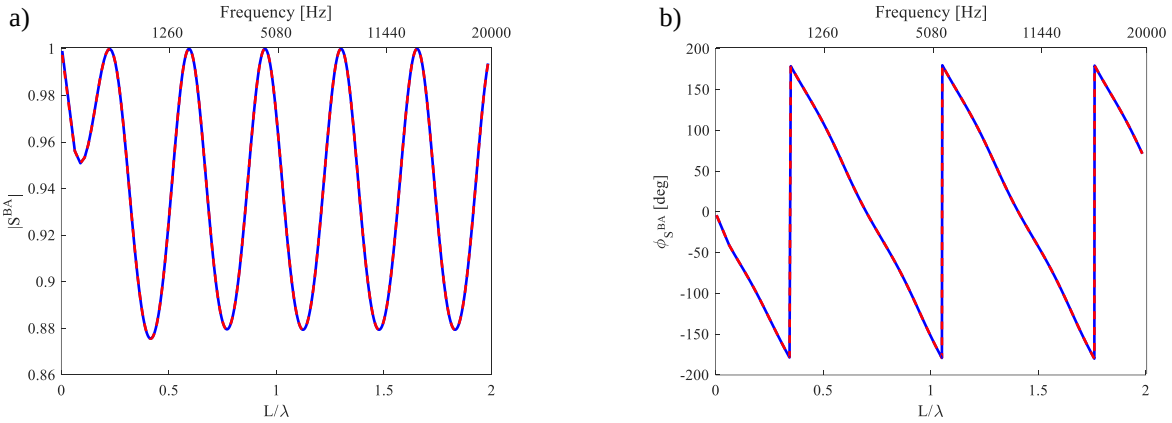

Source: Elaborated by the author

Figure 49 – Reflection coefficient of the flexural nearfield wave in a beam with two consecutive area changes using WFE for 50% damage and an incident propagating flexural wave. a) absolute value; b) phase. Solid blue line —: Analytical solution; Dashed red line - - : WFE solution.

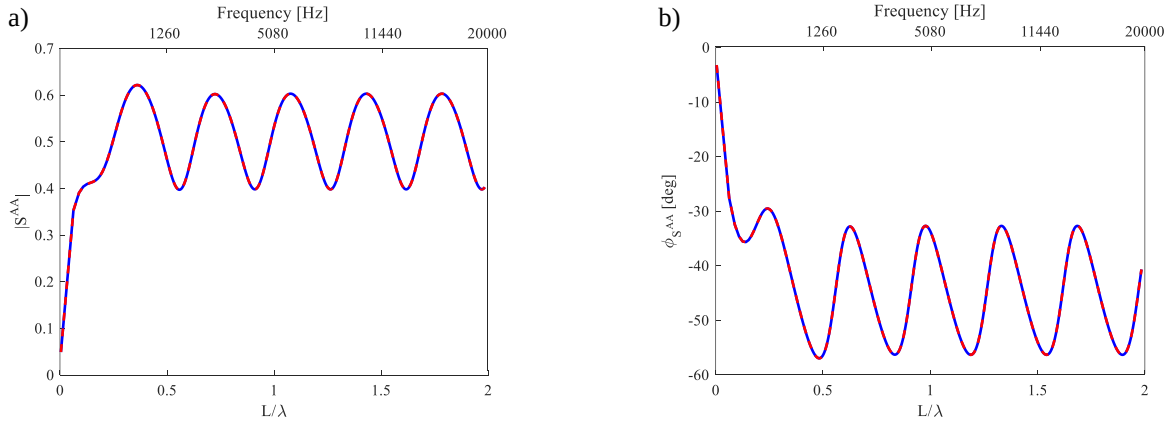

Source: Elaborated by the author

Figure 50 – Transmission coefficient of the flexural nearfield wave in a beam with two consecutive area changes using WFE for 50% damage and an incident propagating flexural wave. a) absolute value; b) phase. Solid blue line —: Analytical solution; Dashed red line - - : WFE solution.

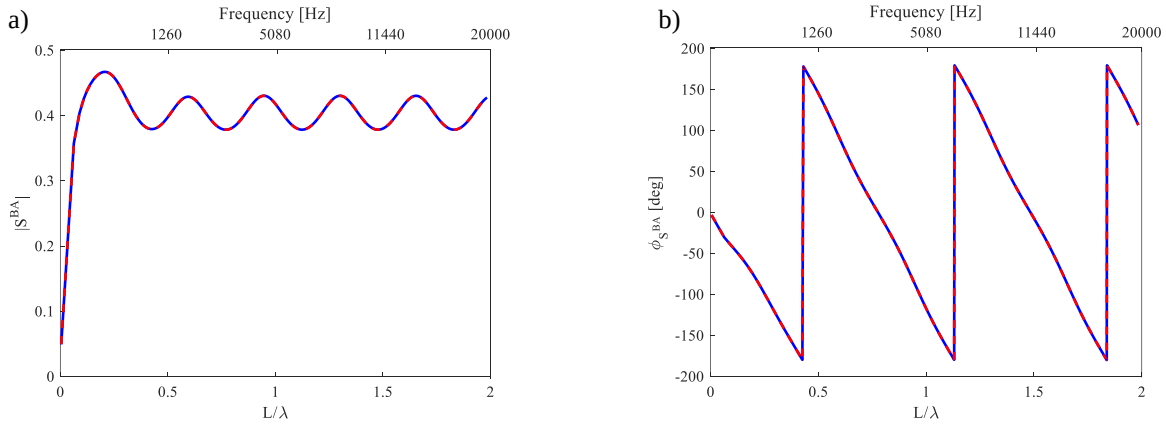

Source: Elaborated by the author

The WFE results agree very well with the analytical solution for the frequency range considered. From visual inspection, the results agree very well with those presented by Ayala Castillo, Lopes Junior and Brennan (2015).

4.5 CONCLUSIONS

In this chapter, the WFE method was applied to find the reflection and transmission coefficients of a rod and an Euler-Bernoulli beam following the examples solved analytically in Chapter 3. The WFE dispersion curves and wavemodes were used to describe the nodal displacements and nodal forces following the wave matrix formulation described in Chapter 2.

WFE results were compared with those obtained by analytical solutions. Since the FE models are of a simple rod and an EB beam, no numerical errors were found in evaluating the scattering matrix and numerical results were in perfect agreement with those obtained from the analytical models. In particular, the nodal displacements and nodal forces were easily described using all the wavemodes obtained from the WFE eigenvalue problem.

In the next chapter, the beam will be discretized using more elements meshed through the cross-section in order to allow the evaluation of the wave scattering up to high frequencies. The case of a non-symmetrical change of cross-sectional area will be also considered.

5 WAVE SCATTERING FROM SYMMETRIC AND NON-SYMMETRIC DISCONTINUITIES IN ONE-DIMENSIONAL WAVEGUIDES

5.1 INTRODUCTION

This chapter shows some results for reflection and transmission of waves propagating in one-dimensional waveguides with a change in the cross-sectional area. The WFE method is applied and the waveguides are discretized using 2D standard FE plane elements. The plane elements are defined by four nodes, each node having two degrees of freedom: translations in the *x* and *y* directions. The FE matrices of a small segment of waveguides **A** and **B** are used for the WFE model. Which in turn, are used to obtain the dispersion curves and wavemodes. From this, the scattering matrix is then obtained as described in Chapter 2.

The material properties are listed in Table 4.

Table 4 – Material properties of the waveguide.

Property	Symbol	Value	Units
Young's Modulus	E	206×10^9	N/m^2
Density	ρ	7.8×10^3	kg/m^3
Poisson's ratio	υ	14	mm

Source: Elaborated by the author

In this chapter, two kinds of discontinuities are studied: symmetric and non-symmetric changes of cross-sectional area. Both cases are evaluated for a point discontinuity and a finite length (two consecutive changes of cross-sectional areas) discontinuity configurations. The finite length case is evaluated for three different situations of damage length, which are better explained in the next sections. For the finite length case, the influence of the type of incident wave (symmetric S_0 and anti-symmetric A_0 Lamb modes) and the influence of the severity of the damage to the scattering results are investigated. These can be useful in practical damage detection applications using ND Testing techniques for SHM.

5.2 WFE MODEL USING 2D PLANE ELEMENTS

5.2.1 Introduction

In this section, the WFE model of a one-dimensional waveguide, modelled using plane elements is presented. Dispersion curves with complex wavenumbers numbers are obtained and compared with those obtained analytically while the mode shapes are shown, in particular showing the behaviour of higher order modes. If the FE model has $2n$ DOF, then there are n DOF at each side of the segment, therefore, the solution of the WFE eigenvalue problem will

give *n* eigenvalues (wavenumbers) and *n* wavemodes. Among these wavenumbers, some of them are pure positive, which correspond to the propagating modes, some of them are pure imaginary, which correspond to the nearfield modes, some of them are numerical artifacts, which do not correspond to any actual wavemode and finally some of them are complex conjugate, which correspond to the attenuated modes (see Chapter 2 for more information on wavemodes). In the following solutions, for the sake of simplicity, only the results for the first two pairs of complex conjugate modes are plotted, although they are used on the calculation of the scattering coefficients and power coefficients.

5.2.2 Dispersion curves

Consider a waveguide with a single change of cross-sectional area. The waveguide is divided into two sections: waveguide **A** and waveguide **B**. Both sections are modelled using conventional plane elements as shown in Figure 51.

Figure 51 – FE model using plane elements of a section of the two waveguides **A** and **B**.

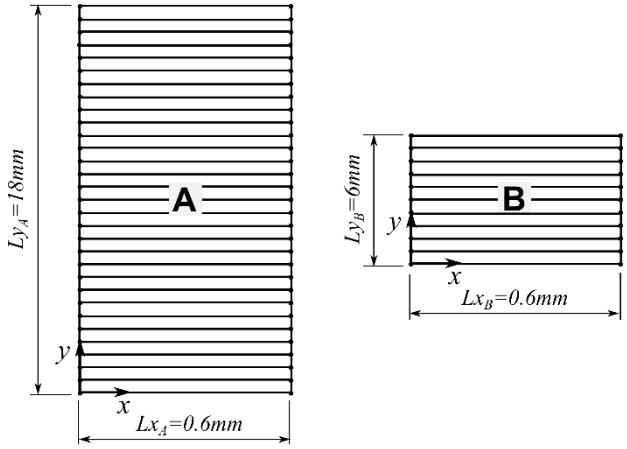

Source: Elaborated by the author

As in standard FE analysis a convergence study was carried out. Results obtained for different FE discretization were compared in terms of the dispersion curves obtained using the WFE method. In the numerical example presented in this section, waveguide A is discretized using 30 plane elements and waveguide B using 10 plane elements, which are meshed through the cross-section. The number of elements was found to be sufficient for obtaining accurate solutions up to 250kHz. Considering the frequency range of interest, the computational cost is extremely small.

By following the procedure described in Chapter 2, the dispersion curves and wavemodes are obtained using the WFE method and the results at low frequency are compared with the analytical solutions for axial and flexural wave propagation, viz. wave propagation in a rod and in Euler-Bernoulli beam (GRAFF, 1975). Wavenumbers and wavemodes are sorted according to the order shown in Chapter 2, as it can be seen in Eq. (22), where the numbers follow the sequence: propagating modes, nearfield modes, attenuating with negative imaginary components and attenuating with positive imaginary components.

$$\mathbf{k}^{+} = \begin{bmatrix} \mathbf{k}_{\mathrm{P}}^{+} & \mathbf{k}_{\mathrm{N}}^{+} & \mathbf{k}_{\mathrm{A-}}^{+} & \mathbf{k}_{\mathrm{A+}}^{+} \end{bmatrix}$$
$$\mathbf{k}^{-} = \begin{bmatrix} \mathbf{k}_{\mathrm{P}}^{-} & \mathbf{k}_{\mathrm{N}}^{-} & \mathbf{k}_{\mathrm{A-}}^{-} & \mathbf{k}_{\mathrm{A+}}^{-} \end{bmatrix} \tag{249}$$

Figure 52 shows the comparison of the dispersion curves for the positive propagating wavemodes.

Figure 52 – Dispersion curves obtained by WFE and analytically. a) Section A; b) Section B. Solid blue line —: Analytical solution; Dashed red line ---: WFE solution.

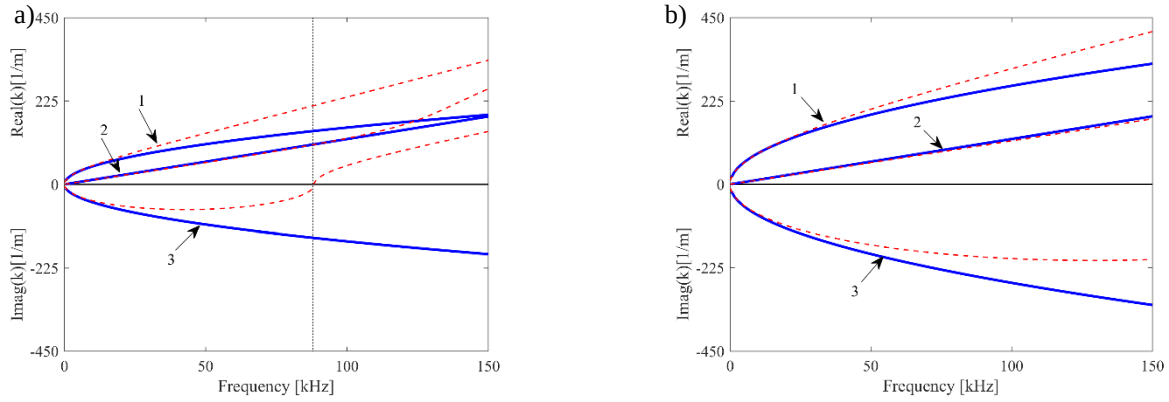

Source: Elaborated by the author

In Figure 52, the numbered arrows indicate the wave mode type, where 1 corresponds to the bending propagating (A_0 Lamb) mode, 2 corresponds to the longitudinal propagating (S_0 Lamb) mode and 3 corresponds to the bending nearfield mode. Modes 1 and 3 are compared with those obtained for the Euler-Bernoulli beam model and mode 2 is compared with the rod analytical model.

It can be seen that the analytical solution agrees with the WFE solution at low frequency due to the limiting hypothesis in the analytical models. Simple analytical models, such as those used here for comparison, are in fact not able to describe high-frequency behaviour. As the

frequency goes higher, the wavelength becomes comparable with the waveguide cross-section, and the hypothesis in the rod and Euler-Bernoulli theories are no longer valid. This is particularly evident for the nearfield mode (wavemode 3) because the Euler-Bernoulli beam does not take into account the wavemode conversion and cut-off of the first antisymmetric A_1 Lamb mode. In fact, some wavemodes "change" their nature as frequency increases, giving rise to different wavemodes which start propagating at cut-off frequencies. In the frequency range considered in Figure 52a and 2b, there is only one cut-off frequency at 88kHz. This dispersion behaviour is better studied in the next section, where higher order modes are introduced.

5.2.3 Wave modes

Complex dispersion curves for waveguide **A** up to 250kHz are shown in Figure 53. Figure 53 shows wavenumbers associated with a wave propagating in the positive direction and nearfield and attenuated waves decaying in the positive direction. In particular, only complex wavenumbers having positive real parts are plotted.

Figure 53 – Dispersion curves for steel beams. ——— propagating modes; – · – : evanescent modes; – – – : complex modes (note that complex modes occur as a pair of complex conjugate modes, and only one of the pair is shown here); The numbers relate to different wave modes, and the vertical lines correspond to cut-off frequencies.

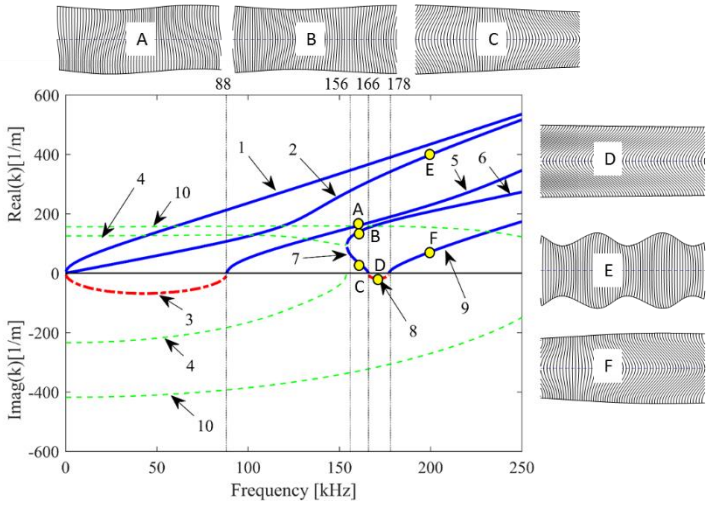

Source: Elaborated by the author

As shown in Chapter 2, the attenuated modes (modes with complex conjugate wavenumbers) appear in pairs of λ_i and $1/\lambda_i$, which correspond to the $k^+_{\mathrm{A}+}$ and $k^+_{\mathrm{A}-}$ modes respectively. In this case, only the wavenumbers with positive real and negative imaginary components are plotted, which means that the k^+_{P}, k^+_{N} and $k^+_{\mathrm{A}+}$ are shown. The other attenuated

mode (k^{+}_{A-}) does not appear in this plot since the wavenumbers with positive imaginary parts are not being shown, however, when arriving at a cut-off frequency they may convert into the positive propagating mode (with a real positive wavenumber) and therefore appear in this plot from that point onward. This is the case for branch 4. Note that for this plot the complex conjugate wavenumbers are composed of a combination of two branches, one to represent the real part and the other to represent the imaginary part of the complex conjugate wavenumber.

Branches 1, 2 and 3 are the same as commented in the previous section, however, in this case, four cut-off frequencies can be seen at 88kHz, 156kHz, 166kHz and 178kHz. Following the nomenclature shown in chapter 2, there are some particular points of interests in Figure 53 indicated by the letters from A to F, where the letters P, N and A refers to propagating, nearfield and attenuated wave modes respectively:

A. The branch 5 (P) is originated from the branch 3 (N) at the first cut-off frequency (88kHz). Branch 5 is an antisymmetric axial mode, see Figure 54 for a representation of symmetric and antisymmetric wave modes;
B. when Branch 4, which is an attenuated (A) mode, arrives at the second cut-off frequency (156kHz), it divides into branches 6 and 7. Branch 6 comes from the negative imaginary attenuated mode (A+) and it is a propagating (P) mode. This branch is a symmetric axial mode with a transverse component;
C. Branch 7 cuts off from branch 4 with the positive imaginary component (A-). This mode is also a symmetric axial mode with a transverse component. However, it has the particularity of having the group velocity in the opposite direction of the phase velocity;
D. Branch 8 originates from branch 7 at the third cut-off frequency (166kHz) and it is a nearfield mode;
E. above a certain frequency, between the first and the second cut-off frequency, the pure axial (longitudinal) mode in branch 2 starts having an increasing transverse component and change behaviour to a symmetric axial mode with a significant transverse component;
F. At the fourth cut-off frequency (178kHz) branch 8 becomes branch 9 which is similar in nature to branches 6 and 7, with the phase velocity in the same direction as the group velocity.

Branch 10 is the second A+ mode and its cut-off frequency lies above the studied frequency range. Just as an observation, branch 10 also becomes propagating mode, in a similar way to the branch 4. In fact, this also happens with the other attenuating modes, however, the larger the wavenumber, the higher the cut-off frequencies for that mode to became a propagating mode. Further information on the wavemodes and cut-off frequencies can be found in the literature on Lamb wave propagation (AULD, 1973; GRAFF, 1975). Figure 54 shows the representation of a symmetric and antisymmetric mode.

Figure 54 – Symmetric and antisymmetric wave modes.

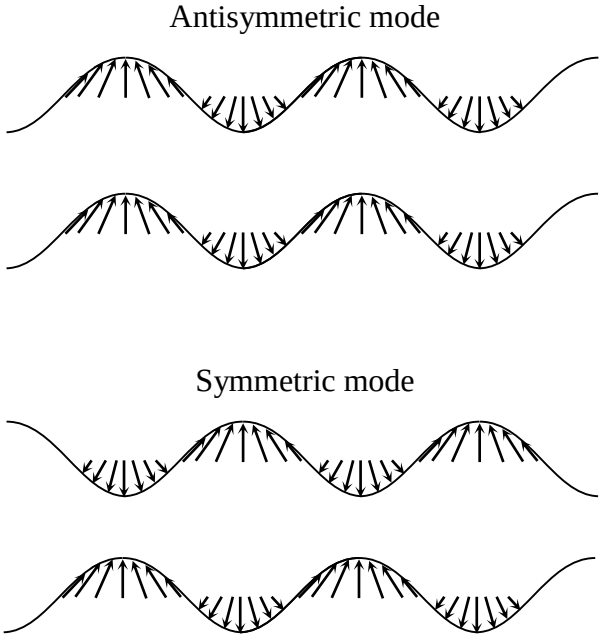

Source: Adapted from Su and Ye (2009)

5.3 SCATTERING: SYMMETRIC CHANGE OF AREA

5.3.1 Introduction

In this section, wave scattering from a symmetric change of cross-sectional area is investigated up to high frequency. As shown in Chapter 2, the analytical solution for the symmetric case at low frequency can be easily found and was used to validate the WFE model.

Consider a one-dimensional waveguide with a change of cross-sectional area (step discontinuity) and double change of cross-sectional area (notch). A small segment of the waveguide is meshed through the cross-section using a stack of standard FE plane elements. As shown in Chapter 2, the FE model is obtained for waveguides **A** and **B**, and the WFE solution of the dispersion curves and wavemodes are obtained as shown in Section 5.2. Scattering

coefficients, power coefficients and time-averaged kinetic energies are then evaluated and discussed for numerical examples.

5.3.2 Point discontinuity

Consider the case of a point discontinuity as shown in Figure 55.

Figure 55 – FE model using plane elements of a single symmetric change of cross-sectional area.

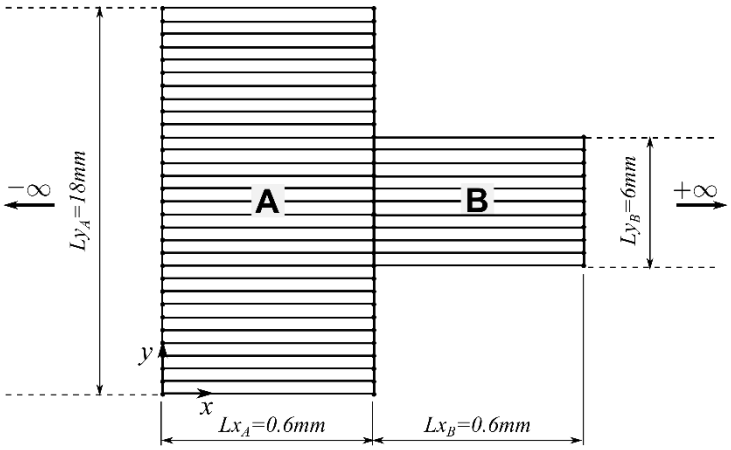

Source: Elaborated by the author

Equilibrium and displacement continuity are

$$\begin{aligned}\mathbf{C}_{\mathsf{A}}\mathbf{q}_{\mathsf{A}} &= \mathbf{C}_{\mathsf{B}}\mathbf{q}_{\mathsf{B}}\\ \mathbf{D}_{\mathsf{A}}\mathbf{f}_{\mathsf{A}} &= \mathbf{D}_{\mathsf{B}}\mathbf{f}_{\mathsf{B}}\end{aligned} \tag{250}$$

If the number of DOF in **A** and **B** are respectively n_{A} and n_{B}, the dimensions of the matrices that describe the boundary conditions are

$$\left(\mathbf{C}_{\mathsf{A}}\right)_{n_{\mathsf{A}}\times n_{\mathsf{A}}}, \left(\mathbf{C}_{\mathsf{B}}\right)_{n_{\mathsf{A}}\times n_{\mathsf{B}}}, \left(\mathbf{D}_{\mathsf{A}}\right)_{n_{\mathsf{A}}\times n_{\mathsf{A}}} \text{ and } \left(\mathbf{D}_{\mathsf{B}}\right)_{n_{\mathsf{A}}\times n_{\mathsf{B}}} \tag{251}$$

Moreover, if the degrees of freedom connecting both waveguides are contained in vectors $\mathbf{m}_{\mathsf{A}}$ and $\mathbf{m}_{\mathsf{B}}$, the matrices of boundary conditions are as follows

$$
\begin{aligned}
&\mathbf{C}_{\mathrm{A}} = \mathbf{I}_{n_{\mathrm{A}}} \\
&\left(\mathbf{C}_{\mathrm{B}}\right)_{n\times m} = \begin{cases} 1, & \text{if } n \in \mathbf{m}_{\mathrm{A}} \text{ and } m \in \mathbf{m}_{\mathrm{B}} \text{ where } n = 1,2,\cdots,n_{\mathrm{A}} \text{ and } m = 1,2,\cdots,n_{\mathrm{B}} \\ 0, & \text{otherwise} \end{cases} \\
&\left(\mathbf{D}_{\mathrm{A}}\right)_{n\times m} = \begin{cases} 1, & \text{if } n \in \mathbf{m}_{\mathrm{A}} \text{ and } m \in \mathbf{m}_{\mathrm{A}} \text{ where } n = 1,2,\cdots,n_{\mathrm{A}} \text{ and } m = 1,2,\cdots,n_{\mathrm{A}} \\ 0, & \text{otherwise} \end{cases} \\
&\mathbf{D}_{\mathrm{B}} = \mathbf{C}_{\mathrm{B}}
\end{aligned}
\tag{252}
$$

where $\mathbf{I}_{n_{\mathrm{A}}}$ and $\mathbf{I}_{n_{\mathrm{B}}}$ are identity matrices with dimensions n_{A} and n_{B} respectively. In this specific case $\mathbf{m}_{\mathrm{A}}$ and $\mathbf{m}_{\mathrm{B}}$ are

$$
\begin{aligned}
&\mathbf{m}_{\mathrm{A}} = \left[\left(\frac{n_{\mathrm{A}} - n_{\mathrm{B}}}{2}\right)+1, \left(\frac{n_{\mathrm{A}} - n_{\mathrm{B}}}{2}\right)+2, \cdots, \left(\frac{n_{\mathrm{A}} - n_{\mathrm{B}}}{2}\right)+\frac{n_{\mathrm{B}}}{2}\right] \\
&\mathbf{m}_{\mathrm{B}} = \left[1, 2, \cdots, \frac{n_{\mathrm{B}}}{2}\right]
\end{aligned}
\tag{253}
$$

With the boundary conditions and the eigenvectors (nodal displacements and nodal forces) from the WFE solution of the FE model, the scattering matrix can be calculated by using the solution shown in Chapter 2, see Eq. (31).

5.3.2.1 Scattering coefficients

By solving the matrix inversion in Eq. (31), the scattering coefficients can be found. Only an A_0 incident wave is considered (branch 1 in Figure 53). Comparison of the results with those obtained from analytical solution for an Euler-Bernoulli beam at low frequency has shown good agreement (Figure 56).

Figure 56 – Reflection coefficients in a symmetric change of cross-sectional area. a) Reflection coefficients; b) transmission coefficients. Solid blue line ——— : propagating modes; dashed dot red line — · — : nearfield modes; dotted blue line ····· : Euler-Bernoulli solution. The numbers relate to different wave modes, and the vertical lines correspond to cut-off frequencies.

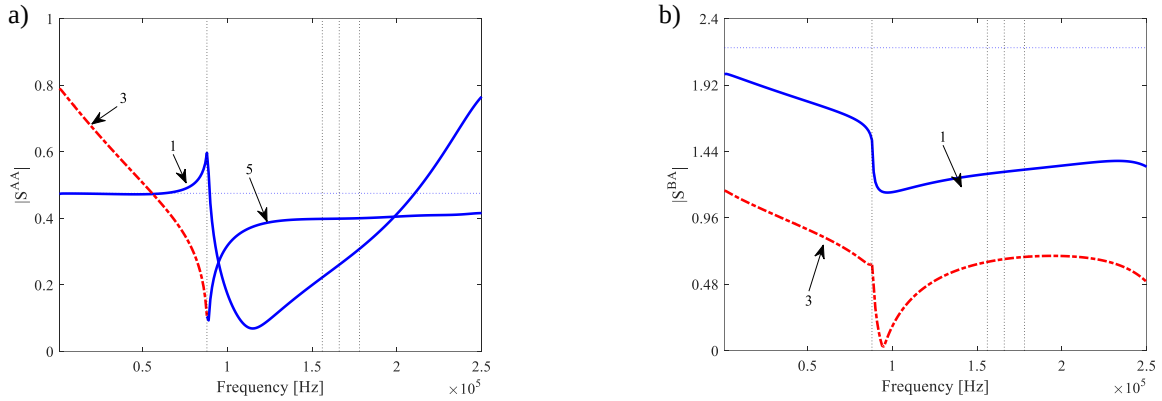

Source: Elaborated by the author

It can be seen that the WFE solution can reproduce the results of the Euler-Bernoulli solution at low frequency (frequencies lower than the first cut-off frequency) although some differences, in particular in the transmission coefficients, are due to significant differences in the models. As frequency increases, the differences in the results between analytical and numerical results get bigger. In particular, at higher frequencies, new modes start propagating and the scattering behaviour becomes more complicated due to energy redistribution amongst higher order modes. Since simple analytical models do not predict higher order modes, they are unable to give reliable results at high frequencies. At the first cut-off frequency of the thicker waveguide, Figure 56 shows a significant change in the behaviour of the wave reflected and transmitted due to the cut-off of the first antisymmetric Lamb mode and consequent energy redistribution amongst modes 1 and 5.

5.3.2.2 Power coefficients

The power coefficients evaluated using Eq. (254), Chapter 2, are plotted in Figure 7.

$$\upsilon = \frac{\Pi_{\mathrm{R}}}{\Pi_{\mathrm{I}}} = \left|S^{\mathrm{AA}}\right|^2 \frac{P_{\mathrm{A}}^{rr}}{P_{\mathrm{A}}^{ii}}$$
$$\tau = \frac{\Pi_{\mathrm{T}}}{\Pi_{\mathrm{I}}} = \left|S^{\mathrm{BA}}\right|^2 \frac{P_{\mathrm{B}}^{tt}}{P_{\mathrm{A}}^{ii}} \qquad (254)$$

where υ and τ are the reflection and transmission power coefficients respectively.

Figure 57 – Power coefficients in a symmetric change of cross-sectional area. Solid blue line ——— : reflection power coefficient; dashed dot red line – – – : transmission power coefficient; dotted black line ····· : the sum of the power coefficients.

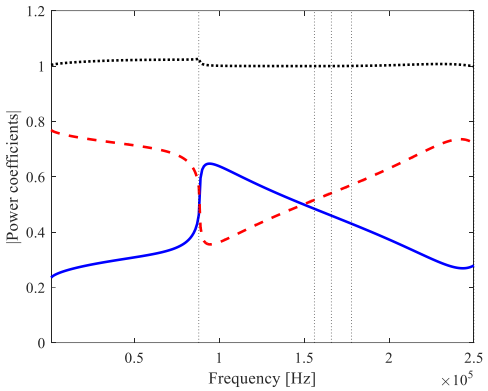

Source: Elaborated by the author

As it can be seen, since the discontinuity is conservative, it is verified that the sum of the power coefficients is close to one in the simulated frequency range. It can be seen that at the cut-off frequency, the reflected power coefficient becomes bigger than the transmitted power coefficient. Again, this happens because of the cut-off of a new mode, viz. the first antisymmetric Lamb mode. At lower frequencies the nearfield mode is present (branch 3); this does not carry energy and therefore it's power coefficient is zero. After the first cut-off frequency, the nearfield mode "converts" to a new propagating mode (branch 5) which does carry energy and energy redistribution amongst propagating modes occurs. Note that in waveguide **B** there are no cut-off frequencies in the frequency range considered, therefore there are new modes only in waveguide **A** (reflected waves). It can be seen that below the first cut-off frequency almost all the energy flow is transmitted to waveguide **B**. However, at this cut-off frequency, there is an increase in the reflected power with a decrease in the transmitted power. At higher frequency, the transmitted power gradually increases, and the reflected power gradually decreases.

5.3.2.3 Time-averaged kinetic energy

Using the Eqs. (255) obtained from Chapter 2, the time-averaged kinetic energy in the *x* and *y* directions are calculated for the incident, reflected and transmitted waves. Note that the kinetic energy content in the *y*-direction can be easily calculated by simply substituting the *x* component in Eq. (255) by the *y* component. Only propagating modes are considered in order to model far-field conditions.

$$\Gamma_{\mathrm{I}}^{x} = \frac{(i\omega)^2}{4}\left(\mathbf{a}_x^{+}\boldsymbol{\Phi}_{\mathrm{q,A},x}^{+}\right)^{H}\mathbf{M}_{\mathrm{A}}\boldsymbol{\Phi}_{\mathrm{q,A},x}^{+}\mathbf{a}_x^{+}$$
$$\Gamma_{\mathrm{R}}^{x} = \frac{(i\omega)^2}{4}\left(\mathbf{a}_x^{-}\boldsymbol{\Phi}_{\mathrm{q,A},x}^{-}\right)^{H}\mathbf{M}_{\mathrm{A}}\boldsymbol{\Phi}_{\mathrm{q,A},x}^{-}\mathbf{a}_x^{-} \tag{255}$$
$$\Gamma_{\mathrm{T}}^{x} = \frac{(i\omega)^2}{4}\left(\mathbf{b}_x^{+}\boldsymbol{\Phi}_{\mathrm{q,B},x}^{+}\right)^{H}\mathbf{M}_{\mathrm{B}}\boldsymbol{\Phi}_{\mathrm{q,B},x}^{+}\mathbf{b}_x^{+}$$

Figure 58 – Incident kinetic energy content in a symmetric change of cross-sectional area. Solid blue line ——: kinetic energy in the *y*-direction; dashed dot red line — · - : kinetic energy in the *x*-direction. The vertical lines correspond to cut-off frequencies.

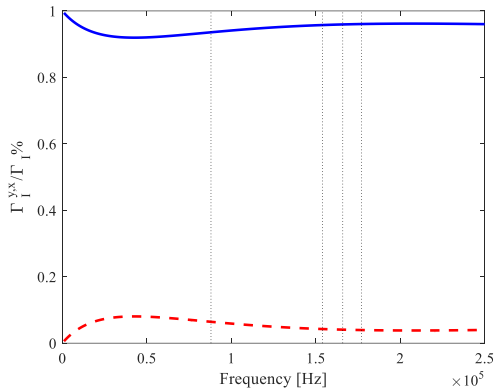

Source: Elaborated by the author

Here the components of the time-averaged incident kinetic energy in the *x* and *y*-directions are given with respect to the total time-averaged incident kinetic energy. Figure 58 shows that, for the incident wave, that is the A_0 Lamb modes, almost all of the kinetic energy is in the *y*-direction while a very small component of the energy is in the *x*-direction.

Figure 59 shows the direction component of the time-averaged kinetic energy associated with the reflected and transmitted waves.

Figure 59 – Kinetic energy content in a symmetric change of cross-sectional area. a) Reflected time-averaged kinetic energy; b) transmitted time-averaged kinetic energy. Solid blue line ——: kinetic energy in the *y*-direction; dashed dot red line — · - -: kinetic energy in the *x*-direction. The vertical lines correspond to cut-off frequencies.

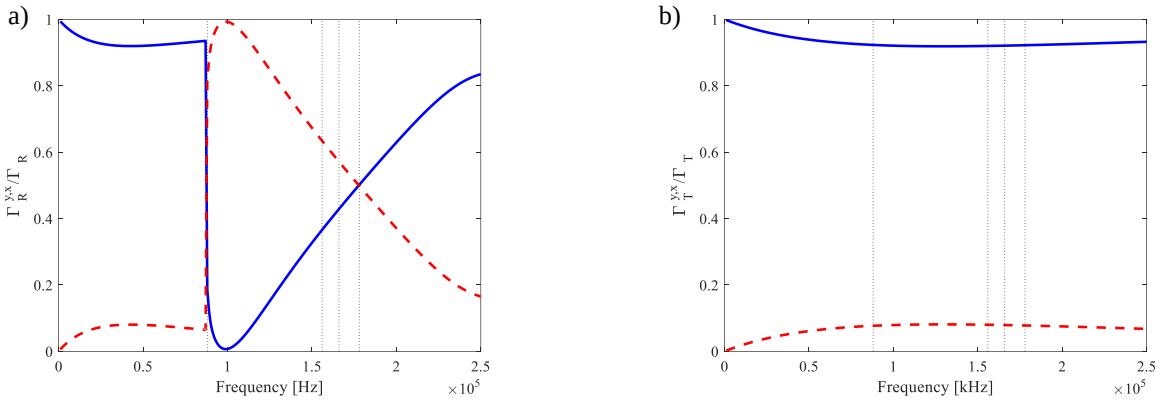

Source: Elaborated by the author

It can be seen that at low frequency the kinetic energy is predominantly in the *y*-direction in both the reflected and transmitted waves. However, at the first cut-off frequency, Figure 59a shows an abrupt decrease of the *y* component for the reflected waves due to the cut-off of the mode 5, see Figure 53. This can be used as an indication of the presence of a damage. In addition, the fact that the reflected kinetic energy has a higher conversion of energy can be exploited, which means that in this case, the reflected signal can give information about the presence of the damage.

5.3.3 Finite length discontinuity

The case of the two consecutive cross-sectional change of areas is studied in this section. This kind of discontinuity is more closely related to a model of damage due to corrosion or open crack. Three cases are investigated: in the first case, the length of the discontinuity is smaller than the smallest wavelength, in the second case the length is comparable with the smallest wavelength, while the third case simulates a discontinuity larger than the smallest wavelength. The three lengths are respectively L=2.4mm, L=20mm and L=90mm. Figure 60 shows the schematic representation of the WFE model in the case L=90mm as an example.

Figure 60 – FE model using plane elements of two consecutive symmetric changes of cross-sectional area.

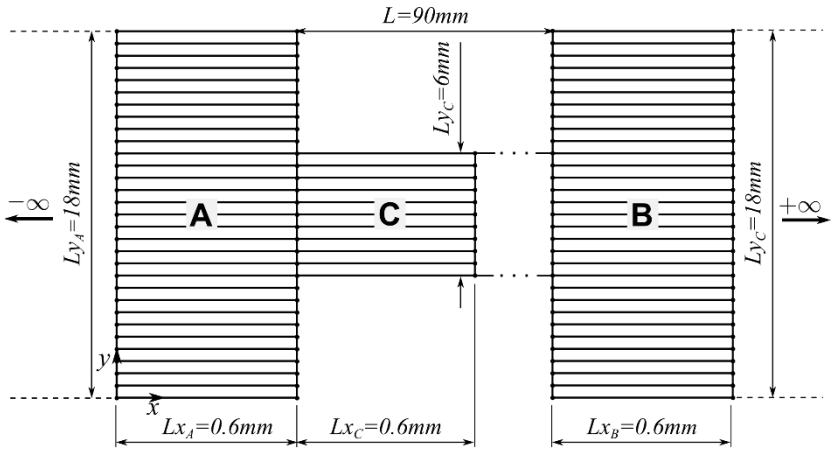

Source: Elaborated by the author

5.3.3.1 Scattering coefficients

In these examples, Eq. (43) in Chapter 2 is used for obtaining the scattering coefficients. The spatial transformation matrix $\mathbf{T}_\mathsf{C} = \mathrm{diag}\left[\exp\left(-i\mathbf{k}_\mathsf{c}L\right)\right]$ is evaluated using the wavenumbers predicted from WFE model for waveguide **C**.

$$
\begin{aligned}
\mathbf{S}^{\mathsf{AB}} &= \mathbf{S}_1^{\mathsf{AC}}\mathbf{T}_\mathsf{C}\left(\mathbf{I}-\mathbf{T}_\mathsf{C}^{-1}\mathbf{S}_2^{\mathsf{CC}}\mathbf{T}_\mathsf{C}\mathbf{S}_1^{\mathsf{CC}}\right)^{-1}\mathbf{S}_2^{\mathsf{CB}}\\
\mathbf{S}^{\mathsf{AA}} &= \mathbf{S}_1^{\mathsf{AA}}+\mathbf{S}_1^{\mathsf{AC}}\mathbf{T}_\mathsf{C}\left(\mathbf{I}-\mathbf{T}_\mathsf{C}^{-1}\mathbf{S}_2^{\mathsf{CC}}\mathbf{T}_\mathsf{C}\mathbf{S}_1^{\mathsf{CC}}\right)^{-1}\mathbf{S}_2^{\mathsf{CC}}\mathbf{T}_\mathsf{C}\mathbf{S}_1^{\mathsf{CA}}\\
\mathbf{S}^{\mathsf{BA}} &= \mathbf{S}_2^{\mathsf{BC}}\mathbf{T}_\mathsf{C}^{-1}\left(\mathbf{I}-\mathbf{T}_\mathsf{C}\mathbf{S}_1^{\mathsf{CC}}\mathbf{T}_\mathsf{C}^{-1}\mathbf{S}_2^{\mathsf{CC}}\right)^{-1}\mathbf{S}_1^{\mathsf{CA}}\\
\mathbf{S}^{\mathsf{BB}} &= \mathbf{S}_2^{\mathsf{BB}}+\mathbf{S}_2^{\mathsf{BC}}\mathbf{T}_\mathsf{C}^{-1}\left(\mathbf{I}-\mathbf{T}_\mathsf{C}\mathbf{S}_1^{\mathsf{CC}}\mathbf{T}_\mathsf{C}^{-1}\mathbf{S}_2^{\mathsf{CC}}\right)^{-1}\mathbf{S}_1^{\mathsf{CC}}\mathbf{T}_\mathsf{C}^{-1}\mathbf{S}_2^{\mathsf{CB}}
\end{aligned}
\tag{256}
$$

Figure 61 shows the scattering coefficients for the three examples. Comparison with the solutions for the same damage but considering an Euler-Bernoulli model is shown.

Figure 61 – Reflection coefficients in a symmetric change of cross-sectional area with finite length. (a)-(b) L=2.4mm; (c)-(d) L=20mm; (e)-(f) L=90mm. (a), (c) and (e) Reflection coefficients; (b), (d) and (f) transmission coefficients. Solid blue line ——— : propagating modes; dotted blue line ····· : Euler-Bernoulli solution. The vertical lines correspond to cut-off frequencies.

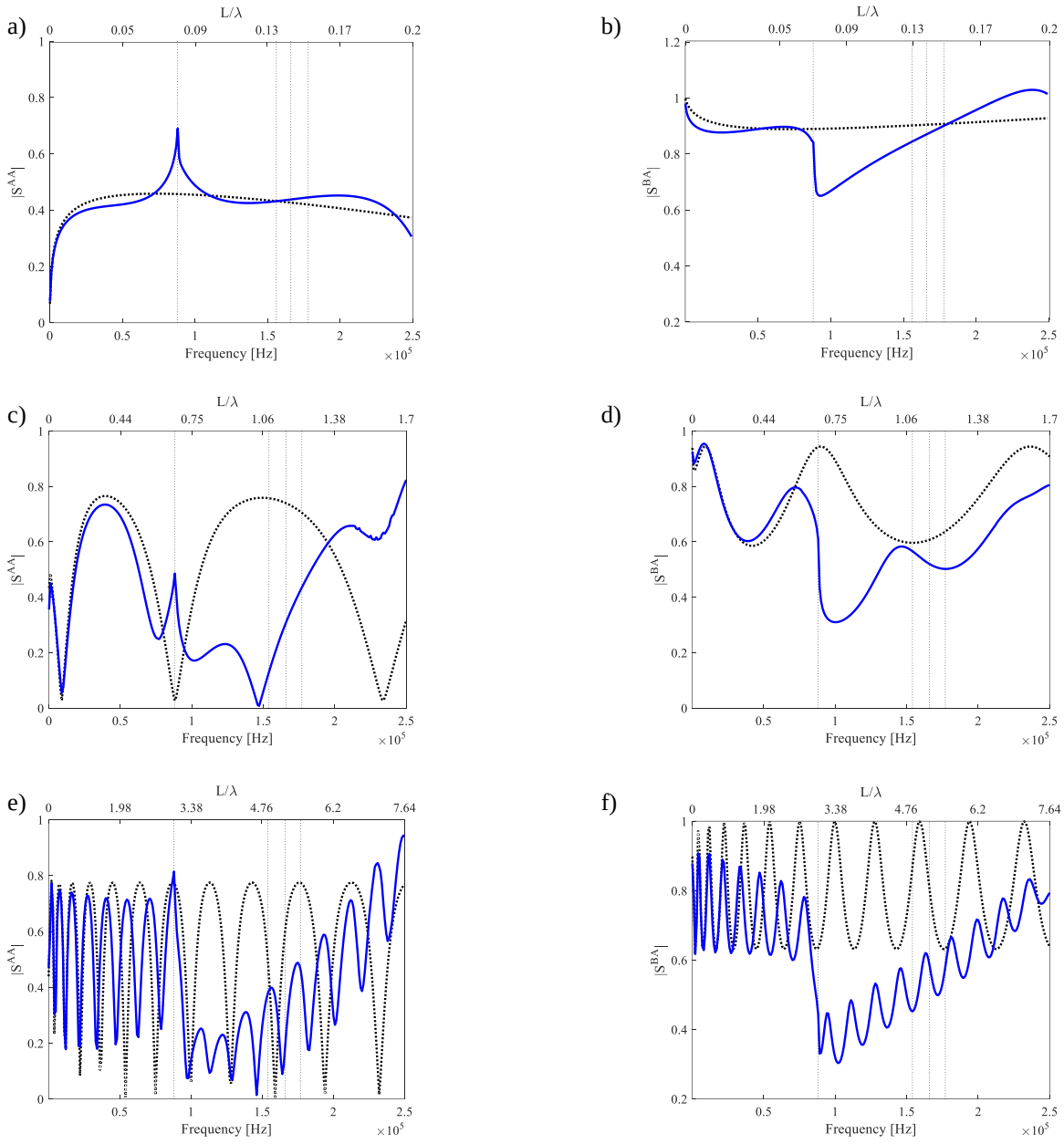

Source: Elaborated by the author

Figure 60 shows that the similarity with the Euler-Bernoulli solution is reduced due to the more complicated mechanism of multiple reflections and transmissions which is affected by the cross-sectional displacements under the passage of the harmonic disturbances. This is due to not only to the higher number of modes propagating at higher frequencies but also to the fact that the second discontinuity also causes the waves in waveguide **C** to reflect, generating

waves that are incident in the first discontinuity from the right side. This does not result in significant differences compared to the previous case for frequencies lower than the first cut-off, as it can be seen in Figure 61. However, at higher frequencies, any mode being incident upon the discontinuity excites all possible modes in the next waveguide. This means that even though only one propagating wave is excited, all possible modes at each frequency can be transmitted (in the second discontinuity) and reflected (in the first discontinuity), and therefore part of the incident energy must be redistributed amongst all modes.

5.3.3.2 Power coefficients

The power coefficients are evaluated using Eq. (254). Figure 62 shows the results for the three cases.

Figure 62 – Power coefficients in a symmetric change of cross-sectional area. a) L=2.4mm; b) L=20mm; c) L=90mm. Solid blue line ——: reflection power coefficient; dashed dot red line – – –: transmission power coefficient; dotted black line ·····: the sum of the power coefficients. The vertical lines correspond to cut-off frequencies.

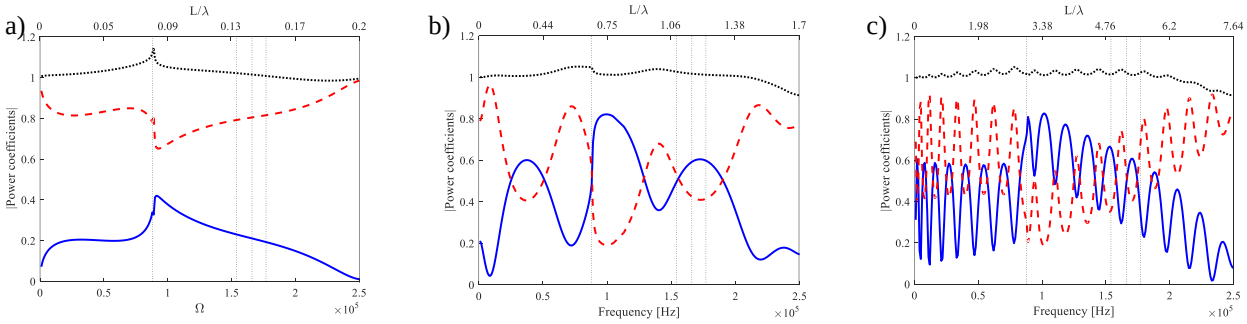

Source: Elaborated by the author

Note that, at very low frequencies and very high frequencies, there is a predominance of the transmitted power, and that there is a frequency range between the first and third cut-off frequencies in which the reflected power becomes bigger than the transmitted power (see Figure 63b and 63c). As already pointed out, the behaviour becomes particularly complicated at the cut-off frequencies, where there are new wavemodes that starts propagating and other modes changing from propagating to non-propagating. This results in significant differences in the power coefficients.

5.3.3.3 Time-averaged kinetic energy

The curves in Figure 63 is obtained using Eq. (255).

Figure 63 – Kinetic energy content in a symmetric change of cross-sectional area with finite length. (a)-(b) L=2.4 mm; (c)-(d) L=20mm; (e)-(f) L=90mm. (a), (c) and (e) Reflection coefficients; (b), (d) and (f) transmission coefficients. Solid blue line ——: kinetic energy in the y-direction; dashed dot red line – – –: kinetic energy in the x-direction. The vertical lines correspond to cut-off frequencies.

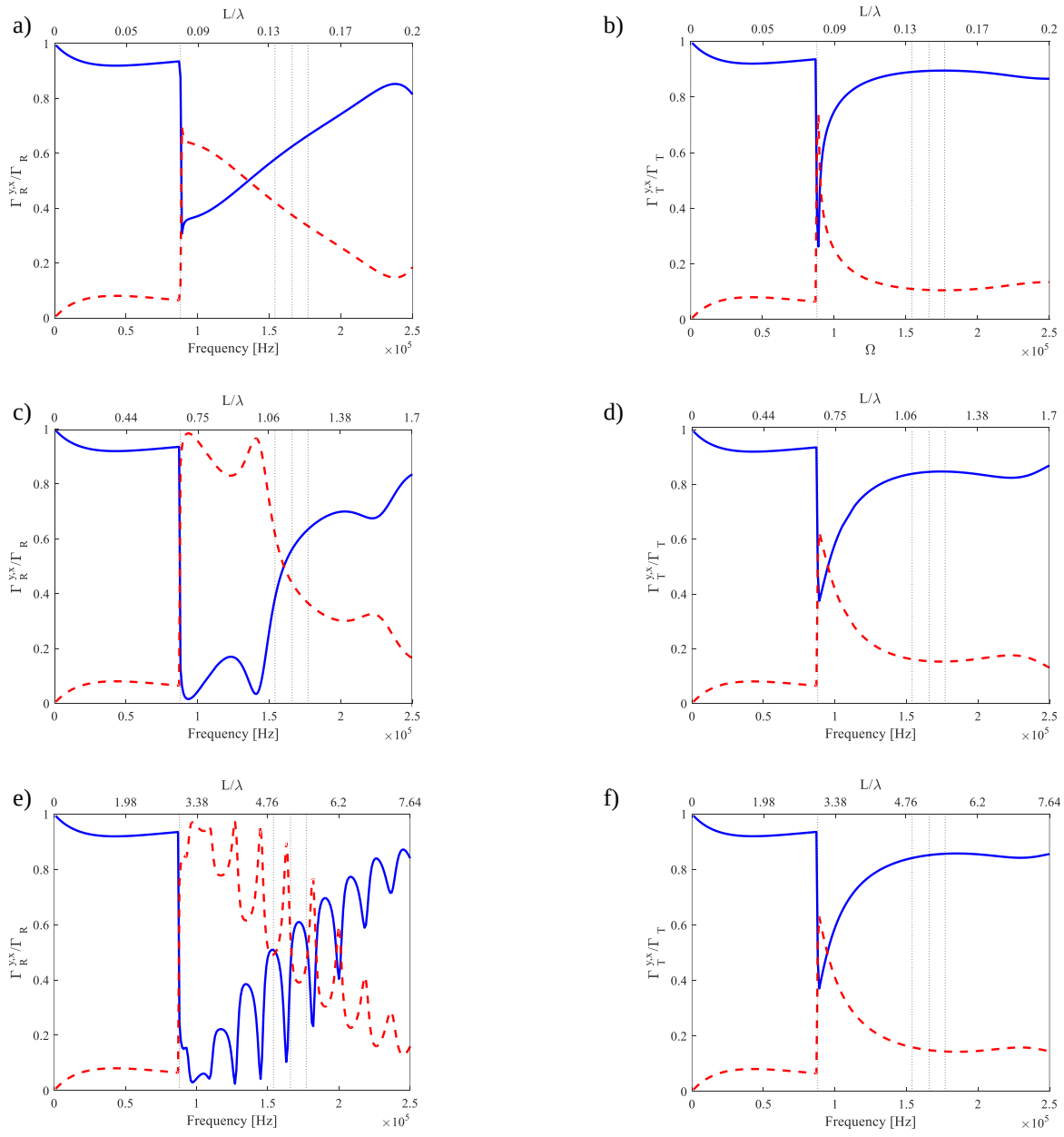

Source: Elaborated by the author

It can be seen from Figures 62 and 63 that the reflected kinetic energy results follow the trend observed in the point discontinuity (Figure 59), however, as the length of the discontinuity gets larger, both energy quantities tend to become more oscillatory. Compared to the previous case, it can be seen that also the transmitted waves are strongly affected by the cut-off of the first antisymmetric Lamb mode, which now can propagate after the discontinuity due to the

characteristics of the damaged waveguide. At low frequencies, the reflected and transmitted time-averaged kinetic energy components retain the same characteristics as the incident wave since, at this frequency range, there are no wavemodes cutting on and the symmetry of the discontinuity do not affect the incident wavemode in terms of mode conversion.

5.3.4 Conclusions

In this section, a symmetric change of cross-sectional area was considered. Compared to the cases studied in the previous chapters, the results were here obtained applying the WFE method to a small segment of the waveguides discretized using a stack of plane elements meshed through the cross-section. This allowed a wave characterization up to high frequency, including cut-off of higher order Lamb modes, nearfield and attenuated modes. The latter two are important in scattering problems since they take part in the energy redistribution due to wave interaction with the discontinuities. Comparison with analytical solutions obtained for an Euler-Bernoulli beam model showed again good agreement at low frequency.

Several numerical cases were considered and the changes in the scattering coefficients and the energy quantities due to the variation of the length of the damage were shown and discussed.

5.4 SCATTERING: NON-SYMMETRIC CHANGE OF AREA

5.4.1 Introduction

In this section, the scattering coefficients, power coefficients and time-averaged kinetic energies are numerically calculated for a non-symmetric change of cross-sectional area.

5.4.2 Point discontinuity

Figure 64 shows a schematic representation of the WFE discretization of a non-symmetric change of cross-sectional area (step discontinuity).

Figure 64 – FE model using plane elements of a single non-symmetric change of cross-sectional area.

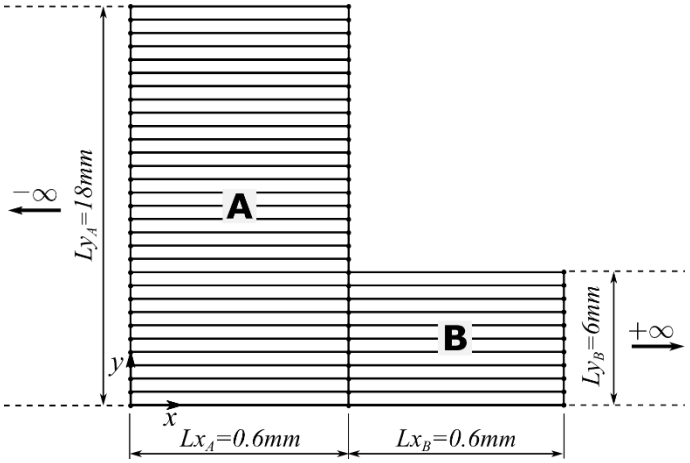

Source: Elaborated by the author

Equation (252) is used to model the boundary conditions. Compared to the symmetric case, the vectors $\mathbf{m}_{\mathsf{A}}$ and $\mathbf{m}_{\mathsf{B}}$ that define the connected degrees of freedom between **A** and **B** are different since here, the first 22 DOF of **A** are connected to all DOF in the left side of **B**. This can be written in a generic way as

$$\begin{aligned}\mathbf{m}_{\mathsf{A}} &= \left[1, 2, \cdots, \frac{n_{\mathsf{B}}}{2}\right] \\ \mathbf{m}_{\mathsf{B}} &= \left[1, 2, \cdots, \frac{n_{\mathsf{B}}}{2}\right]\end{aligned} \tag{257}$$

One of the primary effects of non-symmetric discontinuities is the wavemode conversion. In order to show this mechanism in a simple way, Figure 65 shows a schematic diagram of equilibrium of forces at low frequency. As an example, in Figure 65a a pure axial (longitudinal) force is incident upon the discontinuity. When the force (or the longitudinal wave) is considered at the discontinuity (Figure 65b), part of this force is incident longitudinally at waveguide **B** ($\vec{F}_{A1}$) but another part of that force which is not in direct contact with waveguide **B** ($\vec{F}_{A2}$) becomes a moment since it is applied at a distance L_n from the neutral axis of **B**. This causes the waves at **B** to be no longer purely axial, but a combination of axial and transverse waves, which shows in a simple way one of the mechanism of wavemode conversion.

Figure 65 – Diagram of forces in the non-symmetric discontinuity. a) Incident force; b) equilibrium at the discontinuity.

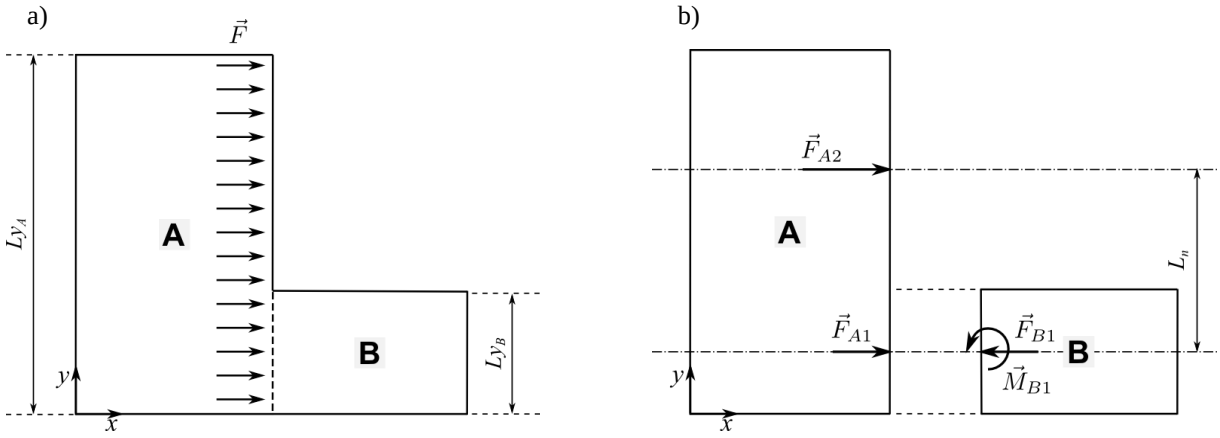

Source: Elaborated by the author

5.4.2.1 Scattering coefficients

Figure 66 shows the scattering coefficients. These are evaluated using Eq. (31).

Figure 66 – Reflection coefficients in a non-symmetric change of cross-sectional area. a) Reflection coefficients; b) transmission coefficients. Solid blue line ——— : propagating modes; dashed dot red line — · - : nearfield modes. The numbers relate to different wave modes, and the vertical lines correspond to cut-off frequencies.

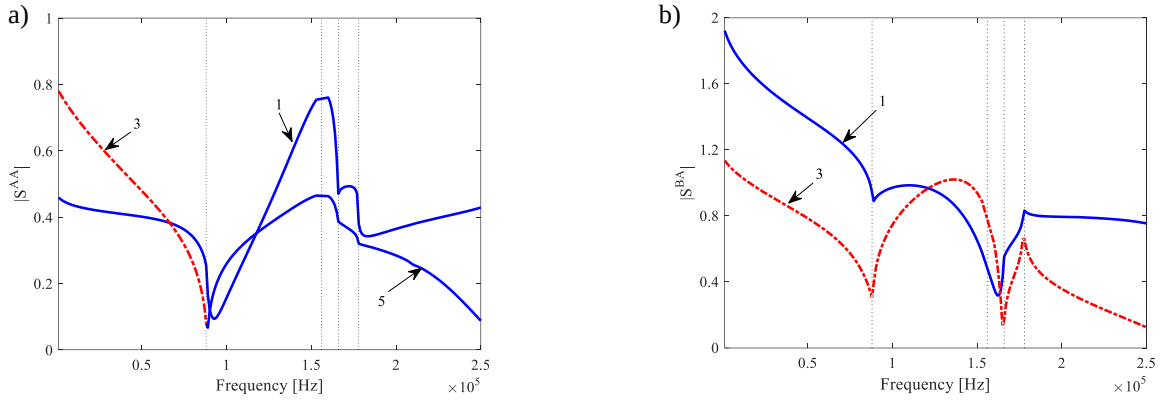

Source: Elaborated by the author

It can be seen that, compared to the symmetric case, the scattering behaviour is more complicated, in particular at higher frequencies due to higher-order wavemodes and complicated mode conversion. Changes in the scattering behaviour are particularly significant at the cut-off frequencies.

5.4.2.2 Power coefficients

Equation (254) was used for evaluating the power coefficients represented in Figure 67. The figure shows the results for both reflection and transmission power coefficients.

Figure 67 – Power coefficients in a non-symmetric change of cross-sectional area. Solid blue line ——: reflection power coefficient; dashed dot red line – – –: transmission power coefficient.

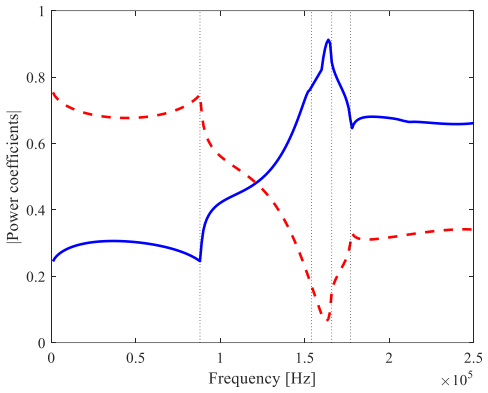

Source: Elaborated by the author

At low frequency, most of the energy flow is transmitted and no significant changes compared to the case of the symmetric change of cross-sectional area can be noticed. However, above the first cut-off frequency, the reflected power coefficient increases and becomes bigger than the transmission power coefficient showing a drastic change in the behaviour. This clearly shows the effect of mode conversion and indicates that a step-down non-symmetric discontinuity can be characterized by a magnitude of the reflected power higher than those of the transmitted. At higher frequency, the reflected energy flow remains higher than those transmitted.

5.4.2.3 Time-averaged kinetic energy

The time-averaged kinetic energy is calculated using Eq. (255), and the results are shown in Figure 68.

Figure 68 – Kinetic energy content in a non-symmetric change of cross-sectional area. a) Reflected time-averaged kinetic energy; b) transmitted time-averaged kinetic energy. Solid blue line ——— : kinetic energy in the *y*-direction; dashed dot red line — · - · - : kinetic energy in the *x*-direction. The vertical lines correspond to cut-off frequencies.

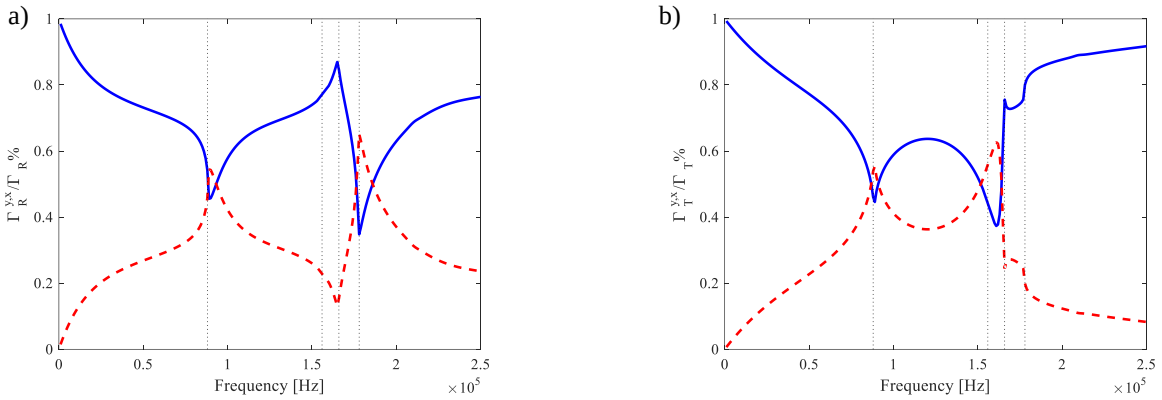

Source: Elaborated by the author

Figure 68 shows that, at low frequency and high frequency, most of the reflected and transmitted kinetic energies are in the *y*-direction, indicating the predominance of transverse modes. This directional component shows a minimum at the first cut-off frequency; after this minimum, it increases and then decreases again, showing a new minimum close to the higher cut-off frequency, where the percentage of the component in the *y*-direction is around 40% compared to those in the *x*-direction that is 60%. For higher frequency, greater than 75% of the transmitted and reflected kinetic energy becomes again the *y*-direction. The reflected kinetic energy shows some similarities to those of the symmetric case as in Figure 59, although the behaviour is more complicated at higher frequencies due to mode conversion caused by the non-symmetry of the discontinuity.

5.4.3 Finite length discontinuity

Scattering from a non-symmetric finite length discontinuity is presented. These can be seen as a notch in a beam or plate The three lengths of discontinuity used in the previous section were considered and the results are compared to the symmetric case investigated in the previous section. Figure 69 shows the schematic representation of the WFE model of the discontinuity studied.

Figure 69 – FE model using plane elements of two consecutive non-symmetric changes of cross-sectional area.

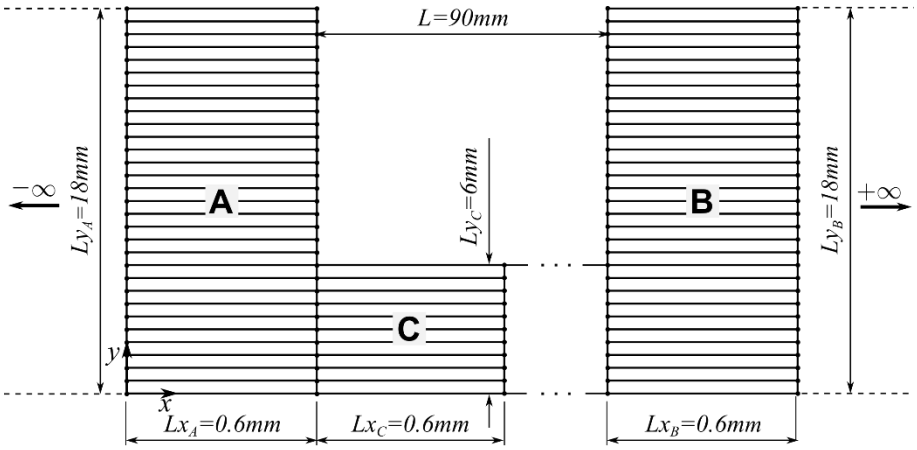

Source: Elaborated by the author

5.4.3.1 Scattering coefficients

Figure 70 shows the scattering coefficients for the finite length discontinuities with L=2.4 mm, L=20mm and L=90mm.

Figure 70 – Reflection coefficients in a non-symmetric change of cross-sectional area with finite length. (a)-(b) *L*=2.4 mm; (c)-(d) *L*=20mm; (e)-(f) *L*=90mm. (a), (c) and (e) Reflection coefficients; (b), (d) and (f) transmission coefficients. The vertical lines correspond to cut-off frequencies.

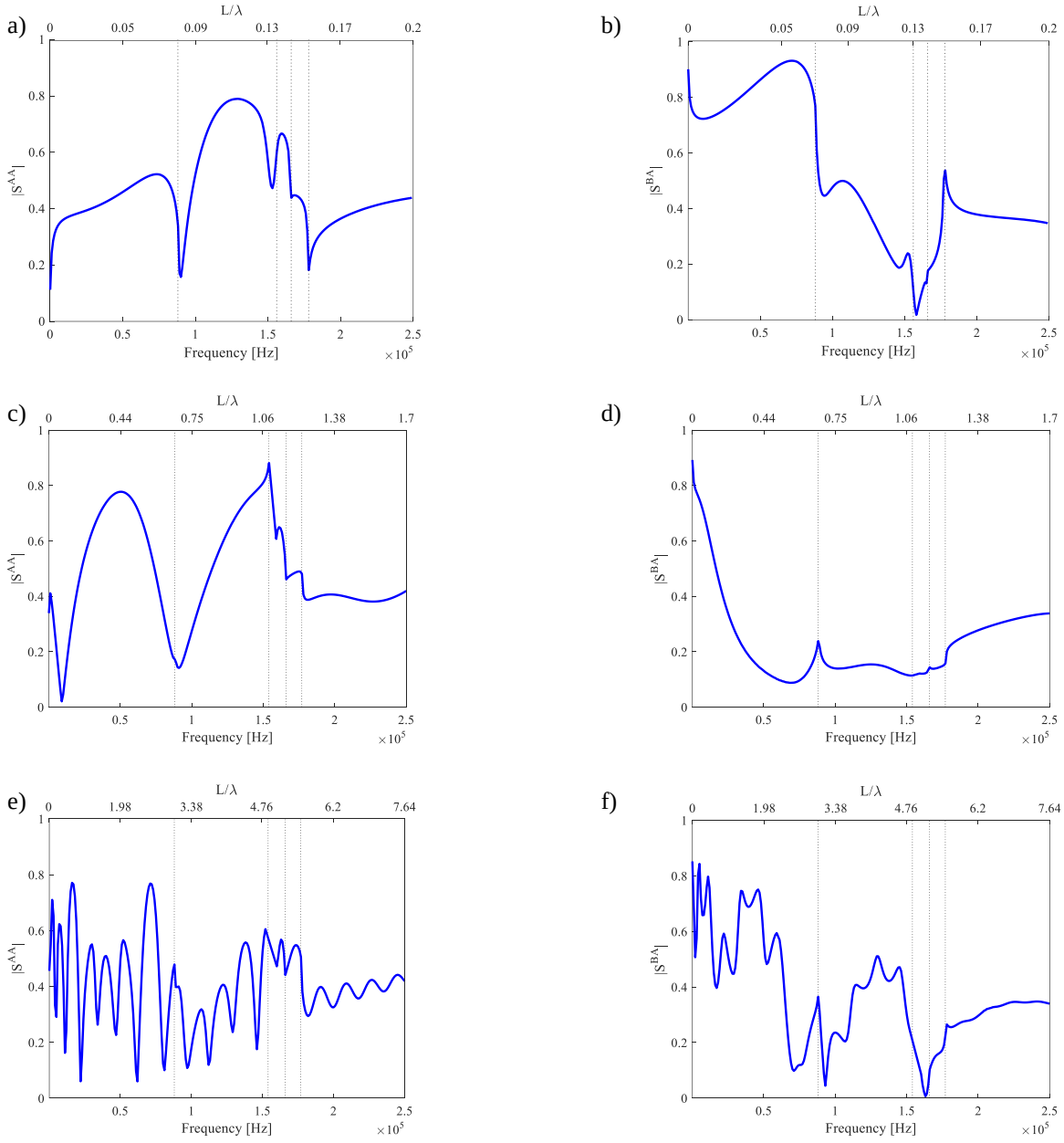

Source: Elaborated by the author

It can be seen that for *L*=2.4mm the reflected and transmitted coefficients show a more complicated behaviour due to the non-symmetry of the change of area and mode conversion. In particular, compared to the previous case in Figure 61a and 61b, significant changes occur at the cut-off frequencies. As the length of the discontinuity gets longer, the differences hold, showing the different mechanism of reflection and transmission compared to the symmetric

case. Again, it can be seen that the scattering behaviour changes close to the cut-off frequencies due to the energy redistribution amongst higher order modes and the mode conversion.

5.4.3.2 Power coefficients

Figure 71 shows the power coefficients calculated using Eq. (254).

Figure 71 – Power coefficients in a non-symmetric change of cross-sectional area. a) L=0.6mm; b) L=20mm; c) L=90mm. Solid blue line ——— : reflection power coefficient; dashed dot red line – – – : transmission power coefficient. The vertical lines correspond to cut-off frequencies.

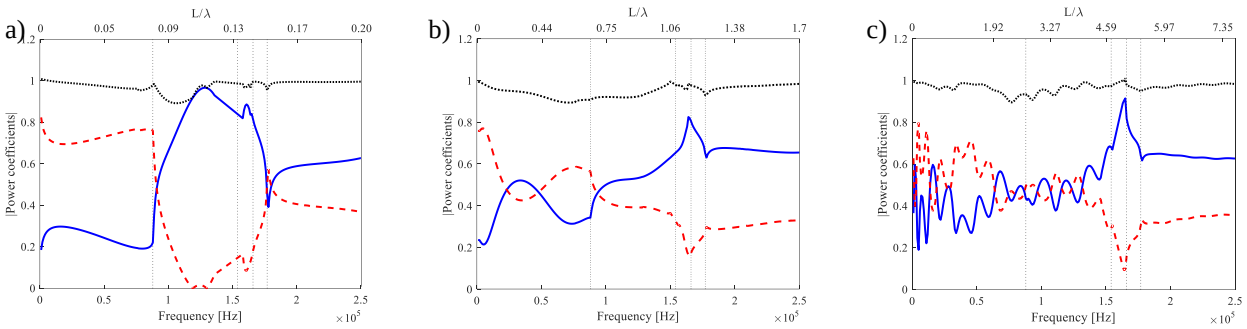

Source: Elaborated by the author

It can be seen that the finite length discontinuity tends to follow, to some extent, the behaviour of the point discontinuity shown in Figure 67. In Figure 71b it can be seen that at 23kHz and 94kHz the reflected power coefficients gets bigger than the transmitted power coefficients, while in Figure 71c this behaviour occurs more frequently with more local maxima and minima. This "conversion of power" is somehow related to the length of the discontinuity and it could be further investigated to give an approximate estimation of the length of the damage. As a general observation, it was found that the numerical model in the frequency range between the first and the second cut-off frequencies is more prone to numerical errors.

5.4.3.3 Time-averaged kinetic energy

Figure 72 shows the time-averaged kinetic energy for the three cases calculated using Eq. (255).

Figure 72 – Kinetic energy content in a non-symmetric change of cross-sectional area with finite length. (a)-(b) L=2.4mm; (c)-(d) L=20mm; (e)-(f) L=90mm. (a), (c) and (e) Reflection coefficients; (b), (d) and (f) transmission coefficients. Solid blue line ——: kinetic energy in the y direction; dashed dot red line – – –: kinetic energy in the x direction. The vertical lines correspond to cut-off frequencies.

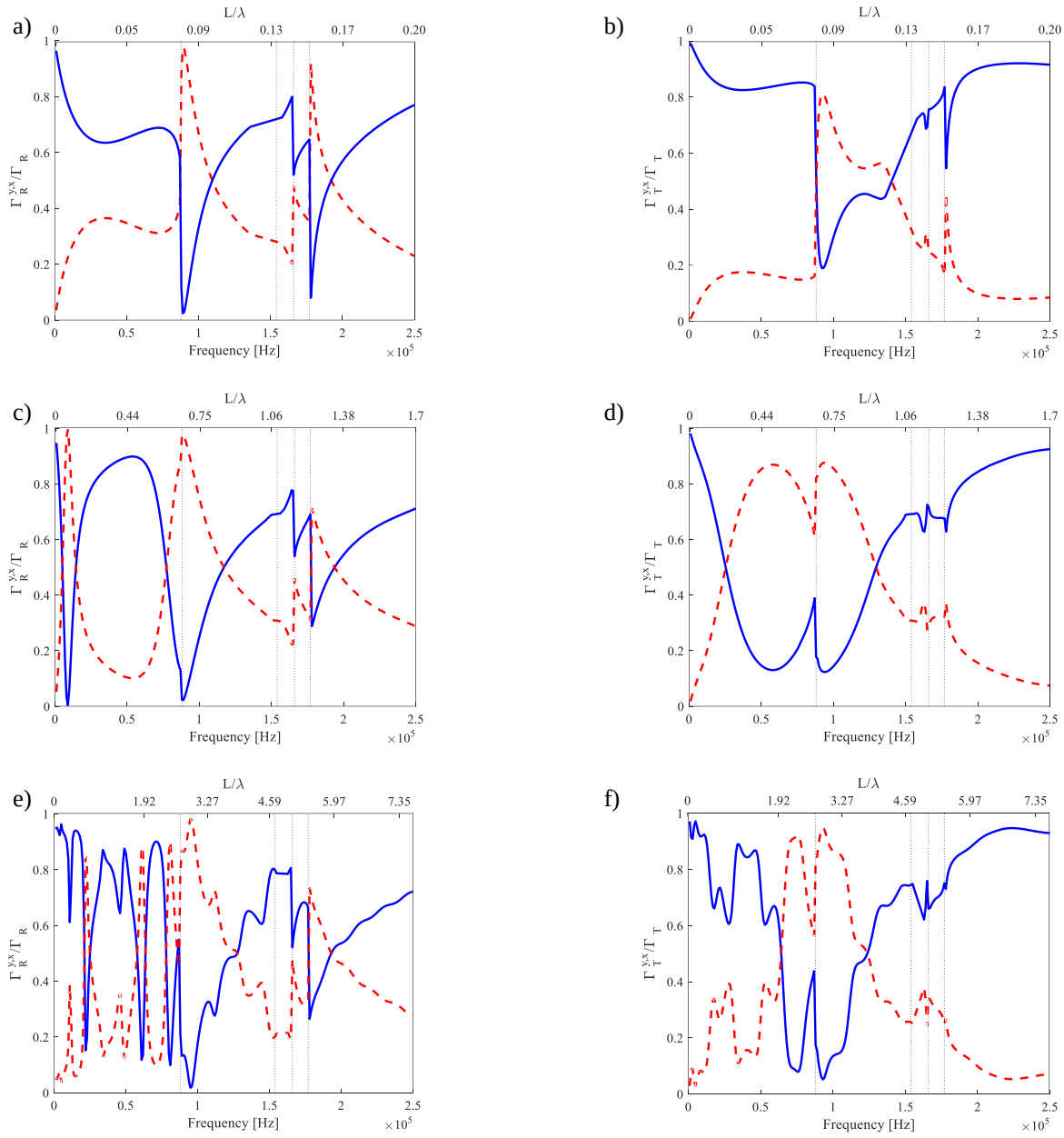

Source: Elaborated by the author

Again, only propagating modes are considered in order to simulate a far-field condition. Compared to the symmetric case, in the non-symmetric thickness variation, mode conversion can be seen in all the three cases looking at the directional components of the kinetic energy. This can be seen even in the case of the smallest discontinuity (L=2.4mm). In all cases, at higher

frequencies, the component of the kinetic energy in the *y*-direction gets bigger than those in the *x*-direction.

5.4.4 Influence of the type of the incident wave

When evaluating the structural integrity of a system, it can be of interest to determine which incident wavemode is better to evaluate the health condition of a given structure. Typically, the A_0 and the S_0 Lamb modes are used as excited waves in ND techniques for SHM applications although it is very difficult to excite a pure single mode in practical applications. These fundamental Lamb modes correspond to waves associated with branches 1 and 2 in the dispersion curves shown in Figure 53. In this section, wave scattering is investigated considering a pure incident symmetric S_0 Lamb mode and an incident antisymmetric A_0 Lamb mode. The non-symmetric case with L=20mm was assumed in the following.

Figure 73 – Comparison of the energy quantities when applying an A_0 or S_0 incident wave for the non-symmetric discontinuity with L=20mm. (a), (c), (e) and (g): Incident A_0 Lamb mode; (b), (d), (f) and (h): incident S_0 Lamb mode. (a)-(b) power coefficients. Solid blue line ——: reflection power coefficients – – –: transmission power coefficients; (c)-(d) Incident time-averaged kinetic energy; (e)-(f) reflection time-averaged kinetic energy; (g)-(h) transmission time-averaged kinetic energy. Solid blue line ——: kinetic energy in the y-direction; dashed dot red line – – –: kinetic energy in the x-direction. The vertical lines correspond to cut-off frequencies.

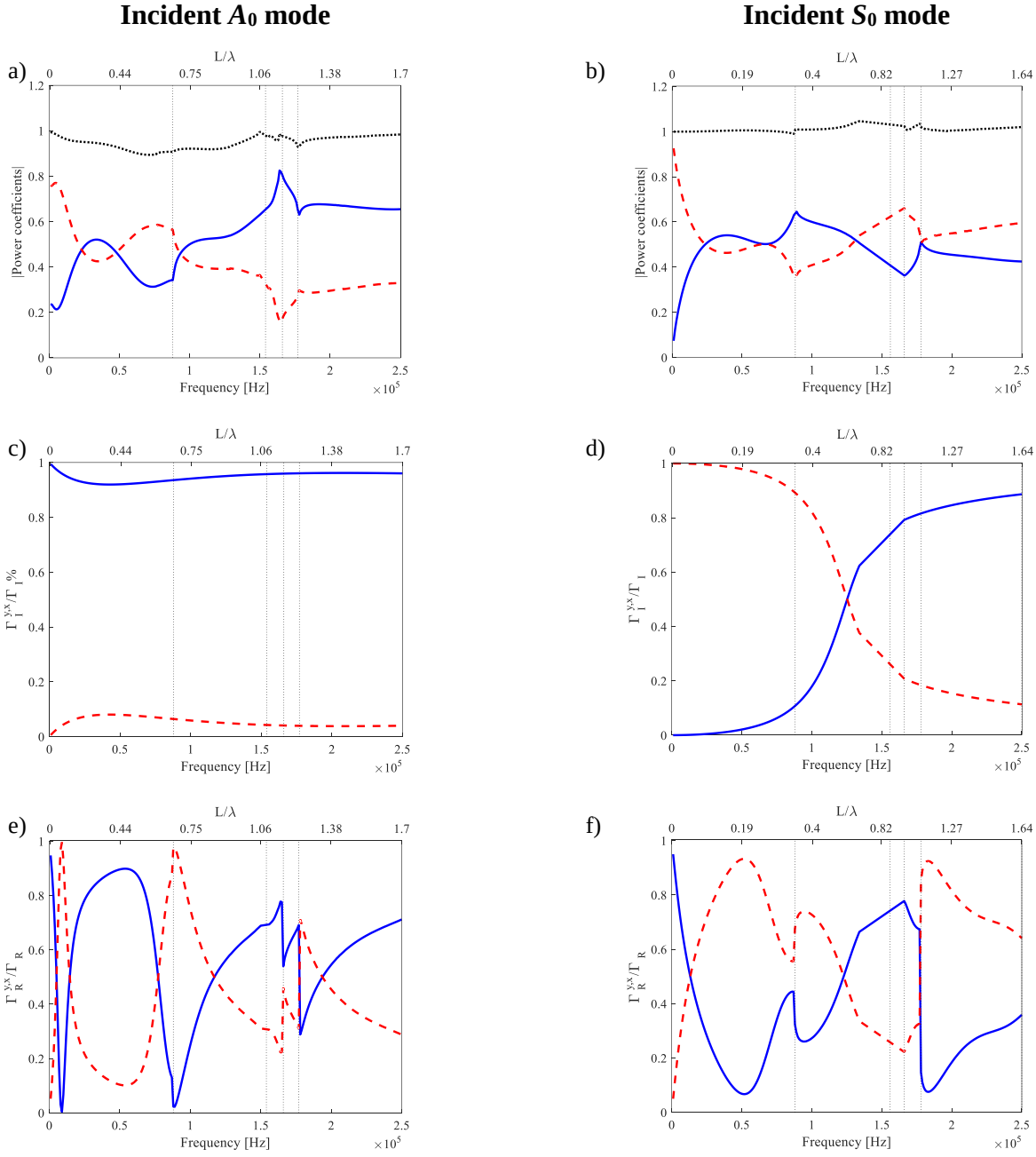

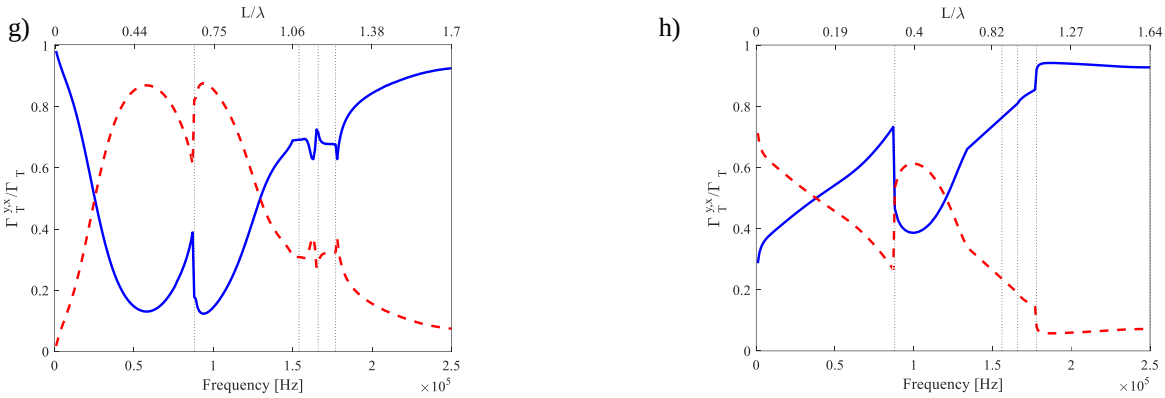

Source: Elaborated by the author

In general, both kinds of incident waves can be used for damage detection purposes, however, some of them might be better suited depending on the situation. It can be seen that for the power coefficients (Figure 73b), the S_0 incident case shows the same amount of energy going to the reflected and transmitted waves. This can show that, for a wide range of frequency, both reflected and transmitted waves can be measured and used for damage evaluation. On the other hand, the A_0 case (Figure 73a) shows that at higher frequencies, the reflected energy is larger, which means that it could be easier to identify the damage using the reflected waves. Considering the directional components of the kinetic energies, both cases present high complexity in the reflected and transmitted waves, meaning that both can represent the wave mode conversion caused by the non-symmetric damage. However, for the S_0 incident mode, at higher frequencies, the incident wave can no longer be considered as a pure longitudinal (as seen in Figure 73d), due to a change in the nature of the S_0 mode. As shown in Figure 52, around the frequency of 125kHz, branch 2, which corresponds to the S_0, start to deviate from the behaviour of a pure axial wave. At higher frequencies, the wavelength becomes comparable to the thickness of the beam, causing the displacement in the *y*-direction to increase. This causes the wavemode to change from symmetric mode with most of the kinetic energy in the *x*-direction to a mode with most of the kinetic energy in the *y*-direction (Figure 73d). It can be seen that the transmitted kinetic energy in Figure 73h follows the same kinetic energy profile observed in Figure 73d, where at low frequencies there is a predominance of kinetic energy in the *x*-direction while at higher frequencies, there is a predominance in the *y*-direction. The reflected kinetic energy in Figure 73f shows an opposite behaviour: at low frequencies, there is a predominance of kinetic energy in the *y*-direction and at high frequencies, there is a predominance in the *x*-direction, which indicates wave mode conversion due to damage and not due to the increase in the frequency.

5.4.5 Influence of the severity of the damage

In this section, a brief introduction to the effects due to an increase in the damage depth is given. This is of importance in damage detection since it can help in evaluating the severity of a damage, so that, when a damage reaches critical condition, the system can be stopped before catastrophic failure occurs. In this study, the severity of the damage was simulated by considering different percentages of damage in waveguide **C**, Figure 69. These percentages correspond to the thicknesses of waveguide **C**: 14.4, 10.8, 7.2 and 3.6mm, over the thickness of the undamaged waveguide (waveguide **A** and **B**, Figure 69), which is 18mm thick.

The evaluated scattering quantity, in this case, is the time-averaged kinetic energy in the *y*-direction. The time-averaged kinetic energy in the *x*-direction is not here shown since it can be easily recovered from those of the time-averaged kinetic energy in the *y*-direction, viz, the sum of the two is equal to one, or equally 100%. The results showed that this quantity is a helpful quantity to investigate the nature of the scattering. The A_0 Lamb mode (branch 1 in Figure 53) is assumed as the incident wave.

Figure 74 – Time-averaged kinetic energy for different damage severity. a) Reflected kinetic energy; b) Transmitted kinetic energy. Solid blue line ——— : waveguide **C** with 3.6mm; dashed red line – – – : **C** with 7.2mm; dash-dot green line — · — : **C** with 10.8mm; dotted brown line ····· : **C** with 14.4mm. The vertical lines correspond to cut-off frequencies of waveguide **A**.

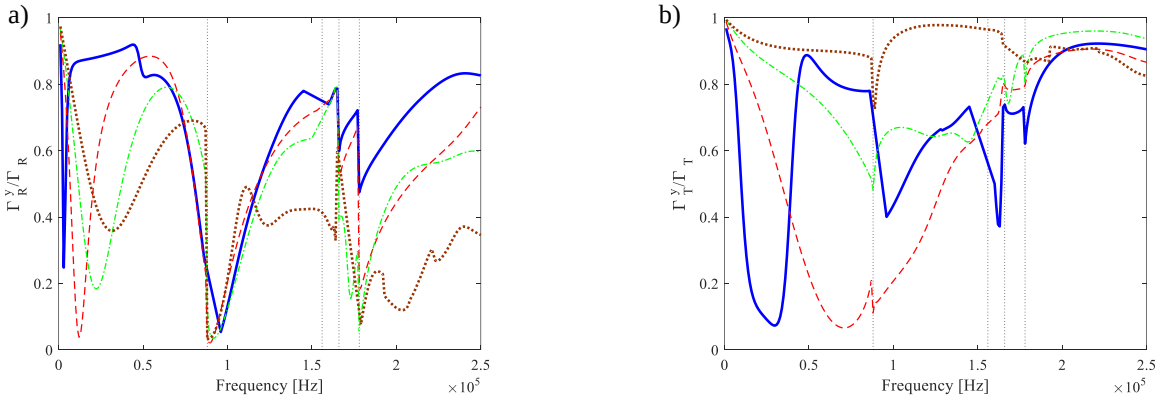

Source: Elaborated by the author

Figure 74 shows that the scattering behaviour becomes more complicated as the level of damage increases due to the increase of the mode conversion. Some general observations can be made with respect to the damage severity, in particular below the first cut-off frequency. At low frequency, in fact, it can be seen for example that the component in the y-direction shows a minimum value which becomes lower in magnitude as the severity increases. This is shown better in Figure 75. Also in Figure 75, the frequency in which the minimum occurs

decreases with the increase of the severity. In both Figures 74(a) and (b), it can be noted similar situations where a clear progression in minima and maxima between the most severe and the smallest damage is observed.

Figure 75 – Zoom of Figure 74, reflected time-averaged kinetic energy for different damage severity below the first cut-off frequency. Solid blue line ——— : waveguide **C** with 3.6mm; dashed red line – – – : **C** with 7.2mm; dash-dot green line —·—: **C** with 10.8mm; dotted brown line ····· : **C** with 14.4mm.

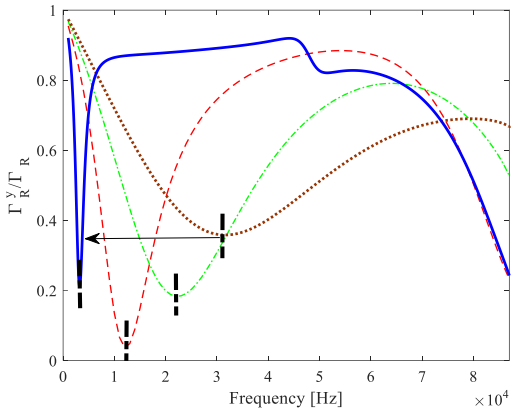

Source: Elaborated by the author

5.4.6 Conclusions

In this section, the effect of a non-symmetric change of cross-sectional area was studied. The discontinuity (damage) was investigated following the procedure presented for the symmetric discontinuity. Results were discussed and compared with those obtained in the symmetric case. It was shown that the non-symmetric discontinuity causes the scattering coefficients to behave in a very different way with respect to the symmetric damage due to the phenomenon of wavemode conversion. The power coefficients showed that the energy flow tends to go to the reflected power coefficient instead of transmitted power coefficient as it was found for the non-symmetric case. The time-averaged kinetic energy, it tends to concentrate in the *y*-direction, as opposed to what was found in the symmetric case. These findings showed that the power coefficients and time-averaged kinetic energies can be used to detect the non-symmetry of the damage. By analyzing the changes in the behaviour of these quantities, it is also possible to estimate the length of the damage to some extent. The influence of the incident wavemode and the effects of the increase in the severity of the damage were also investigated.

5.5 CONCLUSIONS

In this chapter, the modelling of a 1D waveguide using 2D plane element was presented and the WFE model was used to evaluate the scattering coefficients, power coefficients and the time-averaged kinetic energy distribution. Both the symmetric and non-symmetric discontinuities were considered.

Initially, the WFE results for the dispersion curves from 0 to 250kHz of the two types of waveguides were presented, showing the differences at high frequency with those typically obtained using simple analytical models such as the Euler-Bernoulli beam.

It was shown that the WFE solution for the scattering coefficient agreed well with the analytical solution at low frequency, where the latter can give enough accurate results. Validation of the results was also performed considering the conservation of energy: the sum of the reflected and transmitted energy must be equal to incident energy flow. This corresponds to a minimum error in the difference between the sum of the power coefficients and one. The case of finite length discontinuity was also investigated and three different lengths of discontinuity were considered.

The problem of the non-symmetric change of cross-sectional area was presented. As in the symmetric case, the point discontinuity and finite length discontinuity were studied. It was shown that the scattering coefficients are different from the symmetric case due to the mode conversion caused by the loss of symmetry of the change of area with respect to the neutral axis of the waveguide. As a general observation, it was found that the reflected power is generally higher than the transmitted power, showing that this kind of discontinuity diminishes the passage (or transmission) of the excited wave. It was shown that the kinetic energy tends to be higher in the y-direction, while in the symmetric case the energy is predominant in the x-direction.

The last two sections of the chapter focused on the evaluation of some cases which can be of interest when using wave propagation for damage detection purposes. In particular, the scattering when the fundamental symmetric and antisymmetric Lamb modes are excited was investigated. Comparison of the results for the directional components of the time-averaged kinetic energy for different depth of the change of area was evaluated. It was found that the component of the reflected and transmitted kinetic energy can be a useful quantity for evaluating the damage severity.

The results shown in this chapter showed that the proposed methodology can give useful information at low computational cost for practical ND testing in SHM applications.

6 CONCLUSIONS

In this thesis, a numerical model to predict the wave scattering in one-dimensional waveguides with different kinds of discontinuities using the Finite Element method was studied. Particular focus was given to the reduction of cross-sectional area as means to represent loss of material in the surface of a 1D waveguide. The scattering problem was modelled following these steps: prediction of the dispersion curves and wavemodes using the Wave and Finite Element method; nodal displacements and nodal forces of the FE model were approximated using these wavemodes as a basis; the undamaged and damaged part of the waveguides were coupled using equilibrium and continuity conditions. This resulted in the formulation of the frequency dependent scattering matrix in terms of wavemodes. The approach, exploiting standard FE discretization of small segments of the waveguide, can be applied to waveguides with complicated cross-section and up to very high frequency at low computational cost.

In Chapter 2, the Wave and Finite Element method was introduced and the method for obtaining the scattering matrix was described. In this chapter, some numerical issues were also discussed and energy quantities were introduced.

In Chapter 3, the analytical models for rods and beams were studied, and simple scattering examples such as rods and beams with single (point) spring type discontinuities and a symmetric change of cross-sectional area were studied. The last case was also studied considering two consecutive change of area, which can be used, for example, to represent a damage with a finite length due corrosion.

In Chapter 4, the same examples studied in Chapter 3 were studied using the WFE method and the results were compared with those obtained using the analytical approach. The aim of this chapter is to validate the numerical model since the examples in Chapter 3 are already well known and the solution for then can be found in the literature. The WFE model for modelling wave scattering was validated and ready to be applied to more complicated cases, which better represent real cases of damaged waveguides.

In Chapter 5, wave propagation in a one-dimensional waveguide was modelled using a more refined WFE and the region around the damage was discretized using a stack of 2D FE plane element meshed through the cross-section. These plane elements are standard FE plane elements, defined by four nodes, each node having two degrees of freedom. Symmetric and asymmetric change of area in the waveguides, such as step-discontinuities and notches were investigated. It was shown that due to the higher complexity of the WFE model as compared to the Euler-Bernoulli beam model, the WFE model was able to describe a much richer wave

behaviour, resulting in a more accurate description of the wave scattering. In particular, the model allowed a prediction of the wave scattering up to high frequency including higher order wave modes and therefore mode conversion in the case of an asymmetric discontinuity. Results were shown in terms of scattering coefficients, power coefficients and time-averaged kinetic energy. An investigation into the directional components of the time-averaged kinetic energy showed that kinetic energy can be used to model the wave scattering and to evaluate the effects of mode conversion due to an asymmetric damage.

Results showed that the methodology proposed can be useful in modelling wave scattering up to high frequency and at low computational cost. Some general conclusions and considerations are here listed:

- prediction of the dispersion curves is fundamental in wave scattering problems. In particular cut-off frequency and higher order mode cut-off showed to have a very significant effect on the reflected and transmitted waves;
- choosing the number of wavemodes as a basis for describing the "physical" displacements and internal forces is not a trivial task, in particular at high-frequency. In the present work, all the propagating modes were considered according to the frequency range, and evanescent and complex modes were introduced according to a minimum of the difference between the incident energy and the scattered energy (the discontinuity is conservative and therefore conservation of energy must hold);
- the directional components of the time-averaged kinetic energy were found to be useful quantities for studying the scattering behaviour, in particular when mode conversion occurs due to non-symmetric change of the cross-sectional area.

Current and future works concern:

- improvement in the wave mode selection method using automated procedures, which would reduce numerical errors, and implementation in the procedure of a Wave Assurance Criterion in order to numerically track the wavemodes and the wavenumbers in an automated way;
- modelling the effect of external absorbing media in order to simulate situations in which the damaged waveguide is buried or surrounded by water;
- modelling the wave scattering in time-domain in order to simulate experimental results.

REFERENCES

ABDEL-RAHMAN, A. Y. A. **Matrix analysis of wave propagation in periodic systems**. 272 f. Thesis (PhD)- Institute of Sound and Vibration Research, University of Southampton, Southampton. 1979.

ALLEYNE, D. N.; CAWLEY, P. The excitation of Lamb waves in pipes using dry-coupled piezoelectric transducers. **Journal of Nondestructive Evaluation,** New York**,** v. 15, n. 1, p. 11-20, 1996.

ALLEYNE, D. N.; LOWE, M. J. S.; CAWLEY, P. The reflection of guided waves from circumferential notches in pipes. **Journal of Applied Mechanics**, New York**,** v. 65, n. 3, p. 635-641, 1998.

ALMEIDA, F. C. L. et al. On the acoustic filtering of the pipe and sensor in a buried plastic water pipe and its effect on leak detection: an experimental investigation. **Sensors,** Basel**,** v. 14, n. 3, p. 5595-5610, 2014.

ATASHIPOUR, S. A. et al. An effective damage identification approach in thick steel beams based on guided ultrasonic waves for structural health monitoring applications. **Journal of Intelligent Material Systems and Structures,** Lancaster**,** v. 24, n. 5, p. 584-597, 2013.

AULD, B. A. **Acoustic fields and waves in solids**. New York: Wiley, 1973. 423 p.

AYALA CASTILLO, P. C.; LOPES JUNIOR, V.; BRENNAN, M. J. **Detecção de danos em estruturas guiadas usando ondas de alta frequência**. 2015. 83 f. Dissertation (Master)- Faculdade de Engenharia, Universidade Estadual Paulista "Julio de Mesquita Filho"- UNESP, Ilha Solteira. 2015.

BANERJEE, J. R. Dynamic stiffness formulation for structural elements: a general approach. **Computers & Structures,** Elmsford**,** v. 63, n. 1, p. 101-103, 1997.

BARSHINGER, J. N.; ROSE, J. L. Guided wave propagation in an elastic hollow cylinder coated with a viscoelastic material. **IEEE Transactions on Ultrasonics, Ferroelectrics, and Frequency Control,** New York**,** v. 51, n. 11, p. 1547-1556, 2004.

BENMEDDOUR, F. et al. Study of the fundamental Lamb modes interaction with asymmetrical discontinuities. **NDT & E International,** London**,** v. 41, n. 5, p. 330-340, 2008.

BOLLER, C.; STASZEWSKI, W. J. Aircraft structural health and usage monitoring. In: STASZEWSKI, W. J.;BOLLER, C. *et al.* (Ed.). **Health monitoring of aerospace structures: smat sensor technologies and signal processing**. West Sussex: John Wiley & Sons, 2004. p.29-73. ISBN 9780470092866.

BRENNAN, M. J.; ELLIOTT, S. J.; PINNINGTON, R. J. The dynamic coupling between piezoceramic actuators and a beam. **The Journal of the Acoustical Society of America,** Melville**,** v. 102, n. 4, p. 1931-1942, 1997.

BRIGHAM, J. C. et al. A spectral finite element approach to modeling soft solids excited with high-frequency harmonic loads. **Computer Methods in Applied Mechanics and Engineering,** Amsterdam**,** v. 200, n. 5, p. 692-698, 2011.

BRILLOUIN, L. **Wave propagation in periodic structures: electric filters and crystal lattices**. New York: Dover Publications, 1953. 255 p.

CHO, Y.; HONGERHOLT, D. D.; ROSE, J. L. Lamb wave scattering analysis for reflector characterization. **IEEE Transactions on Ultrasonics, Ferroelectrics, and Frequency Control,** New York**,** v. 44, n. 1, p. 44-52, 1997.

CHO, Y.; ROSE, J. L. A boundary element solution for a mode conversion study on the edge reflection of Lamb waves. **The Journal of the Acoustical Society of America,** Melville**,** v. 99, n. 4, p. 2097-2109, 1996.

DEMMA, A. et al. The reflection of guided waves from notches in pipes: a guide for interpreting corrosion measurements. **NDT & E International,** London**,** v. 37, n. 3, p. 167-180, 2004.

DUAN, W.; KIRBY, R. A numerical model for the scattering of elastic waves from a non-axisymmetric defect in a pipe. **Finite Elements in Analysis and Design,** Amsterdam**,** v. 100, p. 28-40, 2015.

DUAN, W.; KIRBY, R.; MUDGE, P. On the scattering of elastic waves from a non-axisymmetric defect in a coated pipe. **Ultrasonics,** Surrey**,** v. 65, n. 1, p. 228-241, 2016.

FAN, Y. et al. Energy flow prediction in built-up structures through a hybrid finite element/wave and finite element approach. **Mechanical Systems and Signal Processing,** London**,** v. 66, n. 1, p. 137-158, 2016.

GALÁN, J. M.; ABASCAL, R. Remote characterization of defects in plates with viscoelastic coatings using guided waves. **Ultrasonics,** Surrey**,** v. 42, n. 1, p. 877-882, 2004.

GAO, Y. et al. A model of the correlation function of leak noise in buried plastic pipes. **Journal of Sound and Vibration,** London**,** v. 277, n. 1-2, p. 133-148, 2004.

GRAFF, K. F. **Wave motion in elastic solids**. New York: Dover Publications, 1975. 649 p.

GRAVENKAMP, H.; BIRK, C.; SONG, C. Simulation of elastic guided waves interacting with defects in arbitrarily long structures using the Scaled Boundary Finite Element Method. **Journal of Computational Physics,** Orlando**,** v. 295, n. 1, p. 438-455, 2015.

HARLAND, N. R.; MACE, B. R.; JONES, R. W. Wave propagation, reflection and transmission in tunable fluid-filled beams. **Journal of Sound and Vibration,** London**,** v. 241, n. 5, p. 735-754, 2001.

HAYASHI, T.; SONG, W.-J.; ROSE, J. L. Guided wave dispersion curves for a bar with an arbitrary cross-section, a rod and rail example. **Ultrasonics,** Surrey**,** v. 41, n. 3, p. 175-183, 2003.

HAYASHI, T.; TAMAYAMA, C.; MURASE, M. Wave structure analysis of guided waves in a bar with an arbitrary cross-section. **Ultrasonics,** Surrey**,** v. 44, n. 1, p. 17-24, 2006.

HINKE, L.; MACE, B.; BRENNAN, M. Finite element analysis of waveguides. **ISVR Technical Memorandum,** Southampton**,** v. 932, p. 1-41, 2004.

ICHCHOU, M. N.; MENCIK, J. M.; ZHOU, W. Wave finite elements for low and mid-frequency description of coupled structures with damage. **Computer Methods in Applied Mechanics and Engineering,** Amsterdam**,** v. 198, n. 15–16, p. 1311-1326, 2009.

IHN, J.-B.; CHANG, F.-K. Pitch-catch active sensing methods in structural health monitoring for aircraft structures. **Structural Health Monitoring,** Thousand Oaks**,** v. 7, n. 1, p. 5-19, 2008.

INMAN, D. J. et al. **Damage prognosis: for aerospace, civil and mechanical systems**. West Sussex: Wiley, 2005. 449 p.

KAI, S. et al. Damage identification in thick steel beam based on guided ultrasonic waves. **Journal of Intelligent Material Systems and Structures,** Lancaster**,** v. 21, n. 3, p. 225-232, 2009.

KINSLER, L. E. **Fundamentals of acoustics**. New York: Wiley, 2000. 548 p.

KIRBY, R.; ZLATEV, Z.; MUDGE, P. On the scattering of torsional elastic waves from axisymmetric defects in coated pipes. **Journal of Sound and Vibration,** London**,** v. 331, n. 17, p. 3989-4004, 2012.

KÖPPE, E.; BARTHOLMAI, M.; PRAGER, J. Device concept for the generation of guided waves for early damage detection. **Procedia Engineering,** Amsterdam**,** v. 47, n. 1, p. 1185-1188, 2012.

LEE, S. K.; MACE, B. R.; BRENNAN, M. J. Wave propagation, reflection and transmission in non-uniform one-dimensional waveguides. **Journal of Sound and Vibration,** London**,** v. 304, n. 1–2, p. 31-49, 2007.

LEE, U. **Spectral Element Method in Structural Dynamics**. Singapore: Wiley, 2009. 454 p.

LOPES, V. et al. Impedance-based structural health monitoring with artificial neural networks. **Journal of Intelligent Material Systems and Structures,** Lancaster**,** v. 11, n. 3, p. 206-214, 2000.

MACE, B. R. Wave reflection and transmission in beams. **Journal of Sound and Vibration,** London**,** v. 97, n. 2, p. 237-246, 1984.

MACE, B. R. Power flow between two coupled beams. **Journal of Sound and Vibration,** London**,** v. 159, n. 2, p. 305-325, 1992a.

MACE, B. R. Reciprocity, conservation of energy and some properties of reflection and transmission coefficients. **Journal of Sound and Vibration,** London**,** v. 155, n. 2, p. 375-381, 1992b.

MACE, B. R. et al. Finite element prediction of wave motion in structural waveguides. **The Journal of the Acoustical Society of America,** Melville**,** v. 117, n. 5, p. 2835-2843, 2005.

MACE, B. R.; MANCONI, E. Modelling wave propagation in two-dimensional structures using finite element analysis. **Journal of Sound and Vibration,** London**,** v. 318, n. 4–5, p. 884-902, 2008.

MAHAPATRA, D. R.; GOPALAKRISHNAN, S. A spectral finite element for analysis of wave propagation in uniform composite tubes. **Journal of Sound and Vibration,** London**,** v. 268, n. 3, p. 429-463, 2003.

MANCONI, E. **Modelling wave propagation in two–dimensional structures using a wave/finite element technique**. 2008. 181 f. Thesis (PhD)- Department of Industrial Engineering, University of Parma, Parma, 2008.

MANCONI, E.; MACE, B. R. Wave characterization of cylindrical and curved panels using a finite element method. **The Journal of the Acoustical Society of America,** Melville**,** v. 125, n. 1, p. 154-163, 2009.

MANCONI, E.; MACE, B. R. Estimation of the loss factor of viscoelastic laminated panels from finite element analysis. **Journal of Sound and Vibration,** London**,** v. 329, n. 19, p. 3928-3939, 2010.

MANCONI, E.; MACE, B. R.; GARZIERA, R. The loss-factor of pre-stressed laminated curved panels and cylinders using a wave and finite element method. **Journal of Sound and Vibration,** London**,** v. 332, n. 7, p. 1704-1711, 2013.

MASRI, E. E.; FERGUSON, N.; WATERS, T. Detecting damaged reinforcement bars in concrete structures using guided waves. **Procedia Engineering,** Amsterdan**,** v. 199, n. 1, p. 1882-1887, 2017.

MEIROVITCH, L. **Methods of analytical dynamics**. New York: Dover Publications, 1970. 524 p.

MENCIK, J. M.; DUHAMEL, D. A wave finite element-based approach for the modeling of periodic structures with local perturbations. **Finite Elements in Analysis and Design,** Amsterdam**,** v. 121, n. 1, p. 40-51, 2016.

MILLER, D. W.; FLOTOW, A. V.; HALL, S. R. Active modification of wave reflection and transmission in flexible structures. In: American control conference, 1987, Minesota. **Proceedings…** New York: IEEE Control Systems Society, 1987. p.1318-1324.

MITRA, M.; GOPALAKRISHNAN, S. Extraction of wave characteristics from wavelet-based spectral finite element formulation. **Mechanical Systems and Signal Processing,** London**,** v. 20, n. 8, p. 2046-2079, 2006.

MITROU, G.; FERGUSON, N.; RENNO, J. Wave transmission through two-dimensional structures by the hybrid FE/WFE approach. **Journal of Sound and Vibration,** London**,** v. 389, p. 484-501, 2017.

MUGGLETON, J. M. et al. Approaches to estimating the reflection and transmission coefficients of discontinuities in waveguides from measured data. **Journal of Sound and Vibration,** London**,** v. 307, n. 1–2, p. 280-294, 2007.

MURTHY, M. V. V. S.; RENJI, K.; GOPALAKRISHNAN, S. A spectral element for wave propagation in honeycomb sandwich construction considering core flexibility. **Composite Structures,** Oxford**,** v. 127, p. 28-40, 2015.

NANDA, N.; KAPURIA, S.; GOPALAKRISHNAN, S. Spectral finite element based on an efficient layerwise theory for wave propagation analysis of composite and sandwich beams. **Journal of Sound and Vibration,** London**,** v. 333, n. 14, p. 3120-3137, 2014.

NILSSON, J. W.; RIEDEL, S. A. **Circuitos eletricos**. Sao Paulo: Pearson Brasil, 1983. 816 p.

OGATA, K. **System dynamics**. New Jersey: Prentice-Hall, 1978. 768 p.

RAO, S. S. **Vibrações mecânicas**. 4. ed. São Paulo: Pearson Prentice Hall, 2009. 1030 p.

RENNO, J. M.; MACE, B. R. Calculating the forced response of two-dimensional homogeneous media using the wave and finite element method. **Journal of Sound and Vibration,** London**,** v. 330, n. 24, p. 5913-5927, 2011.

RENNO, J. M.; MACE, B. R. Calculation of reflection and transmission coefficients of joints using a hybrid finite element/wave and finite element approach. **Journal of Sound and Vibration,** London**,** v. 332, n. 9, p. 2149-2164, 2013.

ROY MAHAPATRA, D.; GOPALAKRISHNAN, S. A spectral finite element model for analysis of axial–flexural–shear coupled wave propagation in laminated composite beams. **Composite Structures,** Oxford**,** v. 59, n. 1, p. 67-88, 2003.

SAMARATUNGA, D.; JHA, R.; GOPALAKRISHNAN, S. Wave propagation analysis in laminated composite plates with transverse cracks using the wavelet spectral finite element method. **Finite Elements in Analysis and Design,** Amsterdam**,** v. 89, n. 1, p. 19-32, 2014.

SATYARNARAYAN, L. et al. Circumferential higher order guided wave modes for the detection and sizing of cracks and pinholes in pipe support regions. **NDT & E International,** London**,** v. 41, n. 1, p. 32-43, 2008.

SISTEMA NACIONAL DE INFORMAÇÕES SOBRE SANEAMENTO. **Planilha AE2012:** resumo por abrangência. Brasília: Ministério das cidades, 2014. Disponível em: < http://www.snis.gov.br> Acesso em: 14 jul. 2014.

SØE-KNUDSEN, A.; SOROKIN, S. On accuracy of the wave finite element predictions of wavenumbers and power flow: A benchmark problem. **Journal of Sound and Vibration,** London**,** v. 330, n. 12, p. 2694-2700, 2011.

SREEKANTH KUMAR, D.; ROY MAHAPATRA, D.; GOPALAKRISHNAN, S. A spectral finite element for wave propagation and structural diagnostic analysis of composite beam with transverse crack. **Finite Elements in Analysis and Design,** Amsterdam**,** v. 40, n. 13–14, p. 1729-1751, 2004.

SU, Z.; YE, L. **Identification of damage using Lamb waves: from fundamentals to applications**. Berlin: Springer, 2009. 346 p.

TUA, P. S.; QUEK, S. T.; WANG, Q. Detection of cracks in cylindrical pipes and plates using piezo-actuated Lamb waves. **Smart Materials and Structures,** New York**,** v. 14, n. 6, p. 1325, 2005.

WAKI, Y.; MACE, B. R.; BRENNAN, M. J. Free and forced vibrations of a tyre using a wave/finite element approach. **Journal of Sound and Vibration,** London**,** v. 323, n. 3–5, p. 737-756, 2009a.

WAKI, Y.; MACE, B. R.; BRENNAN, M. J. Numerical issues concerning the wave and finite element method for free and forced vibrations of waveguides. **Journal of Sound and Vibration,** London**,** v. 327, n. 1–2, p. 92-108, 2009b.

YING, Y. et al. Damage detection in pipes under changing environmental conditions using embedded piezoelectric transducers and pattern recognition techniques. **Journal of Pipeline Systems Engineering and Practice,** Reston**,** v. 4, n. 1, p. 17-23, 2013.

ŻAK, A.; KRAWCZUK, M. Assessment of rod behaviour theories used in spectral finite element modelling. **Journal of Sound and Vibration,** London**,** v. 329, n. 11, p. 2099-2113, 2010.

ŻAK, A.; KRAWCZUK, M. Certain numerical issues of wave propagation modelling in rods by the Spectral Finite Element Method. **Finite Elements in Analysis and Design,** Amsterdam**,** v. 47, n. 9, p. 1036-1046, 2011.

ZHAO, X. G.; ROSE, J. L. Boundary element modeling for defect characterization potential in a wave guide. **International Journal of Solids and Structures,** New York**,** v. 40, n. 11, p. 2645-2658, 2003.

ZHENG, M.-F. et al. Modeling three-dimensional ultrasonic guided wave propagation and scattering in circular cylindrical structures using finite element approach. **Physics Procedia,** Amsterdam**,** v. 22, n. 1, p. 112-118, 2011.

ZHONG, W. X.; WILLIAMS, F. W. On the direct solution of wave propagation for repetitive structures. **Journal of Sound and Vibration,** London**,** v. 181, n. 3, p. 485-501, 1995.

ZHOU, C. W. et al. Multi-scale modelling for two-dimensional periodic structures using a combined mode/wave based approach. **Computers & Structures,** Elmsford**,** v. 154, n. 1, p. 145-162, 2015.

ZHOU, W. J.; ICHCHOU, M. N. Wave propagation in mechanical waveguide with curved members using wave finite element solution. **Computer Methods in Applied Mechanics and Engineering,** Amsterdam**,** v. 199, n. 33–36, p. 2099-2109, 2010.

ZHOU, W. J.; ICHCHOU, M. N.; MENCIK, J. M. Analysis of wave propagation in cylindrical pipes with local inhomogeneities. **Journal of Sound and Vibration,** London**,** v. 319, n. 1–2, p. 335-354, 2009.